

University of Alberta

EXPERIMENTAL AND THEORETICAL INVESTIGATION OF MASS TRANSPORT IN
POROUS MEDIA OF A PEM FUEL CELL

by

Lalit Mohan Pant

A thesis submitted to the Faculty of Graduate Studies and Research in partial fulfillment of the requirements for the degree of **Master of Science**.

Department of Mechanical Engineering

©Lalit Mohan Pant
Fall 2011
Edmonton, Alberta

Permission is hereby granted to the University of Alberta Libraries to reproduce single copies of this thesis and to lend or sell such copies for private, scholarly or scientific research purposes only.

Where the thesis is converted to, or otherwise made available in digital form, the University of Alberta will advise potential users of the thesis of these terms.

The author reserves all other publication and other rights in association with the copyright in the thesis and, except as herein before provided, neither the thesis nor any substantial portion thereof may be printed or otherwise reproduced in any material form whatsoever without the author's prior written permission.

To my Parents, my Family and the Cosmos

Abstract

Porous media is an integral part of polymer electrolyte fuel cell (PEMFC) electrodes. In this study, an experimental setup is presented to investigate convective and diffusive mass transport in porous media of fuel cell electrodes. A new theoretical model was developed in order to correct for inconsistencies in current models. Based on the new model, a new data extraction technique was used to obtain permeability and Knudsen diffusivity of a porous media from steady state pure convection measurements. The model was also used to obtain effective diffusivity of porous media from mass transport experiments. Using the obtained transport properties, the models were used to predict mass transport in the electrodes under different operating conditions. Preliminary comparisons of experimental and theoretical predictions show that the new mass transport model is capable of predicting mass transport in the electrode accurately. The results concluded that the traditionally used Bruggeman correlation overpredicts the electrode effective diffusivity by as much as 3-4 times.

Keywords: mass transport, fuel cell, porous media, effective diffusivity

Acknowledgements

I would like to thank my supervisors Dr. Marc Secanell and Dr. Sushanta Mitra for awarding me the opportunity to pursue research under their guidance and for their support and encouragement in last two years. I would like to thank Dr. Marc Secanell for he has been a great source of inspiration for me. Over the last two years, the help I have received from him is invaluable. Be it the problems in modelling, experimentation or reviews of my writings, he has always been very helpful and understanding. Without his help and motivation, it would have been arduous to tackle the obstacles of this project. The discussions I had with him on technical subjects and on life in general will be always cherished in life.

I would like to thank Dr. Sushanta Mitra for considering my application and providing me the opportunity to be here in the first place. His confidence in me even during the tough times of research has been very helpful. He has always been very brisk and generous in resolving the problems. In my two years with him, I have been simply mesmerized by his professionalism and efficient work management. His ambitious perspective of life is something I try to apprentice in my life.

I would like to thank Dr. Subir Bhattacharjee for providing me access to OSCIEF experimental facility and micro-GC, without which this work could not have been completed. I would also like to thank him for all the techno-philosophical discussions in thermodynamics class, which were really motivating. I would like to thank all of my colleagues at energy systems design laboratory (ESDL) group and micro-nano scale transport laboratory (MNLT) group for sharing their enthusiasm and ideas of research. Especially I would like to thank Prashant Waghmare and Naga Shiva for their incredible help during my initial days in Edmonton.

I would like to thank all my family members for their love and encouragement over all these years. Without their emotional support, it would have been really hard to sustain away from home for so long. The help and encouragement from my family has been the the driving force in my life. Without my parents calm words and encouragement for learning, I could have never reached this far. My father has been a teacher for me who not only taught me mathematics in my childhood but also the valuable lessons of life. My brothers have been a been a great source of inspiration in my life for hard work, dedication and patience. If is was not for their consistent efforts and confidence in me, I would have never even got a good start of academic life.

Last but not least, I am thankful to the cosmos for this amazing creation we call the universe. If it was not for all the mysteries of universe and the sophisticated physics behind each one of them, there wouldn't be much to research about and the world of science could have never been so mesmerizing.

Table of Contents

1	Introduction	1
1.1	Motivation	1
1.2	Literature Review	3
1.2.1	Fuel Cells and Challenges	3
1.2.2	Mass Transport in Porous Media	6
1.2.3	Molecular Diffusivity Measurements in Porous Media	12
1.2.4	Permeability Estimation in Porous Media	22
1.2.5	Knudsen Diffusivity Estimation in Porous Media	22
1.3	Contributions	24
1.4	Structure of the Thesis	24
2	Experimental Setup	26
2.1	Experimental Setup for Mass Transport Measurements	26
2.1.1	Schematics of Experimental Setup for Mass Transport Measurements	28
2.1.2	Fabrication of Counter-diffusion Chip	29
2.1.3	Mass Flow Controllers	33
2.1.4	Pressure Controllers	33
2.1.5	Gas Chromatograph	34
2.1.6	Data Acquisition	36
2.1.7	Experimental Procedure and Data Reduction	36
2.1.8	Data Error Analysis for Mass Transport Measurement	39
2.2	Experimental Setup for Permeability Measurements	41
2.2.1	Data Error Analysis for Permeability Measurement	42
3	Numerical Modelling of Mass Transfer in Porous Media	45
3.1	Problem Description	46
3.2	Governing Equations	47
3.2.1	Fick's Law	47

3.2.2	Dusty Gas Model	49
3.2.3	Binary Friction Model	52
3.2.4	Modified Binary Friction Model	57
3.2.5	Numerical Modelling	60
3.3	Validation	63
3.4	Results and Parametric Studies	66
3.4.1	Mass Transport in Gas Diffusion Layers	66
3.4.2	Mass Transport in Micro Porous Layers	69
3.4.3	Mass Transport in GDL MPL Assemblies	76
3.5	Conclusion	79
4	Results on Permeability and Diffusivity Measurements and Discussion	80
4.1	Permeability Measurements in Porous Media	80
4.1.1	Permeability Measurements in Gas Diffusion Layers	82
4.1.2	Permeability Measurements in Micro Porous Layers	85
4.1.3	Limitations of Darcy’s Law and a New Approach to Calculate Permeability	87
4.1.4	Permeability and Knudsen Diffusivity Validation	95
4.1.5	Sensitivity Analysis of Permeability Results	96
4.2	Diffusivity Measurements in Porous Media	99
4.2.1	Diffusivity Measurements in Gas Diffusion Layers	100
4.2.2	Diffusivity Measurements in Micro Porous Layers	100
4.2.3	Diffusivity Estimation Validation	102
4.2.4	Sensitivity Analysis of Diffusivity Results	104
5	Conclusion and Future Work	107
5.1	Conclusion	107
5.2	Future Work	109
	References	111

List of Tables

1.1	List of the experimental methods used for diffusivity measurement . . .	21
3.1	Problem solving parameters for code validation	63
3.2	Problem solving parameters for MPL simulation	70
3.3	Problem solving parameters for GDL-MPL assembly simulation . . .	76
4.1	Permeability values for a SGL SIGRACET 34BA GDL	85
4.2	Permeability values for a SGL SIGRACET 34BC GDL-MPL assembly	86
4.3	Geometric parameters and permeability calculations for a SGL SIGRACET 34BC GDL-MPL assembly	87
4.4	Knudsen number calculations for different gases in GDL and MPL . .	88
4.5	Applicability of different flow models in different flow regimes based on Knudsen number	89
4.6	Permeability and Knudsen diffusivity values in PEM fuel cell porous media	95
4.7	Effective diffusivity values in MPL for the best fit of different mass transport models	102
4.8	Geometric and transport parameters of GDL and MPL estimated from the experiments in a SIGRACET 34BC porous media	104

List of Figures

1.1	The basic schematic of a polymer electrolyte fuel cell	3
1.2	Operation diagram of a polymer electrolyte fuel cell	5
1.3	Performance curve of a fuel cell	6
1.4	Species interaction for different mass transport mechanisms	8
1.5	The tortuosity comparison of two porous media with same porosity .	15
1.6	Experimental schematics for different diffusivity measurement techniques	16
2.1	Basic schematic of a mass transport measurement setup based on diffusion bridge	27
2.2	Schematics of the mass transport measurement setup	28
2.3	Images of the machined acrylic channel for the counter diffusion chip	30
2.4	The porous media assembly laminated in a polymer sheet	31
2.5	The gasket used in diffusion bridge chip	31
2.6	An exploded view of the final diffusion bridge assembly	32
2.7	A snapshot of the final diffusion bridge assembly	32
2.8	Interaction of channel velocity and diffusive boundary layer in a diffusion bridge	33
2.9	Comparison of velocity in the flow channels with velocity across porous media for a SIGRACET 34BC	34
2.10	Schematic of a gas chromatograph	35
2.11	A snapshot of mass transport experimental setup	36
2.12	Flow chart for mass transport measurements	38
2.13	A sample chromatogram obtained from chromatography experiment .	38
2.14	The calibration curve for micro-GC under medium sensitivity of TCD	39
2.15	Repeatability analysis results on mass transport experimental setup .	41
2.16	Schematics of the permeability measurement experimental setup . . .	42
2.17	Repeatability analysis results for the permeability measurement setup	44
3.1	The problem domain used for numerical modelling	46
3.2	Flow circuit diagram proposed for DGM	50

3.3	The comparison of O_2 viscous friction parameter used in BFM and MBFM in a $O_2 - N_2$ binary mixture	60
3.4	The comparison of N_2 viscous friction parameter used in BFM and MBFM in a $O_2 - N_2$ binary mixture	60
3.5	Comparison of oxygen flux variation for different mass transport models	64
3.6	Comparison of oxygen partial pressure across the GDL for different models. Solution at zero pressure difference across porous media . . .	64
3.7	Comparison of oxygen partial pressure across the GDL for different models. Solution at $\Delta p = 250\text{Pa}$ across porous media	65
3.8	Comparison of oxygen partial pressure across the GDL for different models. Solution at $\Delta p = 500\text{Pa}$ across porous media	65
3.9	Comparison of oxygen flux variation in GDL for different mass transport models	66
3.10	Comparison of oxygen partial pressure across the GDL for different models. Solution at $\Delta p = 1\text{kPa}$ across porous media	67
3.11	Comparison of nitrogen flux variation in GDL for different mass transport models	68
3.12	Comparison of nitrogen partial pressure across the GDL for different models. Solution at zero pressure difference across porous media . . .	68
3.13	Comparison of nitrogen partial pressure across the GDL for different models. Solution at $\Delta p = 1\text{ kPa}$ across porous media	69
3.14	Comparison of oxygen flux variation in MPL for different mass transport models	70
3.15	Profile of oxygen partial pressure across MPL, predicted by different models. Solution at zero pressure difference across porous media . . .	72
3.16	Profile of oxygen partial pressure across MPL, predicted by different models. Solution at $\Delta p = 10\text{kPa}$ across porous media	72
3.17	Profile of oxygen partial pressure across MPL, predicted by different models. Solution at $\Delta p = 20\text{kPa}$ across porous media	73
3.18	Comparison of nitrogen flux variation with increase in pressure difference in MPL, for different mass transport models	74
3.19	Profile of nitrogen partial pressure across MPL, predicted by different models. Solution at zero pressure difference across porous media . . .	74
3.20	Profile of nitrogen partial pressure across MPL, predicted by different models. Solution at $\Delta p = 10\text{kPa}$ across porous media	75
3.21	Profile of nitrogen partial pressure across MPL, predicted by different models. Solution at $\Delta p = 20\text{kPa}$ across porous media	75

3.22	Comparison of oxygen flux variation in GDL-MPL assembly for different mass transport models	77
3.23	Profile of oxygen partial pressure across GDL- MPL assembly, predicted by different models. Solution at $\Delta p = 0\text{kPa}$ across porous media	77
3.24	Profile of oxygen partial pressure across GDL- MPL assembly, predicted by different models. Solution at $\Delta p = 10\text{kPa}$ across porous media	78
3.25	Profile of oxygen partial pressure across GDL- MPL assembly, predicted by different models. Solution at $\Delta p = 20\text{kPa}$ across porous media	78
4.1	A schematics of multiple layer assembly in permeability measurement	82
4.2	Overview of a SGL SIGRACET 34BA GDL assembly	83
4.3	The pressure drop vs velocity profile with oxygen for 34 BA and its comparison with datafit	84
4.4	Comparison of pressure gradient vs velocity profiles for two samples of 34BA	84
4.5	Overview of a SGL SIGRACET 34BC GDL-MPL assembly	85
4.6	Net pressure drop vs velocity profile for SGL SIGRACET 34BC assembly	86
4.7	Comparison of experimentally observed pressure drop across a SGL SIGRACET 34BC GDL-MPL assembly with Darcy-Forchheimer prediction	89
4.8	Experimental results vs Darcy's datafit for O_2 in a SGL SIGRACET 34BA GDL	91
4.9	Experimental results vs MBFM datafit for He in a SGL SIGRACET 34BA GDL	92
4.10	Comparison of experimental data to a linear datafit for a SIGRACET 34BC assembly with O_2	94
4.11	Comparison of experimental and MBFM predictions for flow across porous media	96
4.12	Sensitivity of GDL permeability and Knudsen diffusivity of oxygen with respect to GDL thickness	97
4.13	Comparison of pressure drop vs velocity profile for two samples of SIGRACET 24BC with different cross sections	98
4.14	Comparison of experimental flux measurements with numerical predictions using Bruggeman correlation	99
4.15	Variation of the residual with tortuosity for the least square method	101

4.16	Comparison of experimental and best fitting numerical results of mass transport, using MPL tortuosity as fitting parameter	102
4.17	Comparison of experimental and numerical results for validation of MPL tortuosity calculations	103
4.18	Sensitivity of MPL diffusivity with respect to GDL diffusivity	105
4.19	The comparison of best fitting numerical results with experimental results of mass transport, for an MPL thickness of $50\mu m$	106

Nomenclature

English Letters

B_0	Viscous permeability of the pore, [m^2]
B_1	Inertial permeability of the porous media, [m]
B_v	Viscous permeability of porous media, [m^2]
c_i	Molar concentration of species i , [$mol \cdot m^{-3}$]
c_t	Molar concentration of mixture, [$mol \cdot m^{-3}$]
D'	Diffusion coefficients with second order corrections, [$m^2 \cdot s^{-1}$]
D_i^K	Knudsen diffusion coefficient of species i , [$m^2 \cdot s^{-1}$]
D_{ij}	Binary diffusion coefficient, [$m^2 \cdot s^{-1}$]
Kn	Knudsen number
L	Thickness of porous media, [m]
\dot{m}	Mass flow rate, [$kg \cdot s^{-1}$]
M	Molecular weight, [$gm \cdot mol^{-1}$]
N	Net molar flux, [$mol \cdot m^{-2} \cdot s^{-1}$]
n	Net mass flux, [$kg \cdot m^{-2} \cdot s^{-1}$]
n^D	Diffusive mass flux, [$kg \cdot m^{-2} \cdot s^{-1}$]
N^D	Diffusive molar flux, [$mol \cdot m^{-2} \cdot s^{-1}$]
N^{visc}	Viscous flux of the mixture, [$mol \cdot m^{-2} \cdot s^{-1}$]
p, p_t	Total pressure, [Pa]

p_i	Partial pressure of species i , [Pa]
\dot{Q}	Volumetric flow rate, [$m^3 \cdot s^{-1}$]
R	Universal Gas Constant, [$J \cdot mol^{-1} \cdot K^{-1}$]
r_p	Pore radius, [m]
r_{im}	Membrane friction parameter used in MBFM, [$mol^{-1} \cdot m \cdot s$]
T	Temperature, [K]
v_i	Velocity of species i , [$m \cdot s^{-1}$]
v	Mass averaged velocity, [$m \cdot s^{-1}$]
x	Mole fraction

Greek Letters

β_{im}	Membrane friction parameter used in BFM, [$m^{-2} \cdot s$]
χ_i	The viscous friction parameter used in MBFM, [s]
ϵ	Void volume fraction of porous media
η	Viscosity of the fluid, [$Pa \cdot s$]
κ_i	Partial viscosity or the viscous friction parameter used in BFM, [s]
μ	Chemical potential, [$J \cdot mol^{-1}$]
ω	Species mass fraction
ρ	Density, [$kg \cdot m^{-3}$]
τ	Tortuosity of the porous media

Subscripts and Superscripts

eff	Effective parameter, averaged over porous media
i, j	Species index in mixture
$visc$	Viscous part of the parameter

Abbreviations

CL Catalyst layer

GDL Gas diffusion layer

GHG Green house gases

MCFC Molten carbonate fuel cell

MPL Micro porous layer

PEM Polymer electrolyte membrane

PEMFC/PEFC Polymer electrolyte membrane fuel cell

PTFE Polytetrafluoroethylene

SOFC Solid oxide fuel cell

Chapter 1

Introduction

1.1 Motivation

During the last decade, polymer electrolyte fuel cells (PEMFC) have emerged as promising energy conversion devices for power electronics, backup power units, domestic co-generation of electricity and hot water, and as a replacement for the internal combustion engine in automobiles [1]. Recently launched products like the fuel cell operated laptop by Toshiba [2], and Daimler's F-Cell fuel cell car highlight the increasing industrial interest towards this technology. In the near future, fuel cells might be a major component of portable electronics, backup power generators and automobiles.

Fuel cells are high energy efficiency and low noise energy conversion devices that, when fuelled with hydrogen from either nuclear or renewable sources, provide electrical energy while producing zero particulate, nitrogen and sulphur oxide, and green house gas (GHG) emissions. The replacement of the current internal combustion engine in automobiles with fuel cells could therefore result in a considerable reduction of particulates and GHG emissions from the transportation sector and could potentially eliminate smog in large cities such as Kolkata and Los Angeles. Replacing the internal combustion engine with batteries could also eliminate emission from the transportation sector; however, due to the limited amount of energy in the battery and long recharging durations, the range of battery vehicles is limited [3]. Therefore, both fuel cell and battery vehicles will likely co-exist in the future with fuel cell used for long range vehicles, and batteries used in city-bound vehicles. Due to the fast refuelling and long runtime capabilities of fuel cells, they are also considered as an alternative to current battery technologies in markets such as portable electronics, backup power applications and forklifts.

In order to make fuel cells a viable choice for consumers, further cost and durability improvements are necessary. Cost reductions depend in large part to the ability of fuel cell designers to reduce the amount of expensive platinum catalyst currently used in fuel cells. Improving mass transport would allow fuel cells to operate at much higher current densities, thereby reducing the amount of necessary catalyst. Therefore, mass transport in fuel cell porous media has to be well understood in order to optimize the catalyst amount and its distribution inside the electrode. To date, a well defined relationship between porous media structure and mass transport does not exist. As an example, a recent experimental study has shown that current mass transport models are underpredicting the mass transport limitations in porous media by a factor of four [4].

The motivation of this project is to understand the mass transport processes in fuel cell electrodes. This will be helpful in designing better fuel cell electrodes with reduced mass transport limitations, thereby improving catalyst utilization. An extensive experimental study of mass transport in porous media will be helpful in understanding the physics of mass transport, enabling us to develop reliable and accurate governing equations. The mass transport governing equations can be used for computer-aided design and optimization of new fuel cell designs. Finally, the experimental study will also help in determining the transport properties of new porous electrodes fabricated in the Energy Systems Design laboratory in order to assess the ability of new fabrication techniques to create electrode micro-structures that enhance mass transport.

This thesis describes the development of a mass transport measurement setup. The current chapter discusses the mass transport mechanisms in fuel cell porous media and the experimental methodologies used to measure its governing parameters. Section 1.2.1 gives a basic introduction of polymer electrolyte fuel cells, their operation and the challenges faced when trying to improve its performance. This is followed by a review of mass transport in porous media and a discussion of theoretical models in section 1.2.2. Section 1.2.3 discusses several experimental techniques for mass transport measurement. Finally, the impact of this research and the thesis outline are given in sections 1.3 and 1.4 respectively.

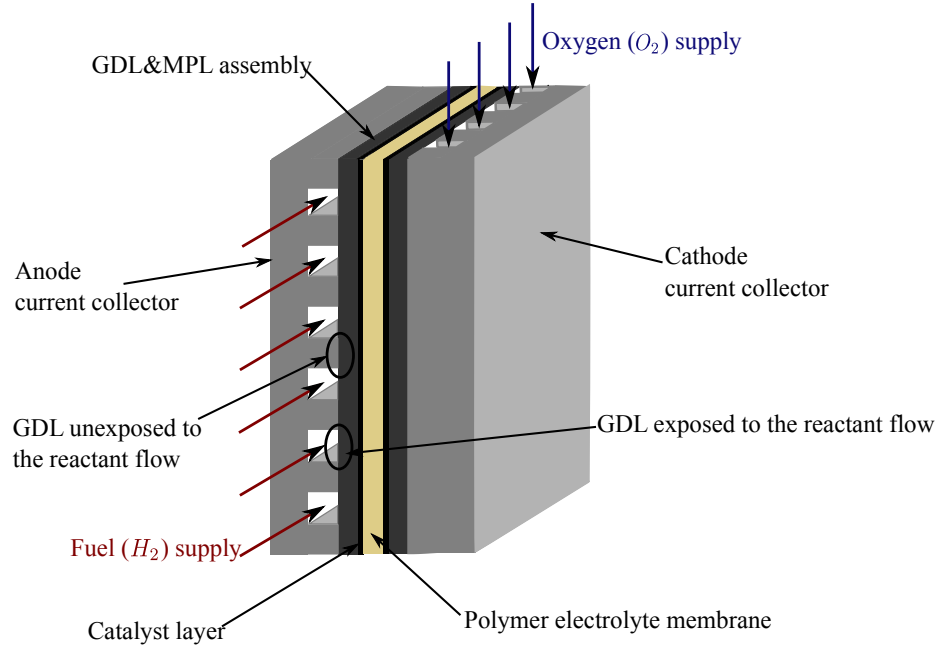


Figure 1.1 – The basic schematic of a polymer electrolyte fuel cell

1.2 Literature Review

1.2.1 Fuel Cells and Challenges

A polymer electrolyte membrane fuel cell (PEMFC) is an electrochemical energy conversion device, which converts the chemical energy of the fuel to electrical energy. A basic schematics of a PEM fuel cell is shown in Fig. 1.1. There are four main components of a PEMFC listed as follows:

- **The current collectors (Bi -polar plates):** The current collectors are made of highly conducting material like graphite or metals for current and heat transport. The reactant supply channels are also fabricated within the bipolar plates in different configurations [5]. These serve as a basic structural block of fuel cell as well as electron conductors.
- **Gas diffusion layer (GDL):** The gas diffusion layers are made of carbon fibers bonded together with polytetrafluoroethylene (PTFE). This layer is sometimes coated with a micro porous layer (MPL) in a GDL-MPL assembly. The micro porous layer is made of nanoporous carbon and PTFE. The porous media provides a medium for transport of reactants and products (oxygen, nitrogen, hydrogen, water vapour, liquid water) through its pores and for electrons through its carbon scaffolding [6]. The GDL is in direct contact with the flow channels

grooved in bipolar plates. It is a highly porous medium and allows the reactants to diffuse quickly within the GDL. This creates a uniform reactant supply over the entire cross section of the catalyst layer (CL). This is especially important in the parts of CL which are not exposed directly to the flow channels as shown in Fig. 1.1. The micro porous layers have a high PTFE content around 30% [7]. Due to its pore structure and high PTFE content, the MPL is hydrophobic and helps to remove water produced in the electrochemical reaction.

- **Catalyst layer:** The catalyst layer is usually fabricated by depositing an ink made of platinum supported carbon black and Nafion ionomer in a solvent [8]. It is the layer in the fuel cell where all the electrochemical reactions occur. The most agreed upon structure of the catalyst layer have carbon agglomerates bounded by Nafion ionomer, where the *Pt* particles are supported on the carbon agglomerates [9]. The reactant and products travel through the void volume, the electrons travel through the carbon/platinum and the protons travel through the ionomer. For an electrochemical reaction to occur in the catalyst layer, all the three phases must be present at the reaction site [10].
- **Polymer electrolyte membrane:** The electrolyte in a PEMFC is made of a sulfonated tetrafluoroethylene polymer called Nafion [10]. The purpose of electrolyte in the fuel cell is to allow only protons but not electrons through it.

The basic overview of a PEMFC mechanism is shown in Fig. 1.2. In a PEM fuel cell, the fuel (H_2) is supplied at the anode and the reactant (O_2) is supplied at the cathode. Hydrogen is split into a proton and an electron, as shown in the following half cell reaction at the anode:



The protons transport through the electrolyte membrane to the cathode and the electrons go through an external circuit towards cathode producing useful electrical current. The protons and electrons react with oxygen at cathode as shown in the following half cell reaction:



The overall cell reaction in a PEMFC can be given as follows:



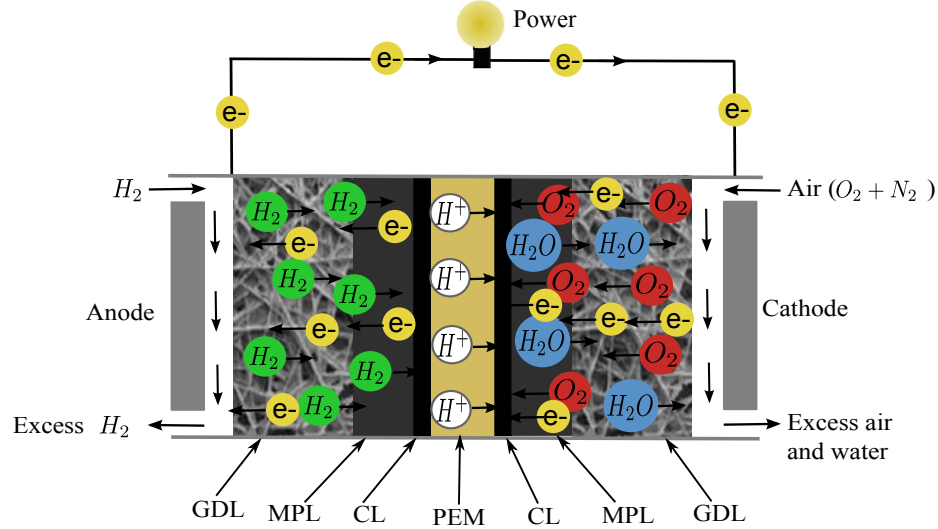


Figure 1.2 – Operation diagram of a polymer electrolyte fuel cell

The electrochemical reactions in catalyst layer can only happen when the reactants, electrons, protons and the catalyst are all present. The reactants travel through the void pores, the electrons travel through the carbon and platinum and protons travel through the Nafion ionomer. Therefore, the catalyst in catalyst layers is not utilized everywhere but only at the three phase boundary of void pore, Nafion and platinum. Additionally, as the reactants move along the catalyst layer, they get depleted. Therefore less and less catalyst in the inner parts of CL has access to the reactants. An optimized catalyst layer will give higher platinum specific activity, or in other words, higher power for same amount of catalyst.

The power output from a fuel cell depends upon the current density. A performance curve of the PEMFC is shown in Fig. 1.3. The three losses in fuel cell compared to an ideal profile are due to reaction kinetics, ohmic losses and mass transport limitations. The power density of the fuel cell is mainly limited by mass transport considerations at higher current densities, hence the current research is focused on minimizing the mass transport losses in porous media. The maximum fuel supply rate depends on the transport properties of the porous media and operating parameters. After a certain current density, the rate of consumption at reaction sites overtakes the supply rate and fuel cell starvation occurs. At low operating temperatures and high current densities, the water produced during the reaction floods the porous media, which in turn interrupts the reactant supply to catalyst layer. This reduces the fuel cell performance drastically [11].

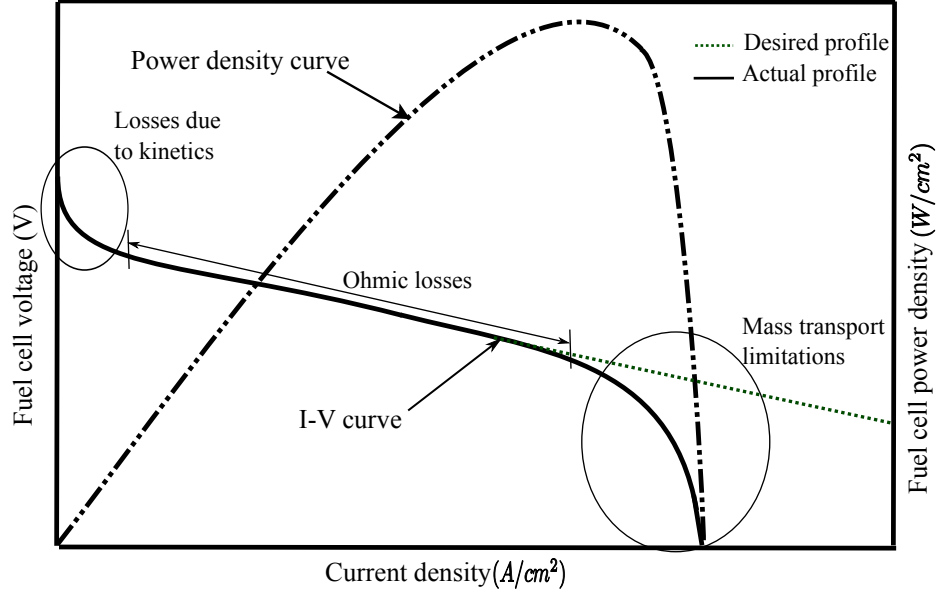


Figure 1.3 – Performance curve of a fuel cell [12]

To improve fuel cell performance, mass transport in the fuel cell porous media has to be improved. The two major improvements possible are: 1) Improvement of transport properties of porous media for gas transport, and; 2) reduction of water accumulation in porous media. This research work is focused on improving transport properties of fuel cell porous media for gas transport. The porous media is a complex and random structure, whose effects on the flow are not very well understood. To improve the transport properties, a thorough understanding of the transport physics in the porous media is necessary. The mass transport models are very important for modelling and optimization of fuel cell [13, 14]. The study of gas transport is also necessary to understand the liquid transport and accumulation. The current water transport models are not capable of explaining the interaction of liquid and gas phases. Another major application of gas transport studies is in high temperature fuel cells like SOFC and MCFC, where the liquid water accumulation is not an issue and the gas transport limitations are quite important.

1.2.2 Mass Transport in Porous Media

Mass transport is a vital mechanism in fuel cells for reactant and product transport. Mass transport can be defined as translocation of a species under the influence of driving forces [15]. This section presents the generalized models of mass transport and their development for specific cases of porous media.

General Models of Mass Transport

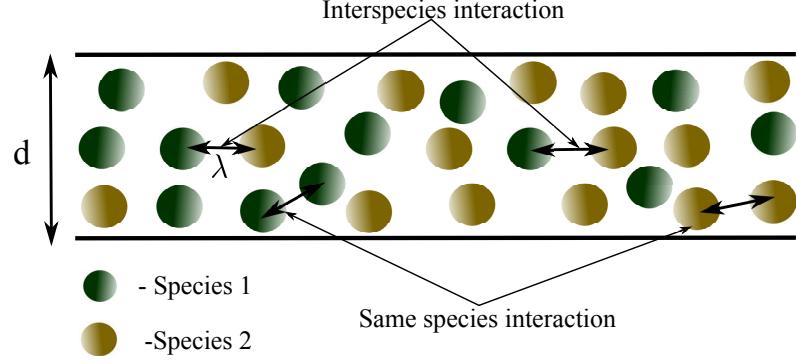
The transport of the species is driven by various driving forces. There are several driving forces for mass transport, which can act alone or together on a species. The net driving force in gases is given by Taylor and Krishna [15] as follows:

$$\mathbf{d}_i = \frac{1}{c_t RT} \left[\underbrace{c_i \nabla_{T,p} \mu_i}_{\text{Chemical potential gradient term}} + \underbrace{(c_i \bar{V}_i - \omega_i) \nabla p}_{\text{Net pressure gradient term}} - \underbrace{\rho_i \left(\mathbf{F}_i - \sum_{j=1}^n \omega_j \mathbf{F}_j \right)}_{\text{External force term}} + \underbrace{\sum_{\substack{j=1 \\ j \neq i}}^n \left(\frac{x_i x_j}{D_{ij}} \right) \left(\frac{D_i^T}{\rho_i} - \frac{D_j^T}{\rho_j} \right) \nabla \ln T}_{\text{Temperature gradient term}} \right] \quad (1.4)$$

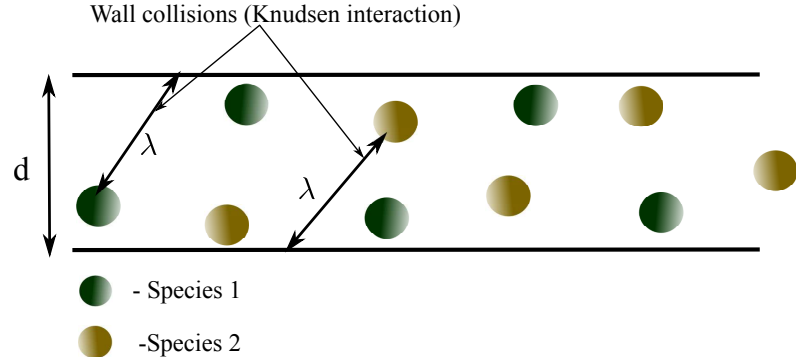
where μ_i is the chemical potential of species i , ω_i is the mass fraction, c_i and c_t are the concentrations of species i and the mixture respectively, \bar{V}_i is the partial molar volume, p is total pressure, ρ_i is the density of species i , \mathbf{F} is the external force, D_{ij} is the Maxwell-Stefan diffusion coefficient and D^T is the thermal diffusion coefficient.

The various driving forces as shown in eq. (1.4) are chemical potential gradient, net pressure gradient, external forces and force caused by thermal collisions. The chemical potential gradient is caused by the difference in composition of species, the net pressure gradient is due to the pressure difference between two locations, the external force can be any force such as electric force and magnetic force and the thermal collisions forces are present due to temperature gradient.

In a mass transport system, there are frictional forces present to balance the driving forces. Figure 1.4 shows the various friction forces present for binary mixture transport in a pore. When the pore diameter is sufficiently large, the molecule-molecule collisions are more dominant than molecule-wall collisions as shown in Fig. 1.4(a). When two molecules of the same species collide the net momentum of that species remain the same, hence the net momentum transfer is zero. However, when molecules of two different species collide, momentum is transferred from one species to another [15]. This net transfer of momentum is accounted by the interspecies drag



(a) Species interaction during mass transport in a pore for Bulk diffusion ($\lambda \ll d$) [16]



(b) Species interaction during mass transport in a pore for Knudsen diffusion ($\lambda \gg d$) [16]

Figure 1.4 – Species interaction for different mass transport mechanisms. λ is the distance travelled by molecule before colliding with another molecule or wall

force, which is given by Krishna and Wesselingh [16] as follows:

$$\mathbf{F}_{d,i} = \sum_{\substack{j=1 \\ j \neq i}}^n \frac{x_i \mathbf{N}_j - x_j \mathbf{N}_i}{c_t D_{ij}} \quad (1.5)$$

where x_i, x_j and N_i, N_j are mole fractions and molar fluxes of species i and j respectively. $F_{d,i}$ represents the total drag force on species i by all other species.

For very small pore sizes or in rarefied gases, the mean free path of the gases is much higher than the length scale of the system. In this case, the molecule wall-collisions will be much higher compared to molecule-molecule interactions. In these cases, wall friction governs the species transport, which is also referred as Knudsen friction. The Knudsen friction is given as [17]:

$$\mathbf{F}_{w,i} = \frac{\mathbf{N}_i}{c_t D_i^K} \quad (1.6)$$

where D_i^K is the Knudsen diffusion coefficient, which depends on pore radius and the species molecular weight.

Apart from interspecies drag and Knudsen friction, another frictional force acting on the flow is the viscous friction force. When there are sufficient number of molecules moving in a pore with certain velocity, a boundary layer will be created due to interaction with the wall. The boundary layer will cause a viscous drag on the species and will reduce the net driving force. The viscous friction force is dependent on the permeability of the pore and viscosity of the mixture and can be derived from Darcy's law [18].

The Maxwell-Stefan approach presented by Taylor and Krishna [15] presents a theoretical model for multicomponent mass transport in pure diffusion. The Knudsen friction and viscous friction effects are neglected. The following equation is given to describe the state of the system [15]:

$$\mathbf{d}_i = \sum_{\substack{j=1 \\ j \neq i}}^n \frac{x_i \mathbf{N}_j - x_j \mathbf{N}_i}{c_t D_{ij}} \quad (1.7)$$

where \mathbf{d}_i is given by eq. (1.4). This is the general form of Maxwell-Stefan equations. In case of extremely dilute mixtures, a species can only interact with the bulk and not with other species. In this case the mixture can be considered to be a binary mixture with respect to each species, where $x_i \ll 1$ and $x_j \simeq 1$. For an isothermal system, under uniform pressure and in absence of external forces, eq. (1.7) can be given as follows [15]:

$$\mathbf{d}_i = \frac{c_i}{c_t RT} \nabla_{T,p} \mu_i = -\frac{\mathbf{N}_i}{c_t D_{ij}} \Rightarrow \nabla x_i = -\frac{\mathbf{N}_i}{c_t D_{ij}} \quad (1.8)$$

This equation is the same as Fick's law, which is described in detail by Bird et al. [19]. This relationship was experimentally observed by Fick [20] while working on diffusion of salt in liquids. As per the derivation of the equation, the diffusive flux of a species is measured relative to the average mixture velocity [19].

$$\mathbf{N}_i = c_i(\mathbf{v}_i - \mathbf{v}) = -D_{ij} \nabla c_i \quad (1.9)$$

To account for the effects of net pressure gradient on mass transport, the average convective velocity is added to the Fick's law as follows [19]:

$$\mathbf{N}_i = -D_{ij} \nabla c_i + c_i \mathbf{v} \quad (1.10)$$

where \mathbf{v} is the convective velocity of the mixture, which is obtained by performing a momentum balance on the mixture. Fick's law has been extensively used for mass transport studies. However, its application is limited to binary mixtures as discussed earlier. The Maxwell-Stefan model is a generalized form of Fick's law which can be used for multicomponent mixtures. However, the Maxwell-Stefan equations do not take into account viscous and Knudsen friction.

Mass transport can be defined in three distinct regions of molecular transport, viscous transport and Knudsen transport. In between these regions, there are transition regimes combining any two modes [21]. Kast and Hohenthanner [21] have explained the laws of different transport modes and techniques to combine them in transition regions for single fluids and binary mixtures. The solution from resulting equations was found to validate Graham's law of diffusion ($N_i \propto 1/\sqrt{M_i}$). The Knudsen diffusivity and permeability can be found by steady state permeability measurements on a porous media between continuum and Knudsen region [21].

Mass Transport Models in Porous Media

The mass transport in porous media is different compared to normal capillary transport (bulk transport). The porous media contains numerous capillary like structures of varying sizes which are interconnected. All the forces must be accounted for in the pores for accurate modelling. The interspecies interaction term is the same as given earlier. The Knudsen interactions and viscous friction can be accounted by using individual momentum balance equations for each species with considerations for wall boundaries.

Kerkhof and Geboers [22] recently proposed a new multicomponent mass transport model based on a new solution of Boltzmann equation. The model is a generalized form of Navier-Stokes equation with momentum balance of each species, eliminating the need for a mixture velocity. The model was validated for a Stefan-tube problem by Salcedo-Diaz et al. [23]. Bearman and Kirkwood [24] have also presented transport equations for multicomponent systems based on statistical mechanics. However, these models are only suitable for pore scale modelling where individual boundary conditions for pore walls can be applied. Using it to model mass transport in porous media can be an extremely complex and tedious task. A simpler way of modelling is to use volume averaged models of mass transport. For a volume averaged model in porous media, the boundary conditions have to be incorporated in problem parameters.

A multicomponent mass transport model for membranes is presented by Lightfoot [25]. The model is based on irreversible thermodynamics approach and it accounts for the wall effects (Knudsen and viscous). Rate of entropy generation in a control volume due to all forces is calculated and the net driving force is derived, which is then balanced by the friction forces [26]. The resulting equation is then extended to include the membrane as a species and a new force balance is derived for the system. The final force balance equation is given as:

$$\frac{x_i}{RT} \nabla_{T,p} \mu_i + \frac{c_i \bar{V}_i}{c_t RT} \nabla p - \frac{\rho_i}{c_t RT} \mathbf{F}_i = \sum_{j=1}^n \frac{x_i \mathbf{N}_j - x_j \mathbf{N}_i}{c_t D_{ij}} - r_{im} \mathbf{N}_i \quad (1.11)$$

where r_{im} is the membrane friction parameter, which accounts for the effects of the porous media/membrane of the species. This is obtained by extending the interspecies interaction term to include the porous media and then setting its flux as zero [26]. The Lightfoot equation is theoretically consistent, but the membrane friction parameter is not well defined. Kerkhof [26] pointed out that the flux averaging in Lightfoot equation has been done abruptly and without any justification.

Mason and Malinauskas [17] have presented a multicomponent mass transport model in porous media, namely the dusty gas model (DGM). The DGM is based on Maxwell-Stefan equations of force balance, and can take into account interspecies, Knudsen and viscous forces. The basic assumption of DGM is that the flux values in the Maxwell-Stefan equation are diffusive only, and can be extended to include viscous effects. Mason and Malinauskas [17] suggest that the net flux can be split into diffusive and viscous flux, which can be then replaced into Maxwell-Stefan equation. Similar to the Lightfoot equation, interspecies terms are summed over all species and the porous media. While summing the forces, the diffusive flux of the porous media is assumed to be zero, which is theoretically inconsistent. The membrane friction parameter is assumed to be the same as Knudsen diffusivity. The final DGM equation is given as [26]:

$$\frac{1}{p_t} \nabla_{T,p} p_i = \sum_{j=1}^n \frac{x_i \mathbf{N}_j - x_j \mathbf{N}_i}{c_t D_{ij}} - \frac{\mathbf{N}_i}{c_t D_i^K} + \frac{x_i \mathbf{N}_{visc}}{c_t D_i^K} \quad (1.12)$$

Kerkhof [26] pointed out several inconsistencies in the derivation of DGM. The inconsistencies of DGM have been discussed in detail at a later stage in this thesis (see section 3.2.2).

Due to the inconsistencies in the DGM, Kerkhof [26] have proposed a new model, i.e. binary friction model (BFM). The BFM is based on Lightfoot equation presented earlier in eq. (1.11). The membrane friction parameter is evaluated for two conditions: pure viscous flow; and pure Knudsen flow. For pure viscous flow calculations, the component velocities are assumed to be equal to the mixture velocity. This assumption is only valid when the convective velocities are very high, and the individual species velocity perturbations can be neglected. The Knudsen transport and viscous transport are assumed to be in parallel, and the final BFM equation is given as [26]:

$$\frac{1}{p_t} \nabla_T p_i = RT \sum_{j=1}^n \Phi_{ij} \frac{(x_i \mathbf{N}_j - x_j \mathbf{N}_i)}{p_t D_{ij}} - \left(D_i^K + \frac{B_v}{\kappa_i} \right)^{-1} \frac{RT}{p_t} \mathbf{N}_i \quad (1.13)$$

where Φ_{ij} is a region based parameter, which is 1 in pure viscous flow region and 0 in pure Knudsen region.

Recently Vural et al. [27] presented a study on solid oxide fuel cell modelling using several mass transport models. The Maxwell-Stefan model, DGM and BFM were used for modelling mass transport in fuel cell electrodes. The results were compared with experimental polarization curves. The trends predicted by different models were fitted to experimental results for porous media tortuosity. The trends for all the models were found to be accurately matching with experimental results on fuel cells.

All of the mass transport models use transport properties to account for the effects of porous media. The three most important parameters in the models are: a) the permeability of the porous media; b) molecular diffusivity of the gases, and; c) Knudsen diffusivity of the gases. In order to use the theoretical models for mass transport predictions, the transport properties of the porous media must be known. The following sections describe the estimation of different mass transport parameters.

1.2.3 Molecular Diffusivity Measurements in Porous Media

The molecular diffusivity for a pair of gases is a kinetic parameter, which defines the diffusion rate in a mixture. The diffusion coefficient for a pair of gases is given as [28]:

$$D_{ij} = \frac{0.00266T^{3/2}}{PM_{ij}^{1/2} \sigma_{ij}^2 \Omega_D} [m^2/s] \quad (1.14)$$

where M_{ij} is the harmonic mean of molecular weights of i and j , σ_{ij} is the arithmetic mean of Lennard -Jones interaction parameter (σ) of i and j and Ω_D is the collision integral.

The diffusion coefficient obtained from eq. (1.14) is called as the bulk diffusivity. It can be used to calculate diffusion rates across capillaries, pores and other well defined paths. However, in a porous media the transport path is not well defined and the presence of media itself affects the net transport as well. To find averaged flux across porous media, the net available area for mass transport must be taken into account. The porosity or void fraction of porous media is used to account for the reduced mass transport area. Another restriction in porous media is the tortuous path the gas molecules have to take compared to a straight pore/capillary. This is accounted by the tortuosity of the porous media. The effective diffusivity of a gas pair in porous media is given as [26]:

$$D_{ij}^{eff} = \frac{\epsilon}{\tau} D_{ij} \quad (1.15)$$

where ϵ is the porosity (void fraction) and τ is the tortuosity of the porous media.

The most common correlation used for estimation of tortuosity is the Bruggeman [29] equation. The Bruggeman equation is developed for a packed bed of spheres with distributed range of diameters [30]. It is given as follows [30]:

$$\tau = \epsilon^{-0.5} \quad (1.16)$$

The structure of porous media in PEM fuel cells consists of cylindrical fibers bonded together in a random fashion. It was shown that the Bruggeman correlation is only accurate for a large range of particle sizes and does not predict tortuosity for cylindrical objects very well [31]. The Bruggeman equation is based on an effective medium approximation. Several other models have been presented based on Percolation theory, which assume a percolation threshold of porosity, below which no transport can occur. Tomadakis and Sotirchos [32, 33] have presented the following correlation for tortuosity:

$$\tau = \left(\frac{\epsilon - \epsilon_p}{1 - \epsilon_p} \right)^\alpha \quad (1.17)$$

where ϵ_p is the percolation threshold and α is dependent on ϵ_p .

Zamel et al. [4] recently presented mass transport studies in gas diffusion layers of a PEM fuel cell. The mass transport results were compared with various effective diffusivity correlations available in literature. It was concluded that all the models in literature overpredicted the diffusivity by 3-4 times. In other words, the tortuosity of the porous media was underpredicted by 3-4 times. Continuing on this work Zamel et al. [34] proposed new correlations for effective diffusivity by combining the

experimental results with a numerical model of random porous media. To determine the correlation, the porous media was reconstructed via a digital stochastic method. The reconstruction was done by assuming infinitely long cylindrical fibers in a Poisson line distribution. The reconstruction parameters were optimized to match the macroscopic data like porosity and pore size distribution with experimental results. Fick's second law was then solved in the void space and the effective diffusivity was obtained in both in-plane and through plane directions. It was found that a percolation limit exists in the porous media, which is in the range $0.2 \leq \epsilon_p \leq 0.3$. The results of the model were found to be in good agreement with experimental results. The diffusivities for in-plane and through plane directions were found to be significantly different, thus challenging the conventional assumption of an isotropic porous media.

Several other researchers have investigated mass transport in porous media to find effective diffusivity values. Lamanna and Kandlikar [30] and Fluckiger et al. [35] have done mass transport studies in porous media to find the effective diffusivity values. Baker et al. [36], Kramer et al. [37], Stumper et al. [38] and Ye and Wang [39] have performed experiments on fuel cell performance to predict the mass transport in electrodes. All of the studies agree on the fact that the conventional correlations like Bruggeman equation are highly overpredicting.

Friedman et al. [40] presented a study on diffusion coefficients in pore structures and its description by capillary models. The pore network was assumed as an array of cylindrical pores on a cubic lattice. The porous media was considered as an assembly of parallel capillaries. The transport in all the pores was considered to be in parallel, thus neglecting any pore connectivity. The effect of tortuosity was taken into account for prediction of apparent diffusion coefficients. The Monte Carlo method was used to predict the diffusion coefficients, and it was observed that apparent molecular diffusion coefficient does not depend directly on either the absolute mean pore size, or the standard deviation, but only on their ratio - the coefficient of variation. In the Knudsen region the apparent diffusion coefficient was found dependent upon the mean pore size.

The fuel cell gas diffusion layers and micro porous layers are random porous media. In this case, a well defined relation can not be obtained between tortuosity and porosity. The porosity is a volume averaged property which depends only on the amount of void space. On the other hand, tortuosity not only depends on the amount of void space but also its distribution and connectivity in porous media. Figure 1.5



Figure 1.5 – The tortuosity comparison of two porous media with same porosity

shows two structures of a porous media which have the same void space distributed in two different manners. It can be seen that in one case the transport is in a straight line ($\tau = 1$), however in the other case the tortuosity is significantly different.

To avoid the porosity based approach in effective diffusivity measurement, two approaches are possible. Either a pore scale model can be developed to take into account the micro-structure of the porous media, or experimental measurements can be done to measure effective diffusivity. In this study, an experimental technique has been adopted for the analysis. Several mass transport techniques are present to measure diffusivity of the porous media. The following subsection presents a brief overview of several mass transport techniques with their advantages and limitations.

Measurement Methods for Diffusion

Marrero and Mason [41] have presented a detailed discussion of all the experimental methods used for measurement of diffusion till 1972. All the conventional methods of diffusivity measurement have been explained in detail. The effects of various parameters e.g. temperature and pressure on diffusion coefficient measurements have also been discussed. Marrero and Mason [41] have divided the experimental techniques in three categories; major, minor and miscellaneous, based on their reliability, accuracy and use in literature. Reliability and uncertainty analysis are also presented for major methods. A summary of the recent mass transport experimental methods is presented in the Landolt Bornstein Series [42].

The two bulb method was developed by Nay and Armistead in 1947 [41]. In this experiment two bulbs are connected by a narrow tube /porous media as shown in Fig. 1.6(a). To study bulk diffusivity, an open tube is used; and to find effective diffusivity, a porous media sample is put in between the two bulbs. The bulbs are

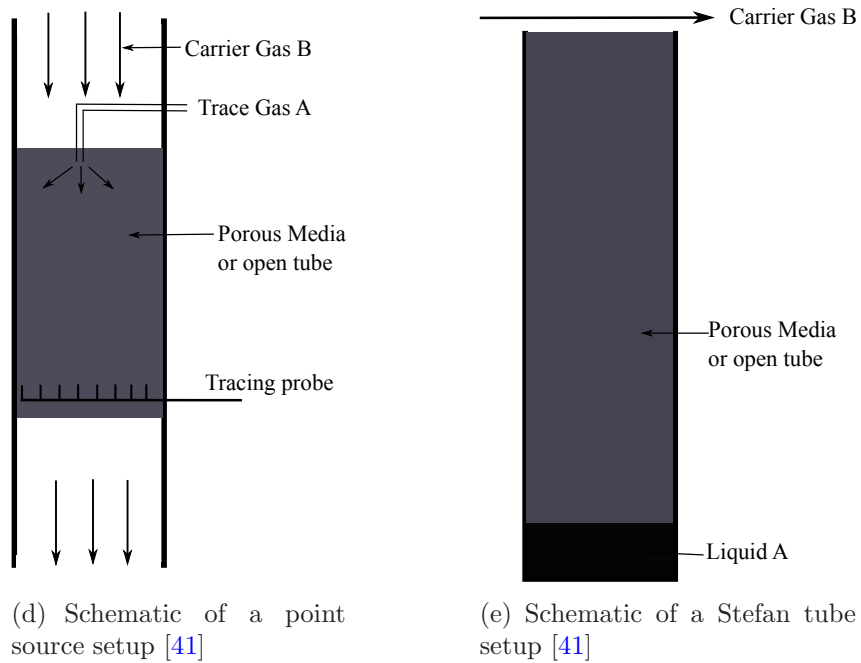
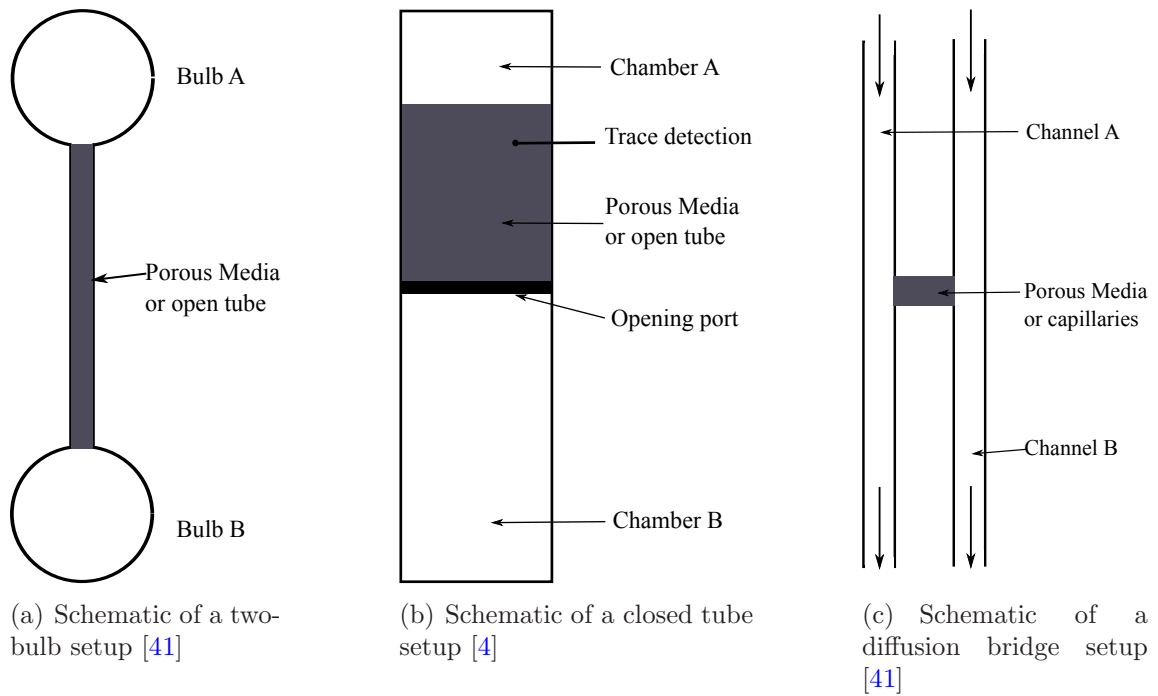


Figure 1.6 – Experimental schematics for different diffusivity measurement techniques

filled by different gases for analyzing binary diffusion. This setup has been used in a broader temperature range to determine diffusion coefficients. The data processing for two-bulb method involves an assumption of constant temperature and pressure. A quasi steady state is also assumed, which imposes a constant flux along the tube. The composition gradient is assumed to be contained completely inside the tube. With these assumptions, Fick's second law gives an exponential solution for concentration vs time. The experimental data can be fitted to the analytical solution to get diffusion coefficients.

The errors and uncertainties in this experiment are attributed to the assumptions in the solution. To achieve ideal quasi steady state, the bulbs should be infinitely large compared to the tube. To reduce this error, bulb sizes are kept quite large compared to tube size. The composition gradient is not contained entirely in the tube, because the gradient does not truncate immediately at the tube end. To account for this error an end correction length is added. The accuracy of diffusion coefficients by this method has been reported in the range of 0.1-0.2% [42]. The two bulb technique is currently the most common technique used for determination of diffusion coefficients due to its ease of construction and high accuracies. This method also has an advantage in its operating range of temperature. This technique has been used to study noble gas systems in the range 350 -1300K [42].

The closed tube method was first proposed by Loschmidt in 1870 [41], on his name this method is sometimes also referred as Loschmidt Cell method. Two chambers containing different gases are interconnected by a tube or a porous media and are initially isolated as shown in Fig. 1.6(b). During the experiment the gases are allowed to interdiffuse, and the change in composition at any location is measured with time. The basis of all the determinations in this method is Fick's second law in one dimension. Various analytical solutions are available for this equation under several assumptions. According to the experimental requirements, corresponding analytical solution can be used. The experimental measurements are fitted to the analytical solution to obtain the diffusion coefficient.

The experiment involves measurement of composition, temperature, pressure, geometry and time[41]. With help of modern instrumentation, the measurement errors can be almost eliminated. However, there are several other factors which contribute towards the error in results. Convective flow can be generated in the tube due to buoyancy, temperature gradient or opening of valve, which causes error in the mea-

surement. To avoid convection due to buoyancy, it has been suggested that the lighter gas should be put in upper section. The dependence of diffusivity on mixture composition may also introduce some errors. Dufour effect also contributes towards the uncertainties in the result [41]. The closed tube method is a transient measurement method, and thus very accurate measurement with respect to time are necessary. At the beginning of the experiment the data obtained will be noisy due to dominant effects of the uncertainties. However after some time the errors will start dampening, as the diffusion becomes steady. The accuracy of this method has been found in the range of 1 to 3%, with reproducibility of 2%. In some new studies proposed in late 1990's, diffusion coefficients have been determined with accuracy of $\pm 0.7\%$ with the close tube method [42]. This experiment has been used to find diffusion coefficients for binary gas pairs in the temperature range of 195 to 478 K. At higher temperatures construction and operation of this setup becomes difficult.

Rohling et al. [43] have used the closed tube setup to measure binary diffusion coefficient for different gases. For detection of concentration in the tube, a photothermal deflection technique was used. This technique has a better accuracy and response than conventionally used gas sensors. Astrath et al. [44] have used the closed tube setup to investigate the effect of water vapours on $O_2 - N_2$ binary diffusion. To detect the oxygen concentration, an oxygen sensor was used. It was concluded that water vapour do not affect the mass transport process, hence it can be considered as a binary transport. Zamel et al. [4] have used a similar setup presented by Astrath et al. [44] to measure effective diffusivity of fuel cell GDLs. They found that the conventional models like Bruggeman equation, highly underpredict the mass transport limitations in fuel cell porous media.

The diffusion bridge method is a steady state diffusivity measurement technique which was presented by Bendt [45]. The basic schematic of a diffusion bridge setup is shown in Fig. 1.6(c). The setup consists of two flow channels with different gases flowing in each channel. The flow channels are connected together by porous media or capillaries through which the mass transport occurs. The mass transport can be due to composition difference, or pressure difference or both. The gas composition at one of the channel exits is measured to find the transported flux through the bridge. Bendt [45] used the diffusion bridge technique to determine diffusion coefficients of hydrogen and helium isotope pairs ($H_2 - D_2$ and $He^3 - He^4$). The main sources of error in this technique are the fluctuations in the flow rate and pressure in the flow channels.

Remick and Geankoplis [46] have used the diffusion bridge technique to study mass transport in micro capillaries. The studies have been done with a binary mixture in the transition region between Knudsen and molecular diffusion. The systems pressure was as low as 0.444 mm Hg in order to have Knudsen diffusion in the micro capillaries. The experimental results were found to be in agreement with Graham's law with high accuracy in the transition region. Remick and Geankoplis [47] further studied ternary diffusion of a He-Ne-Ar mixture in micro capillaries using the same setup.

Evans III et al. [48] have used the diffusion bridge to study diffusion of gases through low permeability graphite at uniform pressures. The experiment consisted of a low permeable graphite block, with helium flowing on one side and argon flowing on another side. After characterization of the graphite specimen for its porosity and permeability, interdiffusion experiments were carried out. The main objective was to verify the dusty gas models at intermediate Knudsen numbers. It was found that this model gives accurate results at intermediate Knudsen values ($\simeq 1$). Using the kinetic theory of gases, a gas diffusion model in porous media was presented and verified.

Evans III et al. [49] presented a study continuing from their previous work [48] of diffusion in graphite. The study focused on effects of pressure variations on interdiffusion. The pressure gradients give rise to viscous fluxes. The studies were carried out between normal and Knudsen regions. The solution of simple diffusion was extrapolated and the total flux was considered to be sum of diffusive flux and forced flow flux. The results indicated that the effective diffusion coefficient increased with increase in the pressure gradient. At very high pressure gradients, the diffusion amount could not be predicted by the relations very accurately.

Henry Jr. et al. [50] have also presented a study on diffusion of gases in porous media using the diffusion bridge technique. Nitrogen and helium flow through the two channels, and diffuse through porous alumina. The thermal conductivity of the output streams was measured and compared to conductivities of pure nitrogen and pure helium to know the composition. It was found that Knudsen diffusion dominates up to the 300 mm Hg pressure. The results from the experiment were within the range of 5% to 30% of the values from various models. At higher pressures the errors were less. Using a correct tortuosity value in their calculation, the errors were reduced to 6.29%.

Reist [51] have presented a study on diffusion coefficients of Krypton- air in porous media using diffusion bridge technique. The incoming and outgoing streams of air were analyzed in a spherical ionization chamber for observing krypton activity. The amount of diffusion can be found out by knowing the difference in Krypton activity of the two streams. The errors in the experimental values was found to be less than 10%.

The point source method is based on the dispersion of a tracer gas in a carrier gas flow stream. It was first proposed by Westenberg and Walker in 1957. The schematic of the technique is shown in Fig. 1.6(d). An injector tube injects the tracer gas in a steady, laminar and fully developed flow of carrier gas. The mixture composition is measured by probes at different distances downstream. The boundary conditions and various assumption has been discussed in detail by Marrero and Mason [41]. The main assumptions are of steady flow, axially symmetric concentration profile, uniform flow velocity and very dilute concentration of tracer so that density can be taken as constant. The various sources of error in this experiment are: wake caused by injector, difference in density of tracer and carrier gas, and variation in flow rate of carrier gas. The instrumentation errors in this experiment can range from 2-5% depending upon the instruments. At lower temperatures, the accuracies of this experiment are about 4% [41]. At higher temperatures larger deviations have been observed.

The evaporation tube method was proposed by Stefan in 1873. Sometimes also referred as Stefan Cell Method, this method has been extensively used for determination of diffusivity in liquid gas mixtures. As shown in Fig. 1.6(e), the tube is filled with liquid, and gas flows over it to carry away all the vapours. The evaporation rate of the liquid is controlled by diffusion through the stagnant gas in the tube. The loss of liquid is measured over long durations to determine the diffusivity. The temperature range in this experiment is limited by the volatility of the liquid. The assumptions are similar to the close tube experiment. The results obtained from this experiment need to be end corrected, for the tube length. Slight change in temperature and pressure may cause significant error. As the experiment runs for very long durations, the chances of temperature and pressure variations are quite high. Non equilibrium state and non ideal nature of the gases also contributes towards the error. Although widely used, this method have high uncertainties in diffusion prediction. Recently Whitaker [52] presented a study on Stefan tube, showing that the assumption of stagnant gas layer is invalid. Due to the momentum transport across the tube a velocity profile develops which causes circulations in the gas layer.

Table 1.1 – List of the experimental methods used for diffusivity measurement

Method	Proposed by	Year	Use	Accuracy
Closed Tube	Loschmidt	1870	High	Very Good
Two Bulb Method	Ney and Armistead	1947	High	Very Good
Point Source	Walker and Westenberg	1958	Low	Average
Evaporation tube	Stefan	1873	Very High	Low
Gas Chromatography	Giddings and Seager	1960	Low	Average
Open Tube	von Obermayer	1882	Low	Average
Back Diffusion	Hartceck and Schmidt	1933	Low	Average
Capillary Leak	Klibanova	1942	Low	Poor
Unsteady Evaporation	Arnold	1944	Low	Good
Diffusion Bridge	Bendt	1958	Low	Average
NMR spin echo technique	N/A	1991	Low	Good
Optical Interferometry	Gouy	1984	Low	Good
Holographic Interferometry	N/A	N/A	Low	Average

Several other methods are also available for diffusion coefficient measurements. Modern instrumental techniques like NMR spin echo technique, interferometry, holographic interferometry, light scattering and chromatographic methods can be used for diffusion coefficient measurement. Table 1.1 shows a consolidated list of several diffusivity measurement techniques.

For the current research, the diffusion bridge technique was chosen for diffusivity measurements. The main advantage of the diffusion bridge is the ability to study mass transport over its entire range of pure diffusion, pure convection and convection-diffusion. The pressure in both the flow channels can be controlled precisely, giving a net pressure gradient across porous media to facilitate convection. Additionally, the diffusion bridge is a steady state technique. Therefore real time measurements are not needed. This reduces the complexity and uncertainty in the experiment, as the transient experiments need to have accurate time measurement. This also reduces the complexity of mass transport models necessary to interpret the results. Compared to transient techniques like two-bulb method and closed tube method, the measurements are not done in the transport zone. The measurements are done at the end of channels and no intrusive probes are needed, which results in better accuracy of this technique.

1.2.4 Permeability Estimation in Porous Media

The viscous interaction of porous media with species movement creates a boundary layer within the pore. This boundary layer causes a viscous friction force on the species. The overall viscous effects of the porous media are characterized by the absolute permeability.

Van Doormaal and Pharoah [53] have presented a study on permeability prediction of porous media in PEM fuel cells. A lattice-Boltzmann method was used to simulate flow in a random porous media with cylindrical fibers. The flow data was fitted to Darcy's equation to obtain permeability values for in-plane and through plane directions. This technique of permeability measurement is quite complex and does not take into account the effects of PTFE binder and non cylindrical fibers.

Gostick et al. [54] have presented through plane and in plane permeability measurements for GDLs of PEM fuel cells. The flow was forced to go through/ across the porous media and the corresponding pressure drop was observed. The experimental data was fitted to Darcy's equation to obtain the permeability value. Most of the materials were found to have higher in-plane permeability compared to through-plane permeability. The effects of compression on the GDLs were also presented.

Gurau et al. [55] have presented through-plane and in-plane permeability measurements in fuel cell GDLs and GDL-MPL assemblies. The flow rate vs pressure drop data was fitted to Darcy-Forchheimer equation. By using a resistance network analogy for the porous assembly, the permeability values of GDL and MPL were separately evaluated. The study also presented the effect of PTFE content and different carbon types on the permeability.

In the current research, the permeability estimation has been done by performing flow experiments on porous media. A setup is used which is similar to the one used by Gostick et al. [54] and Gurau et al. [55] for through plane permeability measurements. Darcy-Forchheimer equation has been used for preliminary permeability estimations.

1.2.5 Knudsen Diffusivity Estimation in Porous Media

For very small pore sizes or for rarefied gases, the molecule wall interactions become highly dominant. In this case, the Knudsen friction governs the species transport. The effect of wall collisions on a species is calculated by its Knudsen diffusivity, given

as follows [56]:

$$\begin{aligned} D_i^K &= 0.89D_{i0}^K \\ D_{i0}^K &= \frac{2}{3}r_p \left(\frac{8RT}{\pi M_i} \right)^{1/2} \end{aligned} \quad (1.18)$$

where r_p is the pore size and M_i is the molecular weight of the species. For very large pore radius, the diffusivity is quite high and thus the Knudsen friction is negligible. To find Knudsen diffusivity in porous media, the effects of porosity and tortuosity must be included. The effective Knudsen diffusivity in the porous media is given as follows:

$$D_i^{K^{eff}} = \frac{\epsilon}{\tau} 0.89 \times \frac{2}{3}r_p \left(\frac{8RT}{\pi M_i} \right)^{1/2} \quad (1.19)$$

The tortuosity in this equations is the same as used in molecular diffusivity estimations. The pore radius is not very well defined for a porous media due its distributed nature and also due to connectivity of the pores.

One way to predict the effective Knudsen diffusivity is to use the pore size distribution of the porous media. Weber et al. [57] have presented an estimation of effective pore radius from the pore size distribution of the porous media. The effective pore radius can be used to find overall Knudsen diffusivity of the porous media. However, the estimation of pore size distribution requires mercury intrusion porosimetry experiments.

The Knudsen diffusivity of a porous media can also be found by performing the permeability measurements in the transition region between pure viscous flow and pure Knudsen flow [21]. The apparent permeability values obtained by this experiment include the effect of permeability as well as Knudsen diffusivity. By repeating the experiment with two gases, the effects can be separated. As the experiment is being done on a porous media, the estimated Knudsen effects are already averaged over the porous media. This eliminates the need to measure pore size distribution, porosity and tortuosity for Knudsen diffusivity estimations.

In the current research, the technique suggested by Kast and Hohenthanner [21] has been used for Knudsen diffusivity estimation. As the permeability measurements have to be performed anyway, this provides an easy way to estimate Knudsen diffusivity. Later on, the BFM has been used to derive an equation for permeability and Knudsen diffusivity estimation in the transition region. The obtained equation is similar to the one presented by Kast and Hohenthanner [21].

1.3 Contributions

The main contributions of this research are in the area of mass transport analysis of fuel cell porous media. The contributions to the area of mass transport are:

- Development of an experimental setup based on diffusion bridge technique to study various modes of mass transport, viz. pure diffusion and convection-diffusion in porous media.
- Development of an experimental setup to study convective flow in porous media for permeability measurements.
- Experimental measurements of mass transport in fuel cell gas diffusion layers and micro porous layers.
- Development of a theoretical and numerical model of mass transport in porous media that corrects the inconsistencies in previous theories.

Several contributions of this work have been presented for the first time in literature, such as:

- Experimental measurement of both diffusive and convective-diffusive transport in fuel cell porous media.
- Development of a theoretical model of mass transport with least number of assumptions.
- Using a transitional model of mass transport in fuel cell micro porous layers for estimation of permeability and Knudsen diffusivity.

1.4 Structure of the Thesis

This thesis is divided into five chapters. This first chapter presents the motivation of this research and a literature review of earlier research in : mass transport modelling; transport properties estimation and; experimental techniques of mass transport measurement. Chapter 2 presents the the design of experimental setups for mass transport measurement and permeability measurement. A description of all the components and the accuracy of experimental measurements is also presented in the chapter. Chapter 3 describes the conventional models of mass transport in porous media such as Fick's law, DGM and BFM. Their limitations are also described. To correct the inconsistencies of the conventional model, development of a new mass transport model

is presented. Numerical simulation results on all the models are then presented to highlight the differences between them. Chapter 4 presents the experimental results on mass transport measurements. The experimental data is analyzed by using the different mass transport models. A new approach for Knudsen diffusivity measurement is also presented. This is followed by validation and sensitivity analysis of the experimental results. Finally, chapter 5 summarizes the key findings of this research and possible pathways of future research.

Chapter 2

Experimental Setup

This chapter describes the design and fabrication of the experimental setup used to investigate mass transport in porous media. As discussed in chapter 1, the three most important parameters governing mass transport in a porous media are the effective diffusivity, permeability and pore size distribution (Knudsen diffusivity). The pore size distribution studies have not been performed in this research. This chapter discusses the experimental setups for measurement of effective diffusivity and permeability of the porous media.

The various design requirements of the diffusivity measurement setup are presented in section 2.1. The schematics of the proposed experimental setup are discussed in section 2.1.1. The fabrication and assembly of the diffusion bridge chip is discussed in section 2.1.2. Various controlling and monitoring equipments of the setup are described in sections 2.1.3 – 2.1.6. The experimental procedure for diffusivity measurements is presented in section 2.1.7, which is then followed by an uncertainty analysis of the experimental setup in section 2.1.8. The experimental setup design for permeability measurements is presented in section 2.2, followed by an uncertainty analysis in section 2.2.1.

2.1 Experimental Setup for Mass Transport Measurements

In a PEM fuel cell electrode, both convection and diffusion are present [53]. To study the mass transport in a detailed and precise manner, the experimental setup should be able to capture both transport mechanisms. Most of the mass transport measurement methods are only able to study pure diffusion. However, in the current study, both pure diffusion and convection-diffusion need to be studied. Based on this

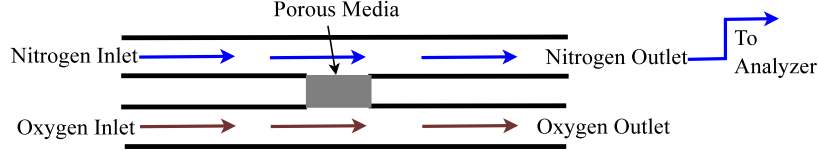


Figure 2.1 – Basic schematic of a mass transport measurement setup based on diffusion bridge

requirement, the diffusion-bridge/counter-diffusion method [41, 46, 58, 59] has been chosen for mass transport experiments. Compared to other methods, the diffusion bridge offers an advantage of controlled pressure gradients across porous media, which is necessary for convection-diffusion studies.

Based on the experimental technique requirements, the basic setup for diffusivity measurement can be designed as shown in Fig. 2.1. Oxygen and nitrogen are the fluids in the two channels of the diffusion bridge in order to simulate the conditions in a PEMFC cathode. Other gases can also be used, for example: a mixture of oxygen-nitrogen has been used for validation in this research. The oxygen will travel to nitrogen channel due to composition and/or pressure gradients. The out-coming nitrogen stream has to be analyzed for oxygen amount, which will give the value of oxygen flux. In case of multicomponent mixtures, the analyzing equipment should be able to separate the different species and analyze their compositions. For this purpose a gas chromatograph can be used. In case of binary mixtures, simpler equipments such as thermal conductivity detectors or gas sensors can also be used. Due to availability of micro gas chromatograph in the research facility, it was chosen as an analyzing equipment for this experiment. The micro gas chromatograph separates all the components and can identify the fractions of different species in the mixture. In a binary mixture of oxygen and nitrogen, the oxygen fraction can be given as follows:

$$\omega_{O_2} = \frac{\dot{m}_{O_2}}{\dot{m}_{O_2} + \dot{m}_{N_2}} \quad (2.1)$$

where \dot{m}_{O_2} and \dot{m}_{N_2} are mass flow rates of oxygen and nitrogen in the output stream. To know the absolute amount of transported oxygen flux in the output stream, the mass flow rate of nitrogen stream must be known. Use of a mass flow controlling device can ensure a constant and measurable flow rate through the channels.

The main advantage of the diffusion-bridge/counter-diffusion technique is the ability to conduct convection-diffusion studies. However in order to have a well defined pressure gradient across the porous media, the pressure in the channels must be con-

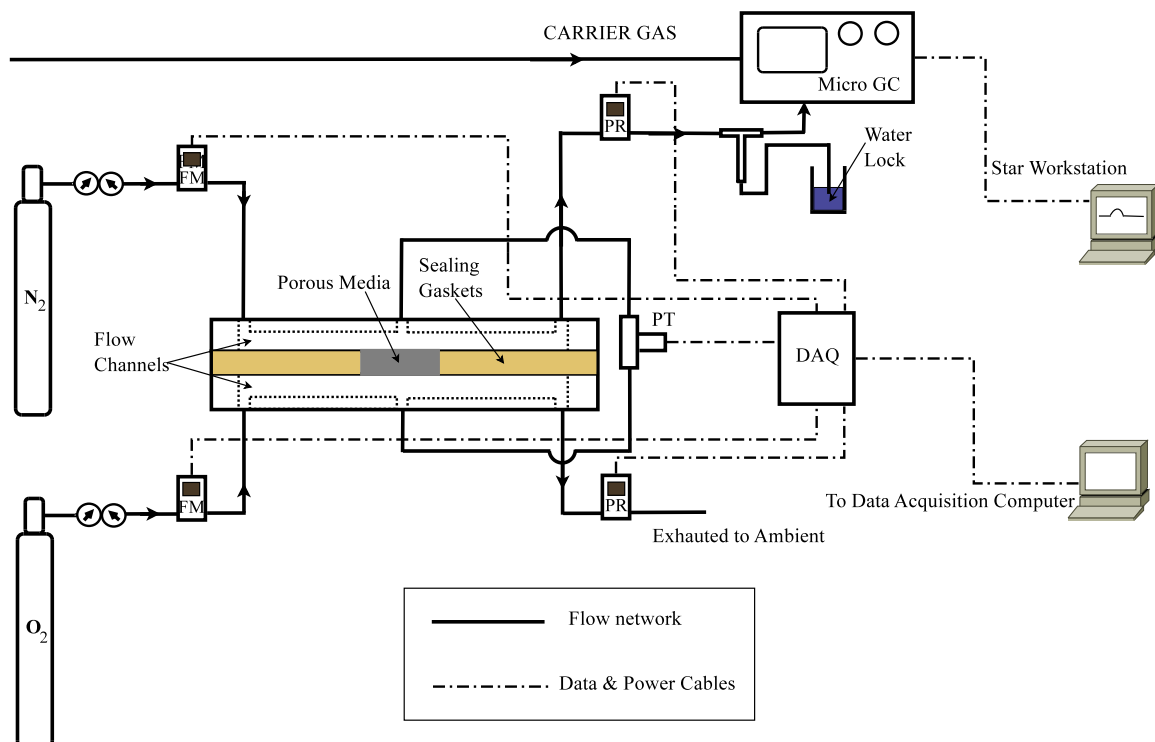


Figure 2.2 – Schematics of the mass transport measurement setup; FM: Mass flow controller, PR: Back pressure regulator, PT: Differential pressure transducer, DAQ: Data acquisition card, GC: Gas chromatograph

trolled. For this purpose, back pressure regulators can be used on each channel. To measure the pressure difference across the porous media as accurately as possible, a high sensitivity differential pressure transducer can be used. The next sections will describe the design/selection of each component of the experimental setup.

2.1.1 Schematics of Experimental Setup for Mass Transport Measurements

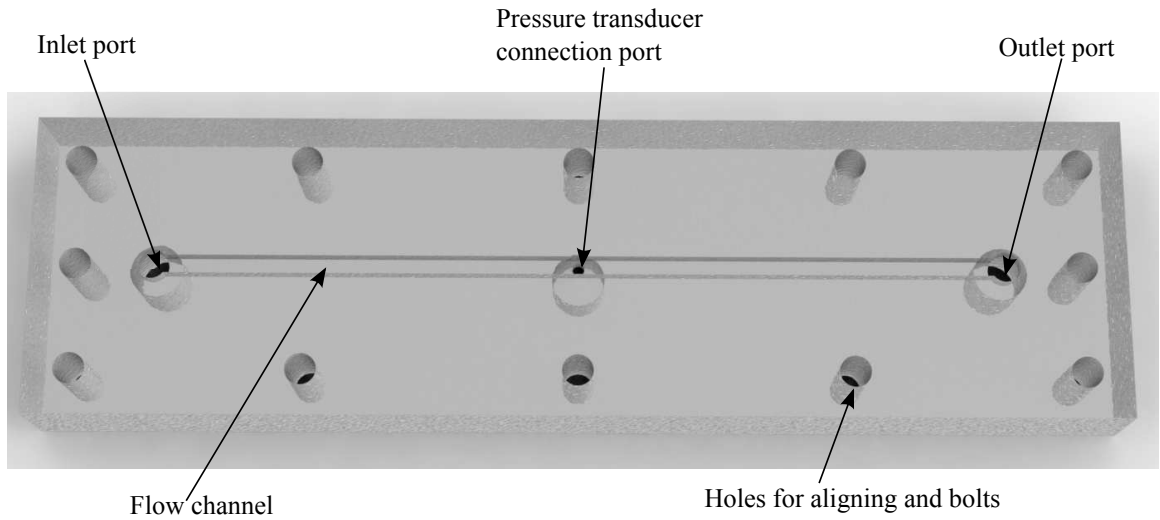
In this section, the experimental setup for mass transport (effective diffusivity) measurements is described. Based on the requirements of the experimental setup discussed, the schematics of the proposed experimental is shown in Fig. 2.2. The central part of the experimental setup is the diffusion bridge based chip. Several auxiliary control and monitoring systems are also required. The diffusion bridge chip and various controlling and monitoring components of the experimental setup are described in the upcoming sections.

2.1.2 Fabrication of Counter-diffusion Chip

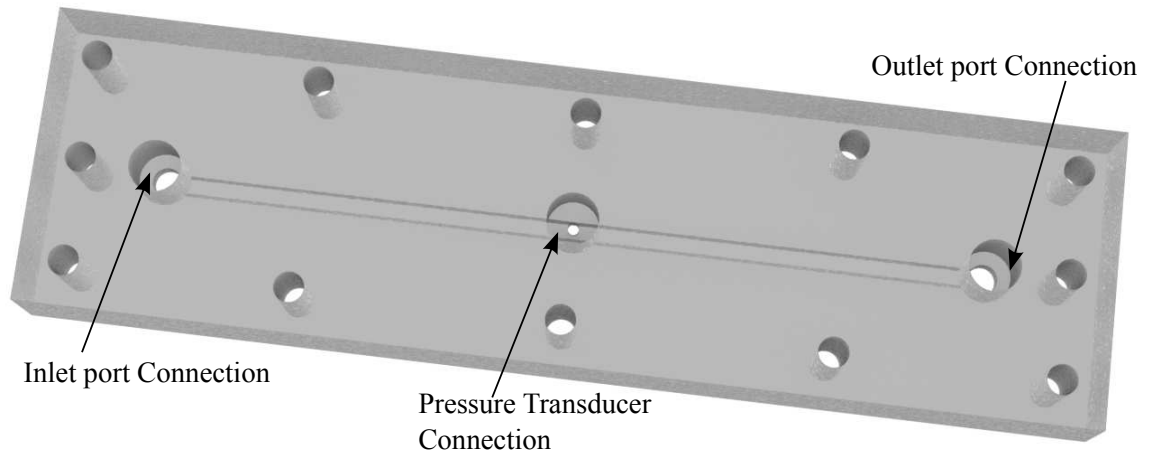
The central component of the experimental setup is the diffusion bridge based chip. As shown in Fig. 2.1, the design should have two separated parallel channels connected only through the porous media. For the current experimental setup, the flow channels were fabricated on an acrylic block by milling. The reason for selecting acrylic material is the ease of fabrication. Figure 2.3 shows a solid model of the machined acrylic chip. The acrylic chip has a flow channel of cross section $3\text{mm} \times 3\text{mm}$ milled on one side as shown in Fig. 2.3(a). The flow channel has the flow connecting ports on its ends, which are machined on the other side of the acrylic block. At the middle of the channel, a connecting port for a pressure transducer has also been machined as shown in Fig. 2.3(b). These connecting ports will be used to connect the flow channel to mass flow controllers and pressure regulators as discussed in section 2.1. Two such blocks were fabricated for oxygen and nitrogen flow channels. These two channels will be assembled together in a mirror image formation to make the final chip.

The flow channels should be separated and only connected through a porous media. For this purpose, a laminated porous media assembly is placed in between the acrylic blocks. Figure 2.4 shows the porous media assembly used in the experiments. The assembly is made by putting several layers of the porous media between two lamination sheets, where an aperture is made to facilitate mass transport. The assembly is then heat laminated to make a rigid and sealed porous media assembly. Holes were made on the sides of the sheet to align with the bolting holes in the acrylic block.

To make the assembly leak proof, a silicon gasket was used on each side of the porous media assembly. A sample of the used gasket is shown in Fig. 2.5. The central portion of the gasket is removed to accommodate the porous media assembly. Finally, all the components are assembled as shown in Fig. 2.6. The silicon gaskets and the lamination sheets separate the flow channels and also make the assembly leak proof. Once all the components are assembled, they are bolted together through the aligning holes. The final diffusion chip looks as shown in Fig. 2.7.



(a) An image of the machined acrylic block with flow channel and connections



(b) Inverted image of the machined acrylic block showing connections

Figure 2.3 – Images of the machined acrylic channel for the counter diffusion chip

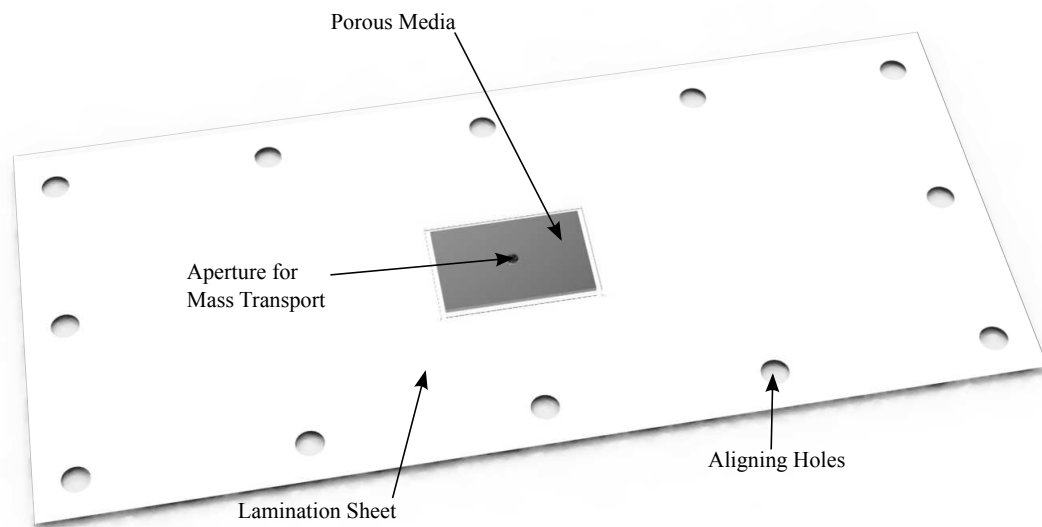


Figure 2.4 – The porous media assembly laminated in a polymer sheet

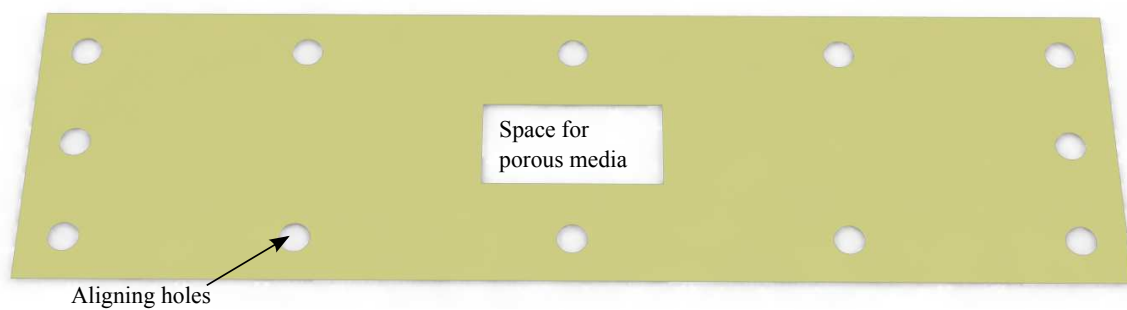


Figure 2.5 – The gasket used in diffusion bridge chip

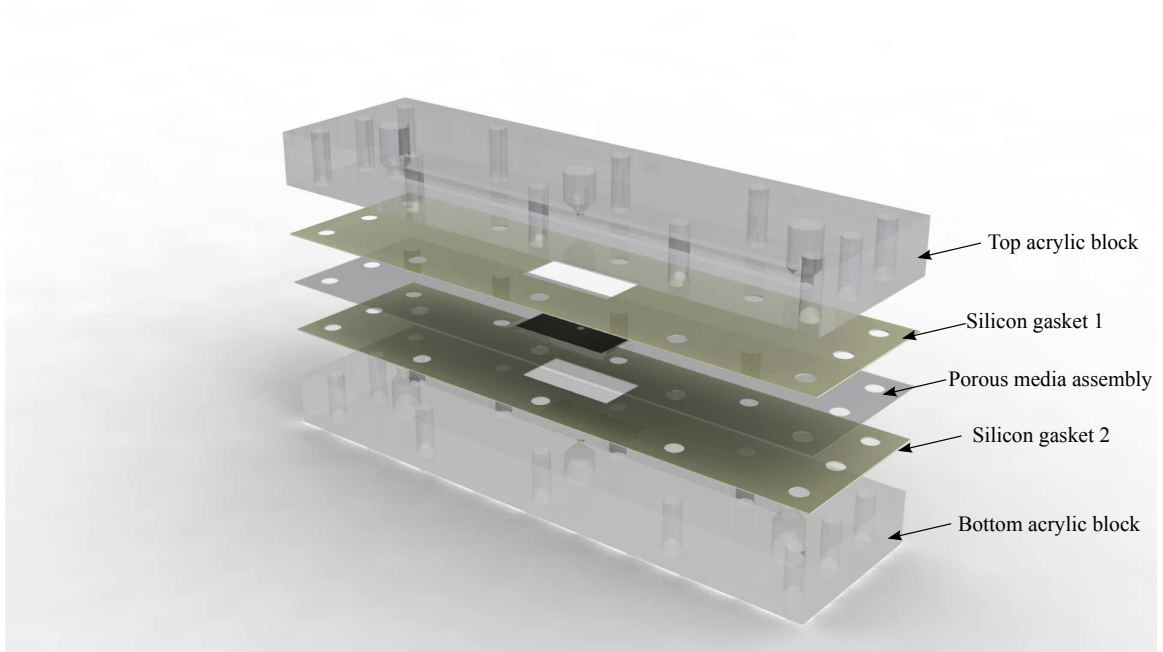


Figure 2.6 – An exploded view of the final diffusion bridge assembly

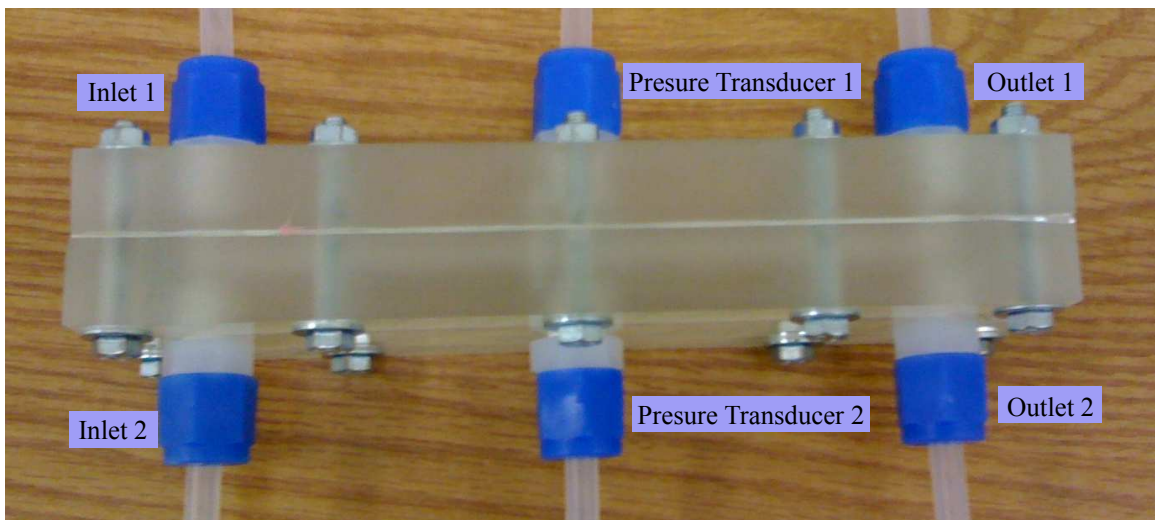


Figure 2.7 – A snapshot of the final diffusion bridge assembly

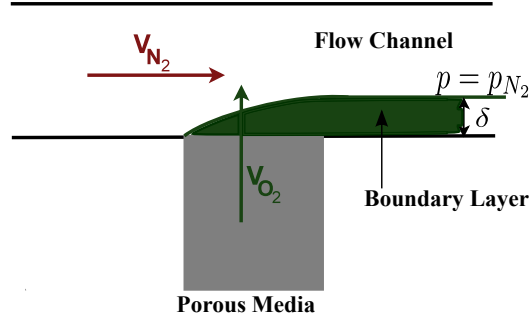


Figure 2.8 – Interaction of channel velocity and diffusive boundary layer in a diffusion bridge

2.1.3 Mass Flow Controllers

The flow rates of the gases in the flow channels need to be controlled and known for mass transport calculations. The mass flow rate is quite critical in functioning of the setup and needs to be within a specific range. If the mass flow rate is too high, the oxygen fraction will be too small to be detected by a micro-GC or any other detecting equipment. If the mass flow rate is too low then the flux coming through porous media will create a boundary layer, as shown in Fig. 2.8. For ease in numerical modelling, it is normally assumed that the oxygen coming to the channel is quickly swept away, hence the oxygen partial pressure in nitrogen channel is assumed to be zero. This assumption is only valid when $v_{N_2} \gg v_{O_2}$. Keeping these constraints in mind, two mass-flow controllers (Cole-Parmer, model: RK-32907-57) with a flow range of 0.5-50 ccm were used for controlling the mass flow rate. The accuracy of the flow controllers is $\pm 0.8\%$ of the reading and repeatability is $\pm 0.2\%$ of maximum value.

Figure 2.9 shows the comparison of velocity in the flow channels and velocity across porous media for a SIGRACET 34BC porous media. In this research, all the experiments were conducted for a pressure difference below 300Pa, to ensure that the velocity in the flow channels was sufficiently higher than velocity across porous media.

2.1.4 Pressure Controllers

In order to perform a convection-diffusion study, the pressure difference across the channels have to be properly controlled. To control the pressure in flow channels, two back pressure regulators (Cole-Parmer, model: NCI-00240MM) with a range of 0-1 psig are used. The accuracy of the pressure controllers is $\pm 0.25\%$ of maximum value. To measure the pressure difference across porous media, a differential pressure transducer (Omega, customized model: MMDDDB10WBIV10H2A0T1A2) of range 0–

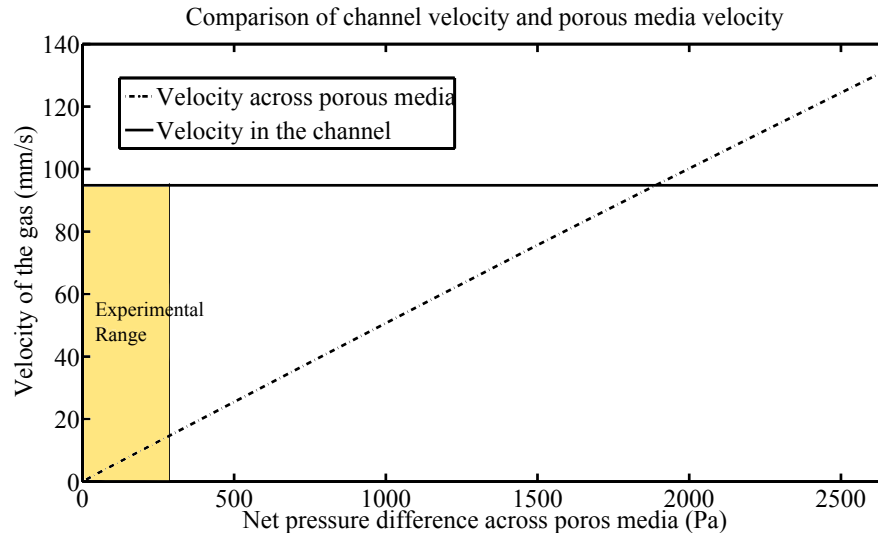


Figure 2.9 – Comparison of velocity in the flow channels with velocity across porous media for a SIGRACET 34BC

25 mBar is used. The transducer can record very small pressure changes with high accuracy, hence it is helpful especially for near zero pressure difference studies.

2.1.5 Gas Chromatograph

At the end of diffusion bridge, the nitrogen channel is connected to a micro gas chromatograph for analysis of the out-coming stream. Gas chromatography is a chromatographic mixture separation technique used in analytical chemistry. Also referred as gas liquid chromatography, it has most commonly been used to separate gas mixtures and vapours [60]. The early usage of this technique can be traced back to 1950s [61]. In later years, many critical chemical analysis methods, e.g. mass spectroscopy and infrared spectroscopy became dependent on gas chromatography for separation of complex mixtures. The gas chromatograph provided an accurate and fast platform for separation of gaseous and volatile compounds in a mixture. Eiceman [60] have discussed in detail the developments in the gas chromatography technology, from its beginning to the current highly efficient gas chromatographs.

Figure 2.10 shows a general schematics of the gas chromatograph (GC). In a chromatography experiment, a gaseous sample is moved along a column by a carrier gas. The purpose of the carrier gas is only to carry the sample. The column is mostly a long metallic tube, with an inner coating of a polymer with low vapour pressure [60]. When the sample components pass through the column, they travel at different speeds depending on the species. At the end of column, different gases elute at

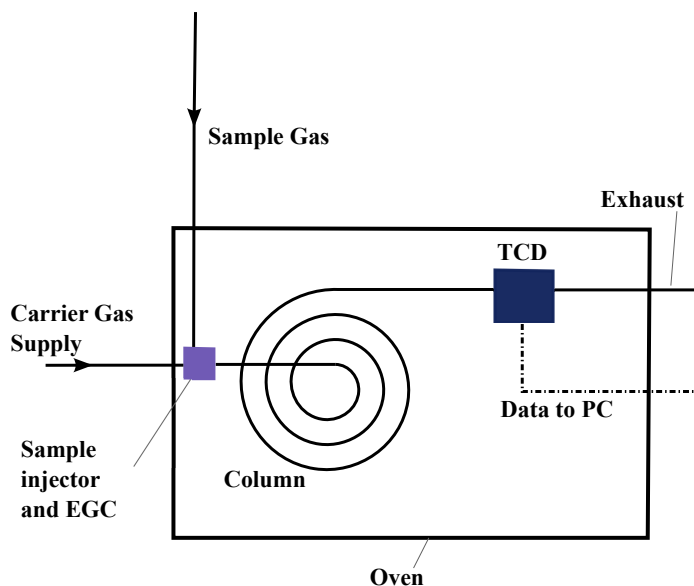


Figure 2.10 – The schematics of a gas chromatograph [62]

different times, and are sent to the detector. The most common detector used is a thermal conductivity detector (TCD), which measures the conductivity of eluting substances.

In this research, a micro gas chromatograph (Varian, model: CP-2003P) is used for analyzing the out-coming stream from the diffusion bridge. The micro GC can analyze components within concentration range of 1ppm-100%. It uses a TCD for detection and is also equipped with electronic gas pressure control (EGC) [62]. To analyze oxygen and nitrogen, helium is used as the carrier gas and the analyzing column is a molecular sieve column. The TCD sends the conductivity output as a voltage signal. The signal is sent to a computer equipped with interpretation software (star workstation), which analysis the conductivity data and plots a chromatogram for the stream.

Another additional equipment in the setup is a tee connection in the GC sampling line. The tee connection is used as a safety measure for GC. The micro-GC has an upper limit of sample gas pressure. However, even when the GC does not take a sample, the incoming sample stream from the diffusion bridge can create a pressure buildup. Hence the tee connection acts as a pressure relief valve in the sample gas line. The third line of the tee is water locked to ensure that no ambient gases will enter the sample through the tee connection.

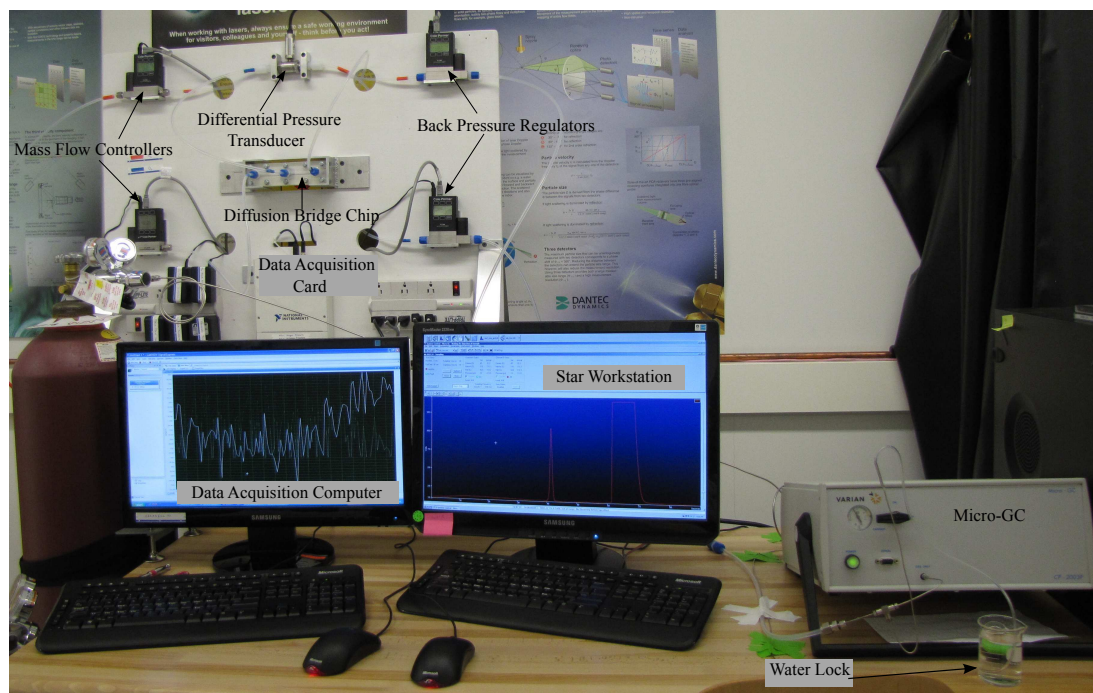


Figure 2.11 – A snapshot of mass transport experimental setup

2.1.6 Data Acquisition

The mass flow rates, pressures and other process specific parameters need to be continuously monitored. A data acquisition card (National Instruments, model: USB-6221) is used to collect data from mass flow controllers, pressure controllers and differential pressure transducer. The data acquisition card can sweep data at 250,000 sweeps/s and accepts voltage inputs within ± 10 Volts. With a sensitivity of around $100 \mu V$, this data acquisition card helps in capturing small pressure differences across the porous media. The data acquired by micro-GC and data acquisition card is finally sent to computers equipped with data post-processing software. A snapshot of the final mass transport experimental setup is shown in Fig. 2.11.

2.1.7 Experimental Procedure and Data Reduction

The experimental methodology used to obtain the species fluxes in the mass transport experiment is shown in Fig. 2.12. First, the diffusion bridge chip is assembled with all its components as shown in Fig. 2.2. Once the chip is assembled, leak tests are done on the setup by system pressurization and snoop solution. Before starting the experiments, the equipments need to be calibrated. The mass flow controllers, pressure controllers and pressure transducer output as a voltage signal, which can be converted to the relevant parameter by equipment manufacturer's calibration.

The micro-GC also needs calibration to convert its output to mass fraction. A sample chromatogram obtained from a gas chromatograph experiment is shown in Fig. 2.13. The chromatogram tracks the conductivity of the outcoming stream with time. The flat line in the chromatogram shows the conductivity of the carrier gas, which is also the reference line. The peaks show different components in the sample. The area under the peaks is proportional to the mass of corresponding species in the sample. Calibration is required to obtain a conversion coefficient between the area under the curve and the actual mass fraction of components.

In the current experiment, four calibration samples with varying oxygen proportions were used for calibration. The area count under the oxygen peak is proportional to the fraction of oxygen in the mixture. As the calibration is done over a large range of concentrations, the calibration curve is assumed to be piecewise linear. After adjusting for zero offset of the GC, the calibration curve of micro-GC is as shown in Fig. 2.14. Later on during experimentation, this curve can be used to find oxygen mass fraction in mixture, which can then be converted to oxygen flux using eq. (2.1).

The experimental setup can perform two types of studies: pure diffusion and convection-diffusion. The pressure difference across porous media can be changed by changing the pressure in channels. For pure diffusion study, the pressure in both channels is kept the same. In this case, the pressure difference between the channels should be zero. However, due to fluctuations in the pressure, getting an absolute zero pressure difference is not feasible. A closest possible value to zero is used for the experimentation. The oscillations in the pressure were around $\pm 3Pa$.

For convection-diffusion studies, the pressure in the channels has to be different. To study oxygen convection into nitrogen channel, nitrogen channel pressure is reduced and vice versa. Once the desired pressure difference is achieved, chromatographic analysis of the outcoming stream is performed. To ensure steady-state in the diffusion bridge, several chromatographic analysis were performed until the oxygen area count is steady with $\pm 3\%$. The final area count is used to calculate the oxygen fraction in the outcoming stream. This analysis is repeated with changing pressure difference across porous media. The oxygen flux vs pressure difference profile can then be used with theoretical models to get mass transport properties of porous media.

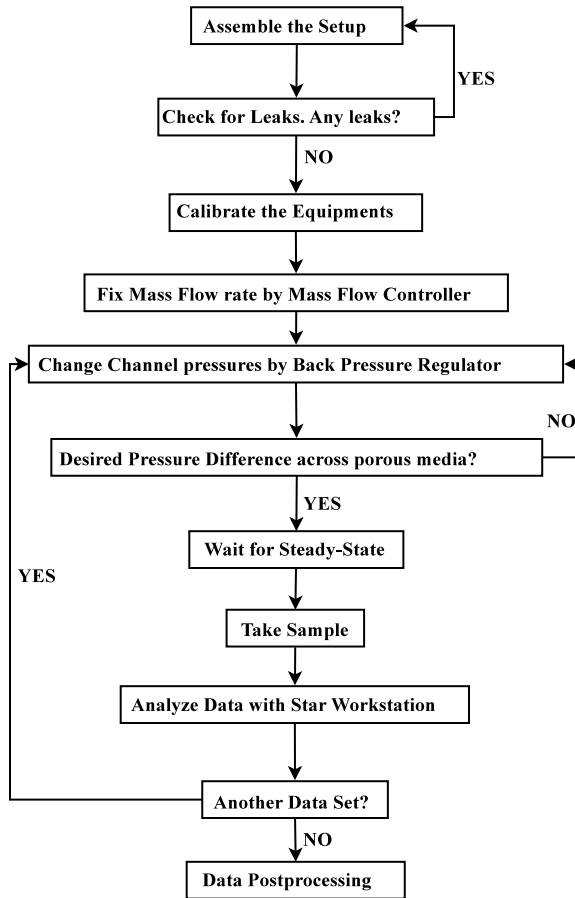


Figure 2.12 – Flow chart for mass transport measurements

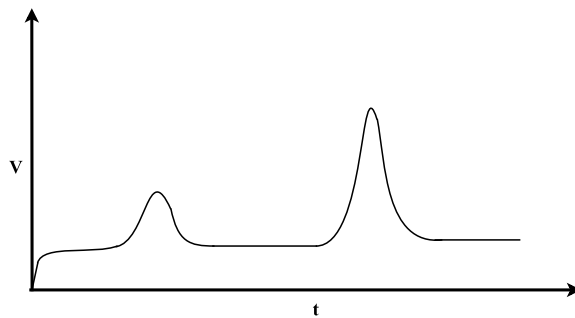


Figure 2.13 – A sample chromatogram obtained from chromatography experiment

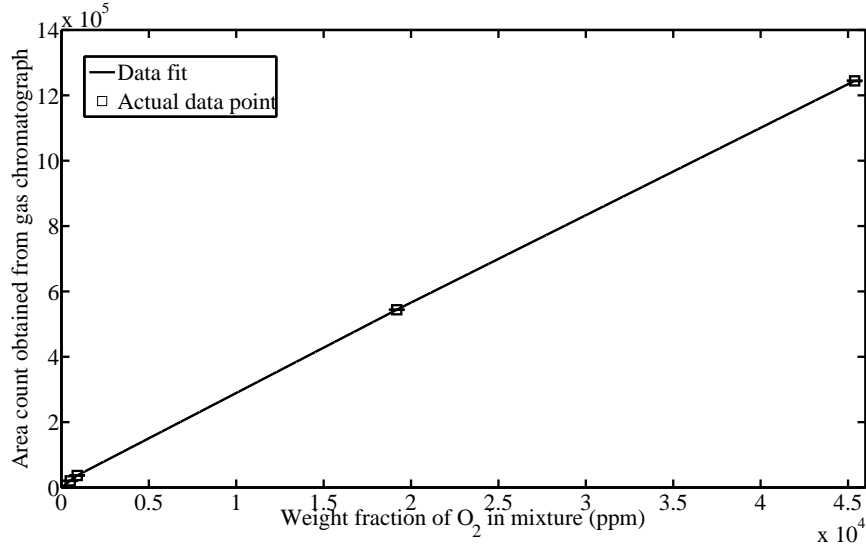


Figure 2.14 – The calibration curve for micro-GC under medium sensitivity of TCD

2.1.8 Data Error Analysis for Mass Transport Measurement

There is always an uncertainty in the data obtained from experiments. This uncertainty can be due to several reasons, such as fluctuations in operating conditions, equipment control uncertainties and external influences. An error analysis on the experimental results can be helpful in determining the margin of error for final results. Using eq. (2.1), the equation for oxygen mass fraction in mixture can be given as follows:

$$w_{O_2}(ppm) = \frac{\dot{m}_{O_2} \times 10^6}{\dot{m}_{O_2} + \dot{m}_{N_2}} \quad (2.2)$$

The oxygen fraction can also be given as follows:

$$w_{O_2}(ppm) = \frac{A}{c} \quad (2.3)$$

where A is the area count from micro-GC measurements and c is the calibration constant. By rearranging the terms of eq. (2.2), the following expression can be obtained for oxygen flux:

$$\dot{m}_{O_2} = \frac{\dot{m}_{N_2} \times w_{O_2}(ppm)}{10^6 - w_{O_2}(ppm)} \quad (2.4)$$

Taking logarithm on both sides of the equation above, the following equation is obtained:

$$\ln(\dot{m}_{O_2}) = \ln(\dot{m}_{N_2}) + \ln(w_{O_2}(ppm)) - \ln(10^6 - w_{O_2}(ppm)) \quad (2.5)$$

Taking partial differential on both sides of the equation, the following equation is obtained for relative error:

$$\frac{d\dot{m}_{O_2}}{\dot{m}_{O_2}} = \frac{d\dot{m}_{N_2}}{\dot{m}_{N_2}} + \frac{dw_{O_2}(ppm)}{w_{O_2}(ppm)} - \frac{dw_{O_2}(ppm)}{10^6 - w_{O_2}(ppm)} \quad (2.6)$$

To account for the maximum error in all the expressions, all the terms will be added together::

$$\frac{d\dot{m}_{O_2}}{\dot{m}_{O_2}} = \left| \frac{d\dot{m}_{N_2}}{\dot{m}_{N_2}} \right| + \left| \frac{dw_{O_2}(ppm)}{w_{O_2}(ppm)} \right| + \left| -\frac{dw_{O_2}(ppm)}{10^6 - w_{O_2}(ppm)} \right| \quad (2.7)$$

Similarly by using eq. (2.3), the following expression can be obtained:

$$\frac{dw_{O_2}(ppm)}{w_{O_2}(ppm)} = \left| \frac{dA}{A} \right| \quad (2.8)$$

The experimental setup has been designed in such a way that $w_{O_2}(ppm) \ll 10^6$, so that micro-GC does not saturate. Combining eq. (2.3), (2.7) and (2.8), the following expression is obtained for error in oxygen flux estimation:

$$\frac{d\dot{m}_{O_2}}{\dot{m}_{O_2}} = \left| \frac{d\dot{m}_{N_2}}{\dot{m}_{N_2}} \right| + \left| \frac{dA}{A} \right| + \left| -\frac{dA}{c \times 10^6} \right| \quad (2.9)$$

The error in measuring nitrogen mass flow rate (\dot{m}_{N_2}) is associated with mass flow controller. The mass flow controller has a maximum error of 0.8% of reading. The error associated with area count measurements depends on the oxygen fraction in the stream. For high area counts, the error will be less and vice versa. As a results, the error will be higher for diffusion studies compared to convection-diffusion. There is no absolute value given for error in area count measurements in the manufacturer manual for the molecular sieve column. The uncertainty is very small in the area count measurements, which is evident from the size of error-bars in Fig. 2.14. During experimentation, the uncertainty in area count is observed between 1–3% of the reading. The absolute error in area count varied between 1000–9000 ($\simeq 1 - 3\%$ error). For medium sensitivity of micro-GC, the calibration constant (c) is around 30. Using these values, the error in oxygen flux measurements can be found as follows:

$$\frac{d\dot{m}_{O_2}}{\dot{m}_{O_2}} = 0.008 + 0.03 + \frac{9000}{30 \times 10^6} = 0.03818 \simeq 3.82\% \quad (2.10)$$

A repeatability and uncertainty analysis on the mass transport setup is also done. The oxygen flux vs ΔP profile was measured in three different sweeps on the same GDL-MPL assembly (SIGRACET, model: 34 BC). All the experiments were done on the same day to avoid any shift in calibration curve. The three data sets are shown in Fig. 2.15. The pressure difference across porous media is indirectly controlled by

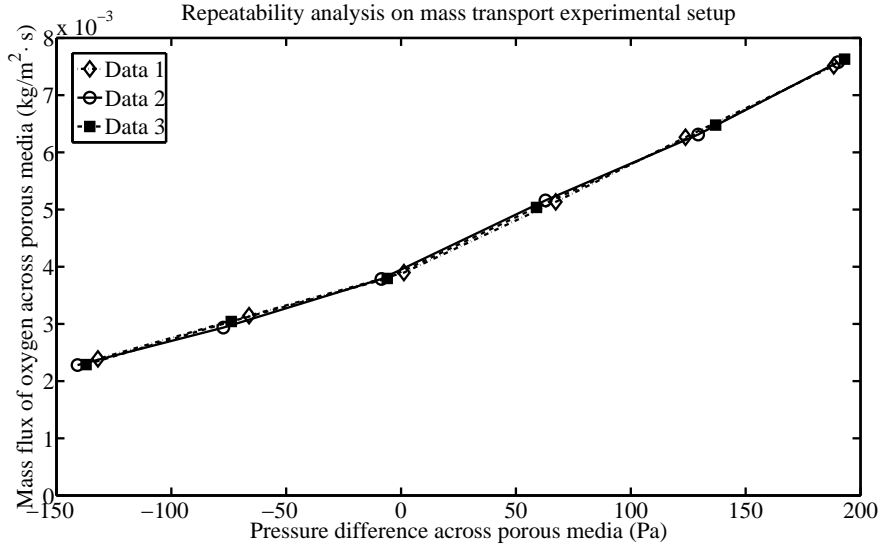


Figure 2.15 – Repeatability analysis results on mass transport experimental setup

the back pressure controllers, hence it is not possible to get exactly same pressure difference in each trial. Due to this reason, the points in different trial are slightly separated horizontally as well. The maximum data uncertainty within trials is found to be around $\pm 2.8\%$, which is within the theoretically calculated range.

2.2 Experimental Setup for Permeability Measurements

In mass transport there are mainly three important transport properties: the diffusivity of the porous media, pore size distribution (Knudsen diffusivity) and the permeability of the porous media. The mass transport setup described in the previous section measures the net mass transport across porous media, accounting for all of the three effects. For the current experimentation, the Knudsen diffusivity is obtained by using the permeability experimentation in transition region between pure viscous and pure Knudsen region [21]. In this section, an experimental method to find the permeability of the porous media is discussed. Having known the Knudsen number and permeability, the diffusivity of the porous media can be easily predicted from mass transport results.

To measure the permeability of the porous media, a modified diffusion bridge chip was used. The schematics of the permeability measurement experimental setup is shown in Fig. 2.16. The inlet of one channel and the outlet of the other channel were

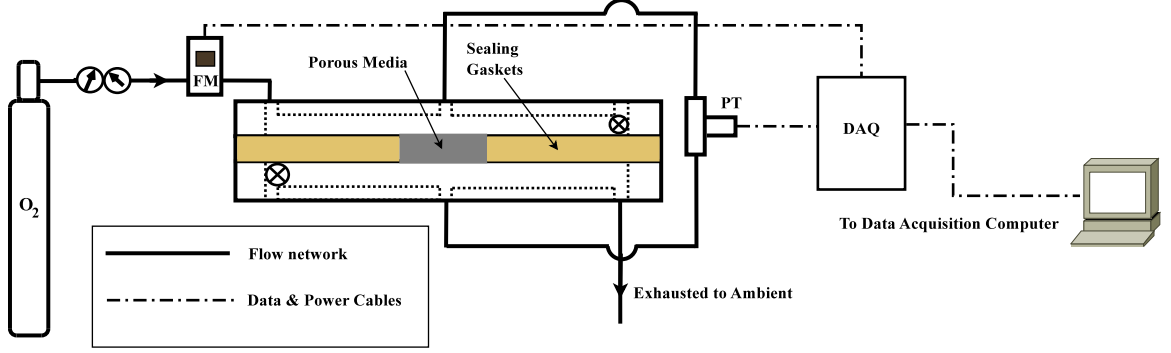


Figure 2.16 – Schematics of the permeability measurement experimental setup

blocked. This forces the flow to go through the porous media. All the control and analysis equipments are the same as used in mass transport setup. Due to the flow across the porous media, a pressure drop occurs. The pressure drop can be measured by the differential pressure transducer. By varying the flow rate across the porous media, the pressure drop can also be varied. From the experiments, a pressure drop vs velocity profile can be obtained for the porous media. This profile can be fitted to Darcy- Forchheimer equation, given as follows [55]:

$$\frac{dp}{dx} = -\frac{\eta}{B_v}v - \frac{\rho}{B_1}v^2 \quad (2.11)$$

where B_v is viscous permeability and B_1 is inertial permeability.

2.2.1 Data Error Analysis for Permeability Measurement

To find the margin of error in permeability measurements, an error analysis on permeability setup is shown in this section. For low velocities across porous media, the Darcy-Forchheimer equation shown in eq. 2.11 reduces to the linear Darcy's equation:

$$\frac{dp}{dx} = -\frac{\eta}{B_v}v \quad (2.12)$$

where v is the pore average velocity across the porous media. The velocity can be obtained from the volumetric flow rate of gas as follows:

$$v = \frac{\dot{Q}}{\pi D^2/4} \quad (2.13)$$

where D is the diameter of mass transport aperture and \dot{Q} is the volumetric flow rate. Assuming a linear pressure gradient, equation (2.12) can be expanded as:

$$B_v = -\frac{\eta L}{\Delta p}v = -\frac{\eta L}{\Delta p} \frac{\dot{Q}}{\pi D^2/4} = \frac{4\eta}{\pi} \frac{L\dot{Q}}{\Delta p D^2} \quad (2.14)$$

where L is the thickness of porous media and Δp is the pressure difference measured by transducer. By doing a similar analysis as shown in section 2.1.8, the maximum relative error in the permeability measurement can be given as follows:

$$\frac{dB_v}{B_v} = \left| \frac{dL}{L} \right| + \left| \frac{d\dot{Q}}{\dot{Q}} \right| + \left| -\frac{d\Delta p}{\Delta p} \right| + \left| -2\frac{dD}{D} \right| \quad (2.15)$$

the thickness L was measured by a micrometer (Mitutoyo, Model: CLM1-.6"QM) with an error of $\pm 2\mu m$, the relative accuracy of the mass flow controller is $\pm 0.8\%$ of the reading and the accuracy of the pressure transducer is $\pm 0.05\%$ of the reading. The diameter of the aperture was measured by a surface profilometer (AMBIOS, model: XP-300). The maximum error in diameter measurement can be assumed to be around $10\mu m$. The thickness of the porous media in experimentation was between $300\text{--}1000\mu m$ and the diameter of the aperture was $2000\mu m$. Putting these values in above equation, the maximum error is given as follows:

$$\frac{dB_v}{B_v} = \left| \frac{2}{300} \right| + |0.008| + |-0.0005| + \left| -2 \times \frac{10}{2000} \right| = 0.02516 \simeq 2.52\% \quad (2.16)$$

To find the repeatability and uncertainty of the experimental data, multiple experiments were done on a GDL-MPL assembly (SIGRACET, model: 34 BC) using oxygen as the working fluid. All the pressure drop vs flow rate data are shown in Fig. 2.17. The maximum margin of error in pressure measurement for a 95% confidence interval is around $\pm 4.5 Pa$, for a mean pressure of $1104.7 Pa$ and a flow rate of $12 ccm$. Due to the negligible margins of error in pressure measurements, they have not been shown in the figure. The maximum difference between permeability values obtained from these data sets is found to be $\pm 1.7\%$, which is within the calculated theoretical range.

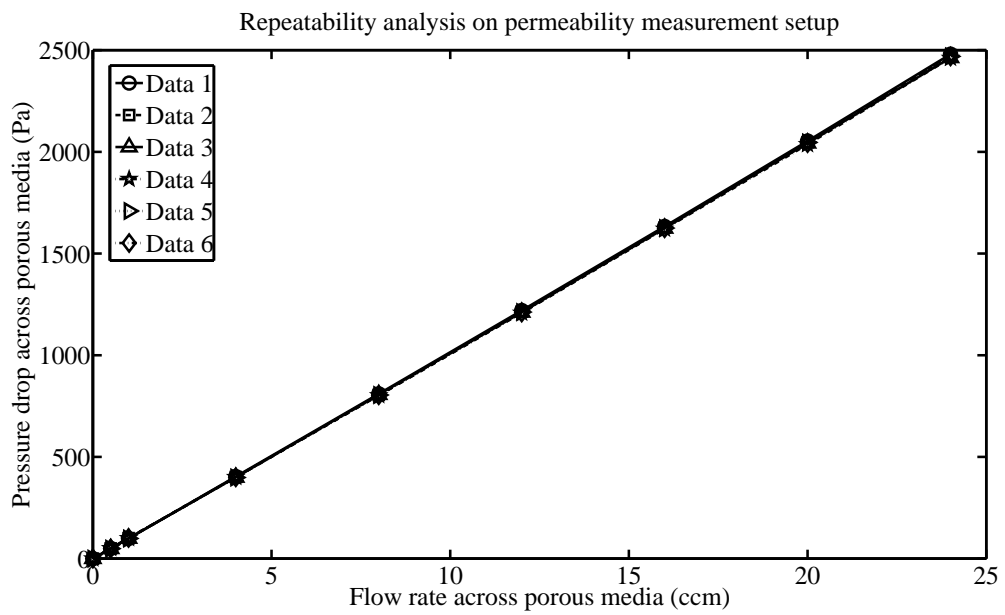


Figure 2.17 – Repeatability analysis results for the permeability measurement setup

Chapter 3

Numerical Modelling of Mass Transfer in Porous Media

This chapter presents the theoretical models used to predict mass transport in the porous transport layers of the fuel cell. The theoretical models are needed for post processing of the experimental data, obtained from the setups described in chapter 2. The experimentation gives only raw profiles like species flux vs pressure difference. This raw data needs to be fitted to the theoretical models for evaluation of various transport properties. The various theoretical models are also helpful in understanding the physics of mass transport and effect of various properties by means of numerical simulation.

The models presented in this chapter are: Ficks and Darcy's model for convection diffusion, dusty gas model (DGM) and binary friction model (BFM). The binary friction model (BFM) has been corrected to account for the assumptions made by Kerkhof [26], and a modified binary friction model (MBFM) is also presented. The various models are then numerically solved using MATLAB's `bvp4c` solver. The numerical models are presented with parametric studies to highlight the differences between them.

The chapter is divided in four sections. Section 3.1 describes the problem and solution parameters, section 3.2 describes various models used to model the mass transport including the new modified binary friction model (MBFM). Section 3.3 presents a few validation cases by comparing the results to data available in literature, as well as the data obtained from other simulations. Finally parametric studies are presented in section 3.4.

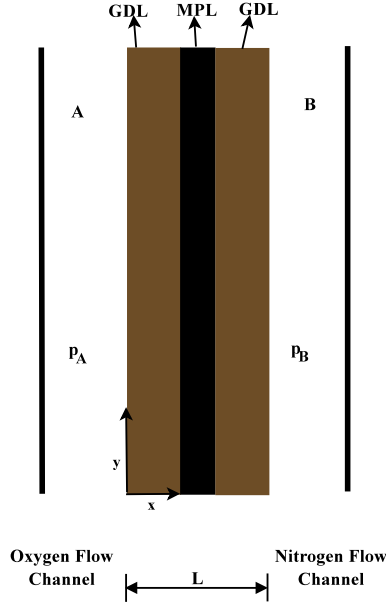


Figure 3.1 – The problem domain used for numerical modelling

3.1 Problem Description

The problem domain under study is shown in Fig. 3.1. The porous media is a sandwich of either GDL only, or a combination of GDL and MPL similar to the one used in experiments. The working fluids, oxygen and nitrogen flow on the two faces of the porous media. The objective of the numerical analysis is to predict the fluxes of different species. The obtained data can be compared to experimental results, to estimate porous media properties and to verify the trends of different models. The validated model can be used to study the pressure profiles and driving forces inside the porous media to understand the physics of mass transport.

The problem domain has been assumed as one-dimensional for simplicity of analysis. The parameters affecting the mass transport are the physical properties of the porous media (i.e. porosity, permeability, thickness, average pore size), and the operating conditions (i.e. temperature, pressure in the flow channels, composition of gases in both channels). The partial pressure of gases in the flow channels is known, as either a pure gas is flowing in the channel or the composition is known. For the gases not flowing in the channel the partial pressure is taken as zero, e.g. in Fig. 3.1 the partial pressure of oxygen in nitrogen flow channel is taken to be zero. Once the problem is defined, its physics has to be modelled according to the mass transport theories.

3.2 Governing Equations

This section describes various theoretical models used for mass transport calculations in porous media. A detailed derivation of each of the models is presented, followed by an analysis of each of the models describing the salient features and shortcomings of each model. The models are presented in the same order, as they were proposed in literature, showing the developments in each one compared to the last model.

3.2.1 Fick's Law

Fick's law has been most commonly used for mass transport calculations in binary mixtures [19]. Fick's law describes the transport of a species in infinitely dilute mixture as a function of its density gradient [19, pp.535, eq.17.7-3]:

$$\mathbf{n}_i^D = -D_{ij}\nabla\rho_i \quad (3.1)$$

where \mathbf{n}_i^D is the mass flux of species i , with respect to a frame of reference moving with average mixture mass velocity. D_{ij} is the binary diffusion coefficient and ρ_i is the density of species i in the mixture. This can also be expressed as:

$$\rho_i(\mathbf{v}_i - \mathbf{v}) = -D_{ij}\nabla\rho_i \quad (3.2)$$

where \mathbf{v} is average mass velocity, which is defined as following [19]:

$$\mathbf{v} = \frac{\sum_{i=1}^n \rho_i \mathbf{v}_i}{\sum_{i=1}^n \rho_i} = \frac{\sum_{i=1}^n \rho_i \mathbf{v}_i}{\rho_t} = \sum_{i=1}^n \omega_i \mathbf{v}_i \quad (3.3)$$

rearranging eq. (3.2), the following equation can be obtained:

$$\mathbf{n}_i = \rho_i \mathbf{v}_i = \rho_i \mathbf{v} - D_{ij}\nabla\rho_i \quad (3.4)$$

where \mathbf{n}_i is the mass flux of species i . In absence of a chemical reaction, a simple mass balance suggests that the flux should remain constant:

$$\nabla \cdot \mathbf{n}_i = 0 \Rightarrow \mathbf{v} \cdot \nabla \rho_i + \rho_i \nabla \cdot \mathbf{v} - D_{ij} \nabla^2 \rho_i = 0 \quad (3.5)$$

the mass average velocity \mathbf{v} is only dependent on pressure difference, and will remain constant across porous media.

Solving the second order boundary value problem for a 1-D case will yield the following expression for density of species i :

$$\rho_i = -k_1 \frac{D_{ij}}{v} + k_2 \exp\left(\frac{v}{D_{ij}}x\right) \quad (3.6)$$

where k_1 and k_2 are integration constants. It is assumed that the partial pressure of species i is p_i^A at $x = 0$ and p_i^B at $x = L$. Putting these boundary conditions back in eq. (3.5), the following equation can be obtained for density profile along x axis:

$$\rho_i = \frac{M_i}{RT} \left[p_i^A - (p_i^A - p_i^B) \left(1 - e^{\frac{v}{D_{ij}}L}\right)^{-1} + (p_i^A - p_i^B) \left(1 - e^{\frac{v}{D_{ij}}L}\right)^{-1} e^{\frac{v}{D_{ij}}x} \right] \quad (3.7)$$

using the ideal gas law $\rho_i = \frac{p_i M_i}{RT}$, the following expression is obtained for the partial pressure profile of species i :

$$p_i = p_i^A - (p_i^A - p_i^B) \left(1 - e^{\frac{v}{D_{ij}}L}\right)^{-1} + (p_i^A - p_i^B) \left(1 - e^{\frac{v}{D_{ij}}L}\right)^{-1} e^{\frac{v}{D_{ij}}x} \quad (3.8)$$

this density profile can be used in eq. (3.4) to find mass flux of species i at any location:

$$n_i|_{x=0} = \frac{M_i}{RT} \left[p_i^A v - (p_i^A - p_i^B) v \left(1 - e^{\frac{v}{D_{ij}}L}\right)^{-1} \right] \quad (3.9)$$

Similarly the molar flux can be given as following:

$$N_i|_{x=0} = \frac{1}{RT} \left[p_i^A v - (p_i^A - p_i^B) v \left(1 - e^{\frac{v}{D_{ij}}L}\right)^{-1} \right] \quad (3.10)$$

It must be noted that till now the porous media has not been mentioned in the derivation anywhere. The velocity v used in the above expressions is the interstitial velocity (pore velocity) and not the average velocity across the porous media. Similarly the flux N_i is interstitial and must be converted to effective flux to obtain the actual flux across porous media. Due to the porous media, only a certain fraction of the actual area is available for the flow to occur. That fraction is the void volume fraction of the porous media, also known as the porosity ϵ . Another factor is the tortuous path the fluid has to take to go across the porous media, compared to a straight path of a pore. This additional hindrance is accounted for by the tortuosity of the porous media, τ . The effective porous media flux is related to the local pore flux by following equation [26]:

$$\mathbf{N}_i^{eff} = \frac{\epsilon}{\tau} \mathbf{N}_i \Rightarrow \mathbf{N}_i = \mathbf{N}_i^{eff} \frac{\tau}{\epsilon} \quad (3.11)$$

Similarly the average velocity across porous media ($\bar{\mathbf{v}}$) is related to the pore velocity as follows:

$$\bar{\mathbf{v}} = \frac{\epsilon}{\tau} \mathbf{v} \Rightarrow \mathbf{v} = \bar{\mathbf{v}} \frac{\tau}{\epsilon} \quad (3.12)$$

Also, the effective diffusivity of a porous media is given as:

$$D_{ij}^{eff} = \frac{\epsilon}{\tau} D_{ij} \quad (3.13)$$

Putting these expressions back in eq. (3.8) and eq. (3.10), the following expressions are obtained for the pressure profile and flux in porous media:

$$p_i = p_i^A - (p_i^A - p_i^B) \left(1 - e^{-\frac{\bar{v}}{D_{ij}^{eff}}L}\right)^{-1} + (p_i^A - p_i^B) \left(1 - e^{-\frac{\bar{v}}{D_{ij}^{eff}}L}\right)^{-1} e^{-\frac{\bar{v}}{D_{ij}^{eff}}x} \quad (3.14)$$

$$N_i^{eff}|_{x=0} = \frac{1}{RT} \left[p_i^A \bar{v} - (p_i^A - p_i^B) \bar{v} \left(1 - e^{-\frac{\bar{v}}{D_{ij}^{eff}}L}\right)^{-1} \right] \quad (3.15)$$

The mass average velocity across the porous media is given by Darcy's law:

$$\bar{\mathbf{v}} = -\frac{B_v}{\eta} \nabla p \quad (3.16)$$

where B_v is the permeability of the porous media and η is the mixture viscosity.

The Fick's law is very simple in understanding and easy in implementation, but it can be used for a few cases only. As this law works only for binary mixtures or infinitely dilute solutions, it is not useful for multicomponent mixtures. Also, the Knudsen effects are not accounted, which can be quite significant for small pore radius e.g. in MPLs and CLs.

3.2.2 Dusty Gas Model

The dusty gas model (DGM) has been proposed by Mason and Malinauskas [17] for multicomponent mass transport in porous media. In the development of their theory, Mason and Malinauskas [17] have assumed the molecular and Knudsen diffusion fluxes in series, which are then parallel to viscous and surface fluxes as shown in Fig. 3.2. During the development of the theory the species gradients are related to Maxwell-Stefan term as follows [17, pp. 37]:

$$-\mathbf{d}_i = \sum_{j=1}^n \frac{x_j \mathbf{N}_i^D - x_i \mathbf{N}_j^D}{n \mathcal{D}_{ij}} \quad (3.17)$$

where \mathbf{d}_i is the gradient term and \mathbf{N}_i^D is the diffusive flux. It can be seen that the flux term consists of only diffusive fluxes in the DGM treatment. Next, the porous media is brought into the equations by considering it as a collection of dust molecules fixed in space. The dust molecules are added to the force balance as the $n + 1^{th}$ species.

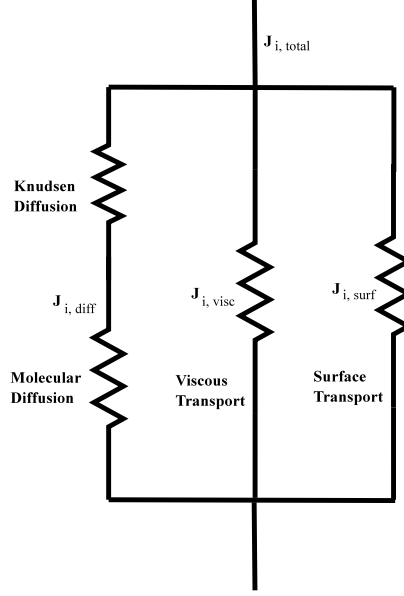


Figure 3.2 – Flow circuit diagram proposed for DGM by Mason and Malinauskas [17]

Now the dust molecule terms are taken out of the Maxwell-Stefan term and the dust flux is assumed to be zero ($\mathbf{N}_d^D = 0$). This is a wrong assumption, which is explained in detail at a later stage in this section. With the assumption, the following equation is obtained [17, pp. 45]:

$$\begin{aligned}
& \frac{n_i}{n} \sum_{j=1}^n \frac{n_j (1 - \Delta'_{id})}{n [D_{ij}]_i} \left[\frac{\mathbf{N}_i^D}{n_i} - \frac{\mathbf{N}_j^D}{n_j} \right] + \frac{1 - \Delta'_{id}}{n [D_{iK}]_1} \mathbf{N}_i^D \\
& = -\nabla \left(\frac{n_i}{n} \right) - \left(\frac{n_i}{n} \right) \nabla \ln p + \frac{n_i}{p} \mathbf{F}_i - \frac{n_i}{n} \left[\sum_{j=1}^n \frac{n_j}{n'} (\alpha'_{ij})_{tr} + \frac{n_d}{n} (\alpha'_{id})_{tr} \right] \nabla \ln T
\end{aligned} \tag{3.18}$$

where n_i, n_j and n_d are number of moles of species i, j and dust respectively, and n represents total number of moles. D_{iK} is the species wall interaction parameter, which has been assumed to be equal to Knudsen diffusion coefficient. The expression $(1 - \Delta'_{id})$ is the second order correction of diffusion coefficients. In the absence of external forces, and for an isothermal ideal gas, eq. (3.18) can be simplified to the following expression [26]:

$$\frac{1}{p_t} \nabla_T p_i = \sum_{j=1}^n \frac{x_i \mathbf{N}_j^D - x_j \mathbf{N}_i^D}{c_t D'_{ij}} - \frac{c_d \mathbf{N}_i^D}{c_t^2 D'_{id}} = \sum_{j=1}^n \frac{x_i \mathbf{N}_j^D - x_j \mathbf{N}_i^D}{c_t D'_{ij}} - \frac{\mathbf{N}_i^D}{c_t D'_{im}} \tag{3.19}$$

where c_d is the concentration of dust molecules. The parameters D'_{ij} and D'_{im} are the molecular and Knudsen diffusion coefficients with second order corrections given

by Mason and Malinauskas [17]. The assumption in the derivation of the DGM is that the net flux can be split up into diffusive and viscous flux as follows:

$$\mathbf{N}_i = \mathbf{N}_i^D + x_i \mathbf{N}_{visc} \quad (3.20)$$

Replacing \mathbf{N}_i^D in eq. (3.19) by the above expression, the following equation is obtained for the force balance:

$$\frac{1}{p_t} \nabla_T p_i = \sum_{j=1}^n \frac{x_i \mathbf{N}_j - x_j \mathbf{N}_i}{c_t D'_{ij}} - \frac{\mathbf{N}_i}{c_t D'_{im}} + \frac{x_i \mathbf{N}_{visc}}{c_t D'_{im}} \quad (3.21)$$

where \mathbf{N}_{visc} is given by Darcy's law in porous media. The second order corrections in the diffusion coefficients are negligible so D' can be replaced by D [17]. Taking into account the above-mentioned simplifications, and using effective properties for porous media, the final DGM equation is as follows:

$$\frac{1}{p_t} \nabla_T p_i = \sum_{j=1}^n \frac{x_i \mathbf{N}_j^{eff} - x_j \mathbf{N}_i^{eff}}{c_t D_{ij}^{eff}} - \frac{\mathbf{N}_i^{eff}}{c_t D_i^{Keff}} + \frac{x_i \mathbf{N}_{visc}^{eff}}{c_t D_i^{Keff}} \quad (3.22)$$

The DGM has been recently questioned by Kerkhof [26] for some inherent inconsistencies in the derivation. While trying to solve the Stefan tube problem, the DGM is shown to give non-intuitive results. To solve the equations of mass transport in Stefan tube, it is assumed that the air is stagnant inside tube. However, while solving the flow equations, the air was found to be circulating. Kerkhof [26] pointed that the fluxes in the force balance already contained the viscous part and thus accounting for them again is incorrect. The double accounting statement by Kerkhof [26] is not very clear and concise, and thus the errors in the derivation of DGM have been explained in detail here. The main error in the derivation is while summing all the Maxwell-Stefan forces including the ones by dust molecules in eq. (3.17). The sum of the Maxwell-Stefan terms can be shown as follows:

$$\sum_{j=1}^{n+1} \frac{x_i \mathbf{N}_j^D - x_j \mathbf{N}_i^D}{c_t D'_{ij}} = \sum_{j=1}^n \frac{x_i \mathbf{N}_j^D - x_j \mathbf{N}_i^D}{c_t D'_{ij}} + \frac{x_i \mathbf{N}_d^D}{c_t D'_{id}} - \frac{x_d \mathbf{N}_i^D}{c_t D'_{id}} \quad (3.23)$$

where \mathbf{N}_d^D is the diffusive flux of dust, which is assumed to be zero in the DGM derivation. However, for a stationary frame of reference it can be said that the net flux of dust molecules will be zero (i.e. $\mathbf{N}_d = 0$), as they are fixed. If the flux splitting analogy is used, the following relation is obtained between diffusive and net flux of dust:

$$\mathbf{N}_d = \mathbf{N}_d^D + x_d \mathbf{N}_{visc} \quad (3.24)$$

Due to the fixed dust molecules, \mathbf{N}_d will be zero. The viscous flux N_{visc} will have a finite values for a pressure gradient. Therefore, N_d^D can not be zero at the same time, as it would imply $x_d = 0$, which in turn indicates a zero membrane friction. Due to these errors in derivation, the DGM equations are not self consistent. This can be shown by summing all the equations over all the components, and obtaining an expression for net pressure gradient. For a set of correct equations, the summation should give the Darcy's equation for net pressure gradient. However in this case a different equation is obtained, which is neither similar nor can be converted to Darcy's equation. Kerkhof [26] have also observed similar discrepancies in the DGM, and have proposed a new mass transport model for multicomponent mixture.

3.2.3 Binary Friction Model

The binary friction model (BFM) is a modified mass transfer model given by Kerkhof [26] for transport through membranes and porous media. The binary friction model is based on Lightfoot equation, which is obtained from irreversible thermodynamic considerations of the system. In irreversible thermodynamics, the power dissipation in the system is given as follows [26]:

$$T\sigma = - \sum_{i=1}^n \left(\frac{1}{M_i} \nabla_T \mu_i - \mathbf{F}_i \right) \cdot \mathbf{J}_i \quad (3.25)$$

where σ is the rate of entropy generation per unit volume and \mathbf{J}_i is the mass averaged flux w.r.t. mass average velocity.

$$\mathbf{J}_i = \rho_i (\mathbf{v}_i - \mathbf{v}) \quad (3.26)$$

In the treatment of Lightfoot, a zero vector is added to equation (3.25) [26]:

$$\frac{1}{\rho_t} \nabla p - \sum_{i=1}^n \omega_i \mathbf{F}_i = \mathbf{0} \quad (3.27)$$

The new equation of entropy generation is given by the following equation:

$$T\sigma = - \sum_{i=1}^n \left(\frac{1}{M_i} \nabla_{T,p} \mu_i + \frac{\bar{V}_i}{M_i} \nabla p - \frac{1}{\rho_t} \nabla p - \mathbf{F}_i + \sum_{j=1}^n \omega_j \mathbf{F}_j \right) \cdot \mathbf{J}_i \quad (3.28)$$

If the entropy generation is defined in terms of a driving force term as follows:

$$\sigma = -c_t R \sum_{i=1}^n \mathbf{d}_i \cdot (\mathbf{v}_i - \mathbf{v}) \quad (3.29)$$

then by comparing eq. (3.28) and eq. (3.29), the driving force per unit volume can be found out as follows:

$$c_t RT \mathbf{d}_i = c_i \nabla_{T,p} \mu_i + (c_i V_i - \omega_i) \nabla p - \rho_i \left(\mathbf{F}_i - \sum_{j=1}^n \omega_j \mathbf{F}_j \right) \quad (3.30)$$

If the system is in equilibrium, the driving forces will be equal to the friction forces given as follows:

$$c_t RT \mathbf{d}_i = -c_t RT \sum_{j=1}^n \beta_{ij} (\mathbf{v}_i - \mathbf{v}_j) \quad (3.31)$$

where the interaction parameter β_{ij} can be found from statistical arguments as follows [15, chapter 2]:

$$\beta_{ij} = \frac{x_i x_j}{D_{ij}} \quad (3.32)$$

Equating equation (3.30) and equation (3.31) leads to the following familiar equation:

$$\frac{x_i}{RT} \nabla_{T,p} \mu_i + \frac{(\phi_i - \omega_i)}{c_t RT} \nabla p - \frac{\rho_i}{c_t RT} \left(\mathbf{F}_i - \sum_{j=1}^n \omega_j \mathbf{F}_j \right) = \sum_{j=1}^n \frac{x_i \mathbf{N}_j - x_j \mathbf{N}_i}{c_t D_{ij}} \quad (3.33)$$

Now the porous media is brought in the equation as $n + 1^{th}$ component. While summing the interspecies interactions, the porous media velocity is taken as zero and the porous media friction term is taken out of the rest of summation. The zero vector presented in eq. (3.27) is also eliminated from the equation. The final Lightfoot equation is given as follows [26]:

$$\frac{x_i}{RT} \nabla_{T,p} \mu_i + \frac{\phi_i}{c_t RT} \nabla p - \frac{\rho_i}{c_t RT} \mathbf{F}_i = \sum_{j=1}^n \frac{x_i \mathbf{N}_j - x_j \mathbf{N}_i}{c_t D_{ij}} - r_{im} \mathbf{N}_i \quad (3.34)$$

Where the porous media friction parameter r_{im} is given as:

$$r_{im} = \frac{x_m}{c_t D_{im}} = \frac{\beta_{im}}{c_i} \quad (3.35)$$

One interesting point to notice in the final Lightfoot equation is that it is based on pore averaged fluxes, even though the equation is derived for local pore fluxes. The inherent assumption that one can be switched to another is not self evident. Also the addition of the zero vector in the primary stage of derivation of the Lightfoot equation is not clear, as it does not yield any changes in the final equation. Similar observations have also been made in the review by Kerkhof [26].

The binary friction model proposed by Kerkhof [26] for isothermal gases is developed from the Lightfoot equation given by equation (3.34). The external forces

are assumed to be absent and the gases are considered to be ideal. Under these assumptions, the following statements can be concluded:

$$\mathbf{F}_i = 0 \quad (3.36)$$

$$c_i = x_i \frac{p_t}{RT} \quad (3.37)$$

$$\phi_i = c_i \bar{V}_i = x_i \quad (3.38)$$

$$c_t = \frac{p_t}{RT} \quad (3.39)$$

$$\frac{x_i}{RT} \nabla_{T,p} \mu_i = \frac{x_i}{RT} RT \nabla (\ln x_i) = \nabla x_i \quad (3.40)$$

The fluxes are assumed to be per unit area of pore along the pore path. The equation (3.34) can be rewritten as [26]:

$$\nabla x_i + \frac{x_i}{p_t} \nabla p_t \equiv \frac{1}{p_t} \nabla p_i \equiv RT \sum_{j=1}^n \frac{(x_i \mathbf{N}_j - x_j \mathbf{N}_i)}{p_t D_{ij}} - r_{im} \mathbf{N}_i \quad (3.41)$$

Summing up over all the components, the interspecies friction term cancels out and the following equation is obtained for the mixture. A new friction parameter β_{im} is also defined:

$$\frac{1}{p_t} \nabla p_t = - \sum_{i=1}^n r_{im} \mathbf{N}_i \equiv - \sum_{i=1}^n \beta_{im} \mathbf{V}_i \quad (3.42)$$

To determine the porous media friction parameter, Kerkhof [26] has considered two cases. In the first case, Knudsen flow of a mixture is considered. In the Knudsen region, interspecies interaction is neglected and eq. (3.41) can be rewritten as follows to describe the flow:

$$\frac{1}{p_t} \nabla p_i = - \frac{RT \mathbf{N}_i}{D_i^K p_t} \quad (3.43)$$

which gives:

$$\beta_{im}^K = \frac{x_i}{D_i^K} \quad (3.44)$$

where D_i^K is the Knudsen diffusion coefficient of species i given as follows [56]:

$$\begin{aligned} D_i^K &= 0.89 D_{i0}^K \\ D_{i0}^K &= \frac{2}{3} r_p \left(\frac{8RT}{\pi M_i} \right)^{1/2} \end{aligned} \quad (3.45)$$

where r_p is the pore radius and M_i is molecular weight of species i .

In the continuum region, it is assumed that for all the components, the local and pore averaged velocities are equal and the flow is purely viscous. The flow is described by Darcy's equation [26]:

$$\frac{1}{p_t} \nabla p_t = - \frac{RT}{p_t^2} \frac{\eta}{B_0} \mathbf{N}_t \quad (3.46)$$

where B_0 is permeability of the pore, and not of the porous media. The above equation does not represent the exact form of Darcy's equation as per the definitions of mass averaged velocities [19]. The detailed description is given in next section. Comparing eq. (3.46) & eq. (3.42) and assuming $\mathbf{v}_i \simeq \mathbf{v}$, the following expression is obtained:

$$\frac{1}{p_t} \nabla p_t = - \sum_{i=1}^n \beta_{im}^v \mathbf{v}_i = -\mathbf{v} \sum_{i=1}^n \beta_{im}^v = -\frac{RT}{p_t} \sum_{i=1}^n \beta_{im}^v \mathbf{N}_t \quad (3.47)$$

Kerkhof [26] suggested that, the interaction parameter β_{im}^v can be written in terms of geometry dependent part and component dependent part as follows:

$$\beta_{im}^v = \frac{1}{B_0} \kappa_i \phi_i = \frac{1}{B_0} \kappa_i x_i \quad (\text{In this case}) \quad (3.48)$$

Comparing this with equation (3.46), the following equation is obtained :

$$\sum_{i=1}^n \kappa_i x_i = \frac{\eta}{p_t} \quad (3.49)$$

where the mixture viscosity η is given by Chapman-Enskog theory [28]:

$$\eta = \sum_{i=1}^n \frac{x_i \eta_i^0}{\sum_{j=1}^n x_j \xi_{ij}} \quad (3.50)$$

So the partial viscosity κ_i can be given as follows:

$$\kappa_i = \frac{1}{p_t} \frac{\eta_i^0}{\sum_{j=1}^n x_j \xi_{ij}} \quad (3.51)$$

Finally it is assumed that the two frictions (i.e. wall friction and viscous friction) work in parallel and thus the flow resistances can be added in parallel.

$$\frac{1}{\beta_{im}} = \frac{1}{\beta_{im}^K} + \frac{1}{\beta_{im}^v} = \frac{D_i^K}{x_i} + \frac{B_0}{\kappa_i x_i} \quad (3.52)$$

A new parameter f_{im} is defined for convenience as follows:

$$f_{im} = \frac{\beta_{im}}{x_i} = \left(D_i^K + \frac{B_0}{\kappa_i} \right)^{-1} \quad (3.53)$$

The final binary friction model is presented as follows [26]:

$$\frac{1}{p_t} \nabla_T p_i = RT \sum_{j=1}^n \Phi_{ij} \frac{(x_i \mathbf{N}_j - x_j \mathbf{N}_i)}{p_t D_{ij}} - f_{im} \frac{RT}{p_t} \mathbf{N}_i \quad (3.54)$$

where the parameter Φ_{ij} is defined as zero in Knudsen region and as unity in fully normal region. For porous media, the equation is modified to account for porosity and tortuosity of porous media. Using eq. (3.11) to replace \mathbf{N} in the above equation, the following expression is obtained for effective flux

$$\nabla_T p_i = \frac{\tau}{\epsilon} RT \left[\sum_{j=1}^n \Phi_{ij} \frac{(x_i \mathbf{N}_j^{eff} - x_j \mathbf{N}_i^{eff})}{D_{ij}} - f_{im} \mathbf{N}_i^{eff} \right] \quad (3.55)$$

The permeability B_0 in the friction parameter f_{im} is the permeability of pore, which is difficult to measure. However the permeability of porous media can be measured and can be related to the permeability of the pore. The pore averaged velocity through a porous media is given by Darcy's equation as follows:

$$\bar{\mathbf{v}} = -\frac{B_v}{\eta} \nabla p \quad (3.56)$$

where B_v is permeability of porous media. The pore averaged velocity is related to the local pore velocity by eq. (3.12) as follows:

$$\bar{\mathbf{v}} = -\frac{B_v}{\eta} \nabla p = \frac{\epsilon}{\tau} \mathbf{v} = -\frac{\epsilon B_0}{\tau \eta} \nabla p \quad (3.57)$$

which gives the following relation between the permeability of pore and porous media:

$$B_v = \frac{\epsilon}{\tau} B_0 \quad (3.58)$$

Using these relations for effective properties, the final BFM equation for a porous media can be written as follows:

$$\nabla_T p_i = RT \left[\sum_{j=1}^n \Phi_{ij} \frac{(x_i \mathbf{N}_j^{eff} - x_j \mathbf{N}_i^{eff})}{D_{ij}^{eff}} - f_{im}^{eff} \mathbf{N}_i^{eff} \right] \quad (3.59)$$

where the effective friction parameter f_{im}^{eff} is given as:

$$f_{im}^{eff} = \left(D_i^{K^{eff}} + \frac{B_v}{\kappa_i} \right)^{-1} \quad (3.60)$$

In the BFM, while evaluating the friction factor, the viscous parameter is obtained with an inherent assumption of the pore average velocity being equal to local velocity in eq. (3.47). Also all the components velocities are assumed to be equal. At very high mixture velocities this assumption can be considered to be valid. However when the mixture velocities and the component velocities are of same order of magnitude the assumption will lead to erroneous results. The parameters obtained with this assumption are incorporated in the main equation where there is no such assumption.

Also it should be noted that the solution of BFM will give different velocities for different species, which is incoherent with the assumption made to derive the very same equation. Another problem in the derivation lies in eq. (3.46). The expression in the equation can only be obtained, under the assumption of mass average velocity being equal to molar average velocity.

3.2.4 Modified Binary Friction Model

Due to the inherent inconsistencies in the assumptions of BFM, a new approach to determine the friction parameters have been presented, which is in line with the approach of Kerkhof [26]. The starting point for the new approach is again the Lightfoot equation under the assumption of ideal gas and zero external forces. The equation is given as follows:

$$\frac{1}{p_t} \nabla p_i = RT \sum_{j=1}^n \frac{(x_i \mathbf{N}_j - x_j \mathbf{N}_i)}{p_t D_{ij}} - r_{im} \mathbf{N}_i \quad (3.61)$$

where the fluxes are per unit area of pore along the pore path. Again summing eq. (3.61) over all the components, the interspecies interaction term will cancel out and the following equation is obtained:

$$\frac{1}{p_t} \nabla p_t = - \sum_{i=1}^n r_{im} \mathbf{N}_i \quad (3.62)$$

For obtaining the friction parameter in the Knudsen region, the interspecies interaction is neglected, and eq. (3.61) is compared with Knudsen diffusion equation in the pore, given as follows:

$$\frac{1}{p_t} \nabla p_i = - \frac{RT}{D_i^K} \frac{1}{p_t} \mathbf{N}_i \quad (3.63)$$

From the above equation, the Knudsen friction parameter can be given as follows:

$$r_{im}^K = \frac{RT}{D_i^K} \frac{1}{p_t} \quad (3.64)$$

For the normal region, it is assumed that the flow can be approximated as a pure viscous flow and can be given by Darcy's law:

$$\mathbf{v} = - \frac{B_0}{\eta} \nabla p_t \quad (3.65)$$

where \mathbf{v} is the mixture mass averaged velocity along the pores and η is mixture viscosity. Here it is worth mentioning that the above equation describes viscous flow in a pore and not in a porous media. Thus the permeability B_v is the pore permeability

and not the permeability of the porous media. In the approach of Kerkhof [26], the above equation is rearranged as shown in following equations:

$$\nabla p_t = -\frac{\eta}{B_0} \mathbf{v} \quad \Rightarrow \quad \frac{1}{p_t} \nabla p_t = -\frac{1}{p_t} \frac{\eta}{B_0} \mathbf{v} \quad (3.66)$$

$$\frac{1}{p_t} \nabla p_t = -\frac{1}{p_t} \frac{\eta}{B_0} c_t \mathbf{v} \frac{1}{c_t} \quad \Rightarrow \quad \frac{1}{p_t} \nabla p_t = -\frac{RT}{p_t^2} \frac{\eta}{B_0} c_t \mathbf{v} \quad (3.67)$$

Kerkhof [26] defines $c_t \mathbf{v}$ as the molar flux of the mixture \mathbf{N}_t , which is inconsistent with the basic definition of fluxes[19]. As the velocity \mathbf{v} in Darcy's law is a mass averaged velocity, the corresponding flux has to be a mass flux. To remove this discrepancy and also to remove the pore averaged velocity assumption, the velocity is defined as mass averaged velocity in current model:

$$\mathbf{v} = -\frac{B_0}{\eta} \nabla p_t \quad \Rightarrow \quad \frac{1}{p_t} \nabla p_t = -\frac{1}{p_t} \frac{\eta}{B_0} \mathbf{v} \quad (3.68)$$

$$\frac{1}{p_t} \nabla p_t = -\frac{1}{p_t} \frac{\eta}{B_0} \sum_{i=1}^n \frac{\rho_i \mathbf{v}_i}{\rho_t} \quad \Rightarrow \quad \frac{1}{p_t} \nabla p_t = -\frac{1}{p_t} \frac{\eta}{B_0} \sum_{i=1}^n \frac{1}{\rho_t} \frac{\rho_i}{c_i} c_i \mathbf{v}_i \quad (3.69)$$

$$\Rightarrow \frac{1}{p_t} \nabla p_t = -\sum_{i=1}^n \frac{1}{p_t} \frac{\eta}{B_0} \frac{M_i}{\rho_t} \mathbf{N}_i \quad (3.70)$$

Comparing the above expression with eq. (3.62), the following expression is obtained for friction parameter in viscous region:

$$r_{im}^v = \frac{\eta}{B_0} \frac{1}{p_t} \frac{M_i}{\rho_t} \quad (3.71)$$

where the mixture viscosity η can be given by Chapman-Enskog theory as follows [28]:

$$\eta = \sum_{j=1}^n \frac{x_j \eta_j^0}{\sum_{k=1}^n x_k \xi_{jk}} \quad (3.72)$$

Putting this back in eq. (3.71), the following expression is obtained for viscous friction parameter:

$$r_{im}^v = \frac{M_i}{B_0} \left[\sum_{j=1}^n \frac{x_j \eta_j^0}{\sum_{k=1}^n x_k \xi_{jk}} \right] \left[\frac{1}{p_t} \frac{RT}{\sum_{j=1}^n p_j M_j} \right] \quad (3.73)$$

For convenience, a new parameter χ_i is defined as follows:

$$\chi_i = M_i \left[\sum_{j=1}^n \frac{x_j \eta_j^0}{\sum_{k=1}^n x_k \xi_{jk}} \right] \left[\frac{1}{\sum_{j=1}^n p_j M_j} \right] \quad (3.74)$$

The viscous friction parameter can be presented as:

$$r_{im}^v = \frac{1}{B_0} \frac{RT}{p_t} \chi_i \quad (3.75)$$

Now assuming that the Knudsen and viscous friction act in parallel, the net friction parameter can be calculated as follows:

$$\begin{aligned} \frac{1}{r_{im}} &= \frac{1}{r_{im}^K} + \frac{1}{r_{im}^v} = D_i^K \frac{p_t}{RT} + \frac{B_0}{\chi_i} \frac{p_t}{RT} \\ \Rightarrow r_{im} &= \frac{RT}{p_t} \left(D_i^K + \frac{B_0}{\chi_i} \right)^{-1} \end{aligned} \quad (3.76)$$

So the final modified binary friction model (MBFM) can be given as follows:

$$\nabla_T p_i = RT \sum_{j=1}^n \left(\frac{p_i \mathbf{N}_j - p_j \mathbf{N}_i}{p_t D_{ij}} \right) - RT \left(D_i^K + \frac{B_0}{\chi_i} \right)^{-1} \mathbf{N}_i \quad (3.77)$$

whereas the original BFM is given as follows:

$$\nabla_T p_i = RT \sum_{j=1}^n \left(\frac{p_i \mathbf{N}_j - p_j \mathbf{N}_i}{p_t D_{ij}} \right) - RT \left(D_i^K + \frac{B_0}{\kappa_i} \right)^{-1} \mathbf{N}_i \quad (3.78)$$

Looking at eq. (3.77) and eq. (3.78), it can be seen that the only difference between the BFM and the MBFM is in the viscous friction term. The parameters κ_i and χ_i are functions of mole fraction for a given mixture. Figures 3.3 and 3.4 show the difference between κ_i (used in BFM) and χ_i (used in the MBFM) for a binary mixture of O_2 and N_2 at total pressure of 107 kPa. It can be seen that only in case of pure mixture the two parameters are the same, and at low mole fractions, the parameters differ from each other. As the difference between the molecular weights of gases in binary mixture increases, the difference between χ_i and κ_i increases as well.

For using the MBFM in porous media, it can be modified in a way similar to the BFM. After adjusting for the effective properties and effective fluxes, the following equation is obtained as MBFM for porous media:

$$\nabla_T p_i = RT \sum_{j=1}^n \left(\frac{p_i \mathbf{N}_j^{eff} - p_j \mathbf{N}_i^{eff}}{p_t D_{ij}^{eff}} \right) - RT \left(D_i^{K^{eff}} + \frac{B_v}{\chi_i} \right)^{-1} \mathbf{N}_i^{eff} \quad (3.79)$$

The modified binary friction model (MBFM) makes only three assumptions: isothermal environment, ideal gas behaviour and no external forces. These assumptions can be practically achieved in any experiment and thus the MBFM can be considered a realistic model. As shown in upcoming sections, even though the change of friction coefficient does not change the results significantly compared to BFM, the merit of MBFM lies in its better accounting of physics.

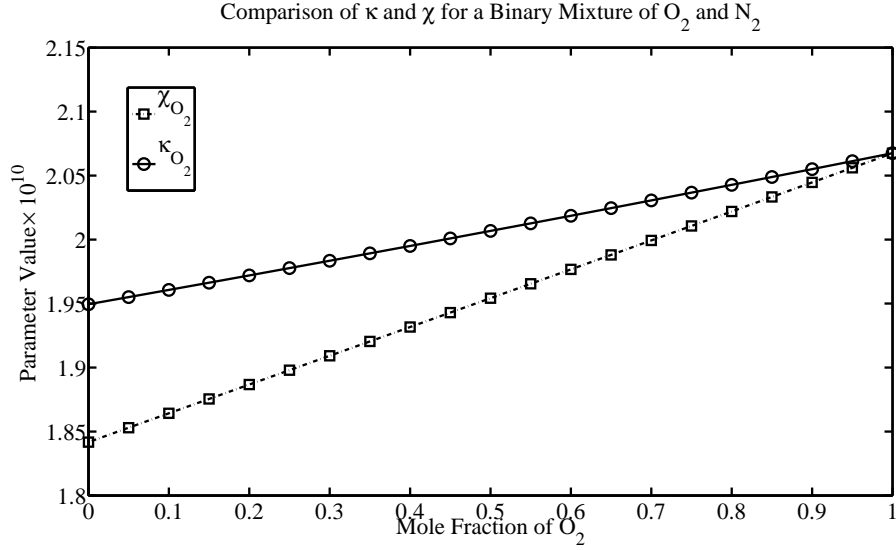


Figure 3.3 – The comparison of O_2 viscous friction parameter used in BFM and MBFM in a $O_2 - N_2$ binary mixture

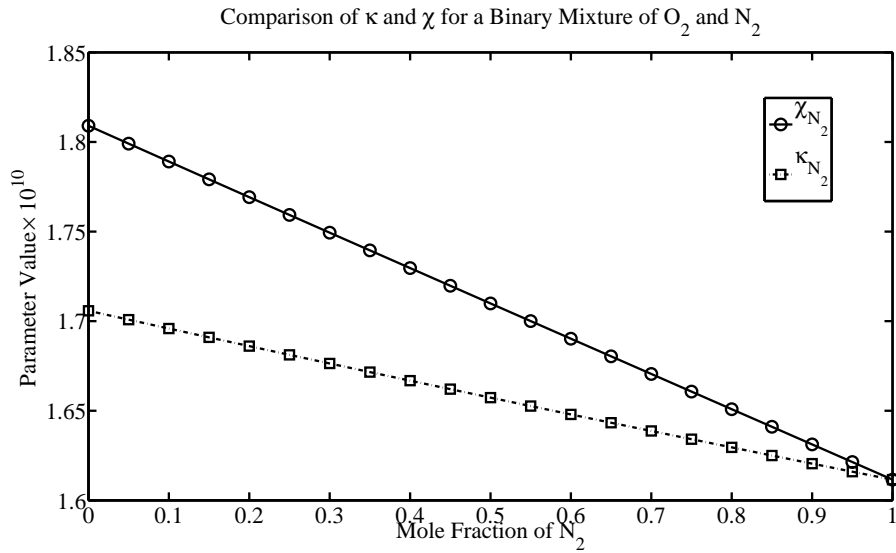


Figure 3.4 – The comparison of N_2 viscous friction parameter used in BFM and MBFM in a $O_2 - N_2$ binary mixture

3.2.5 Numerical Modelling

The models presented in the previous sections have to be solved for one-dimensional case in porous media. However, the equations are quite complex from the point of view of mathematics, and an exact solution might not be achieved for the system of equations. To solve the system of differential equations, numerical methods have been employed. For a binary mixture of O_2 and N_2 four variables must be determined:

fluxes of O_2 and N_2 , and partial pressures of O_2 and N_2 , which are referred in the equations as N_{O_2} , N_{N_2} , p_{O_2} and p_{N_2} . To solve for these four variables, four independent equations are needed. The first two equations for the system are obtained using mass conservation for the species:

$$\nabla \cdot N_{O_2}^{eff} = 0 \quad (3.80)$$

$$\nabla \cdot N_{N_2}^{eff} = 0 \quad (3.81)$$

The other two equations are the momentum balance for the species, which are given as follows for different models:

- **Fick's and Darcy's Equation :**

$$\nabla p_{O_2} = \frac{p_{O_2} \bar{v} - \frac{N_{O_2}^{eff}}{RT}}{D_{O_2 N_2}^{eff}} \quad (3.82)$$

$$\nabla p_{N_2} = \frac{p_{N_2} \bar{v} - \frac{N_{N_2}^{eff}}{RT}}{D_{O_2 N_2}^{eff}} \quad (3.83)$$

where the velocity \bar{v} is given by Darcy's law:

$$\bar{v} = -\frac{B_v}{\eta} \nabla p_t \quad (3.84)$$

- **DGM:**

$$\nabla p_{O_2} = RT \left[\frac{p_{O_2} N_{N_2}^{eff} - p_{N_2} N_{O_2}^{eff}}{p_t D_{O_2 N_2}^{eff}} - \frac{N_{O_2}^{eff}}{D_{O_2 K}^{eff}} + \frac{x_{O_2} N_{visc}}{D_{O_2 K}^{eff}} \right] \quad (3.85)$$

$$\nabla p_{N_2} = RT \left[\frac{p_{N_2} N_{O_2}^{eff} - p_{O_2} N_{N_2}^{eff}}{p_t D_{O_2 N_2}^{eff}} - \frac{N_{N_2}^{eff}}{D_{N_2 K}^{eff}} + \frac{x_{N_2} N_{visc}}{D_{N_2 K}^{eff}} \right] \quad (3.86)$$

where N_{visc} is given as follows:

$$N_{visc} = -\frac{c_t B_v}{\eta} \nabla p_t = -\frac{c_t B_v}{\eta} (\nabla p_{O_2} + \nabla p_{N_2}) \quad (3.87)$$

The mixture viscosity η is given by Chapman-Enskog relation.

- **BFM**

$$\nabla p_{O_2} = RT \left[\frac{(p_{O_2} N_{N_2}^{eff} - p_{N_2} N_{O_2}^{eff})}{p_t D_{O_2 N_2}^{eff}} - \left(D_{O_2}^{Keff} + \frac{B_v}{\kappa_{O_2}} \right)^{-1} N_{O_2}^{eff} \right] \quad (3.88)$$

$$\nabla p_{N_2} = RT \left[\frac{(p_{N_2} N_{O_2}^{eff} - p_{O_2} N_{N_2}^{eff})}{p_t D_{O_2 N_2}^{eff}} - \left(D_{N_2}^{Keff} + \frac{B_v}{\kappa_{N_2}} \right)^{-1} N_{N_2}^{eff} \right] \quad (3.89)$$

- **MBFM**

$$\nabla p_{O_2} = RT \left[\frac{(p_{O_2} N_{N_2}^{eff} - p_{N_2} N_{O_2}^{eff})}{p_t D_{O_2 N_2}^{eff}} - \left(D_{O_2}^{Keff} + \frac{B_v}{\chi_{O_2}} \right)^{-1} N_{O_2}^{eff} \right] \quad (3.90)$$

$$\nabla p_{N_2} = RT \left[\frac{(p_{N_2} N_{O_2}^{eff} - p_{O_2} N_{N_2}^{eff})}{p_t D_{O_2 N_2}^{eff}} - \left(D_{N_2}^{Keff} + \frac{B_v}{\chi_{N_2}} \right)^{-1} N_{N_2}^{eff} \right] \quad (3.91)$$

Once the four equations are defined, four boundary conditions are also needed for the solution. These four boundary conditions are obtained from the partial pressures of O_2 and N_2 in both flow channels as shown in Fig. 3.1.

$$p_{O_2}|_{x=0} = x_{O_2}^A p_A \quad (x_{O_2}^A = 1 \text{ for pure oxygen in channel A}) \quad (3.92)$$

$$p_{O_2}|_{x=L} = x_{O_2}^B p_B \quad (x_{O_2}^B = 0 \text{ for pure nitrogen in channel B}) \quad (3.93)$$

$$p_{N_2}|_{x=0} = x_{N_2}^A p_A \quad (x_{N_2}^A = 0 \text{ for pure oxygen in channel A}) \quad (3.94)$$

$$p_{N_2}|_{x=L} = x_{N_2}^B p_B \quad (x_{N_2}^B = 1 \text{ for pure nitrogen in channel B}) \quad (3.95)$$

where p_A and p_B are the total pressures in channel A and B as shown in Fig. 3.1. x_{O_2} and x_{N_2} are the mole fractions of O_2 and N_2 respectively in the channels. The mole fraction of a gas is assumed to be zero in other channel (i.e $x_{O_2}^B = 0$ in N_2 channel). This assumption is valid only in the case when the carrier gas in the channel is flowing much faster compared to the transported gas. As the transported gas is quickly swept away by the bulk stream in the channel, a partial pressure buildup is not possible. Similar boundary conditions have been extensively used for study of mass transport in Stefan tube [52, 63, 64]. If the transport speeds are comparable to the bulk velocity in the channel, a thick boundary layer will develop, which will affect the mass transport process. In the experimentation it was found that the bulk velocities were significantly higher than the transport velocities, so an assumption of infinitely thin boundary layer is used for numerical simulation. The various models were numerically modelled in MATLAB and the differential equations were solved by the boundary value problem solver `bvp4c`. The reason for converting all the equations in the form shown above is that, the solver `bvp4c` requires the differential equations to be given in the form of $y' = f(x, y)$. The solution was achieved within a relative tolerance of 1×10^{-7} . The `bvp4c` is based on finite difference method, and incorporates the three-stage Lobatto IIIa formula[65]. The obtained results and their analysis is presented in the following sections.

Table 3.1 – Problem solving parameters for code validation

Parameter	Value	Reference
Number of GDL	2	N/A
Number of MPL	0	N/A
Assembly Structure	GDL GDL	N/A
Single GDL Thickness	$190\mu m$	SIGRACET catalogue on 24 series GDL
GDL porosity (ϵ)	84%	SIGRACET catalogue on 24 series GDL
GDL permeability (B_v)	$1.138 \times 10^{-11} m^2$	From experiments on 24BA
GDL tortuosity (τ)	$\epsilon^{-0.5}$	Bruggeman correlation
GDL pore size (r_p)	$10\mu m$	Williams et al. [66]
Operating Temperature	$31^\circ C$	Experimental condition
Channel A Pressure	107.3 kPa	Experimental condition
Channel B Pressure	Varying	N/A
Pressure difference	$dp \in [0, 500] Pa$	N/A

3.3 Validation

To check the accuracy of the code, mass transport across a GDL was analyzed. The parameters used for the solution are presented in Table 3.1. To find the tortuosity, Bruggeman correlation has been used. The oxygen pressure in channel 1 is fixed, while the nitrogen pressure in channel 2 is varied to change pressure difference from 0 to 500 Pa. The problem was solved by using all the discussed models and the results were compared with the analytical solution of Fick’s and Darcy’s law.

Figure 3.5 shows the net flux of oxygen as a function of pressure difference across porous media. In this analysis there is no micro porous layer (MPL) present. It can be seen that the analytical and numerical solution of Fick’s and Darcy’s law are an exact match, thus verifying the implementation of the code. It is also noticeable that the flux estimation at low pressure difference is very similar for all the models. At low pressure differences, the viscous transport is negligible. The Knudsen friction will also be almost negligible in GDL, due to its high pore size. Thus the models accounting for them (i.e DGM, BFM, MBFM) will also predict the similar values as the Fick’s and Darcy’s law which doesn’t account for these frictions. The Fick’s and Darcy’s model overpredicts the oxygen flux at higher pressure differences. The reason for the overprediction is that Fick’s and Darcy’s law doesn’t account for interspecies friction and Knudsen friction, which results in less resistance to flux and thus results in higher flux predictions.

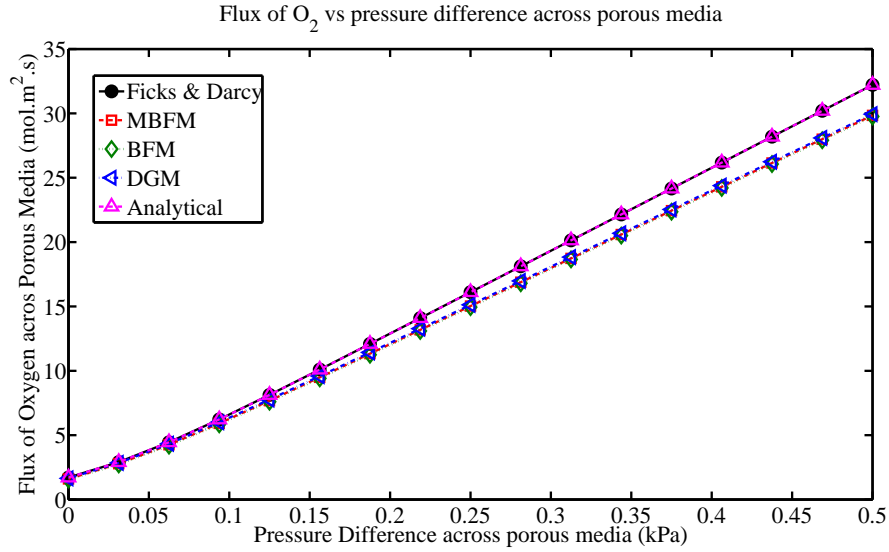


Figure 3.5 – Comparison of oxygen flux variation for different mass transport models

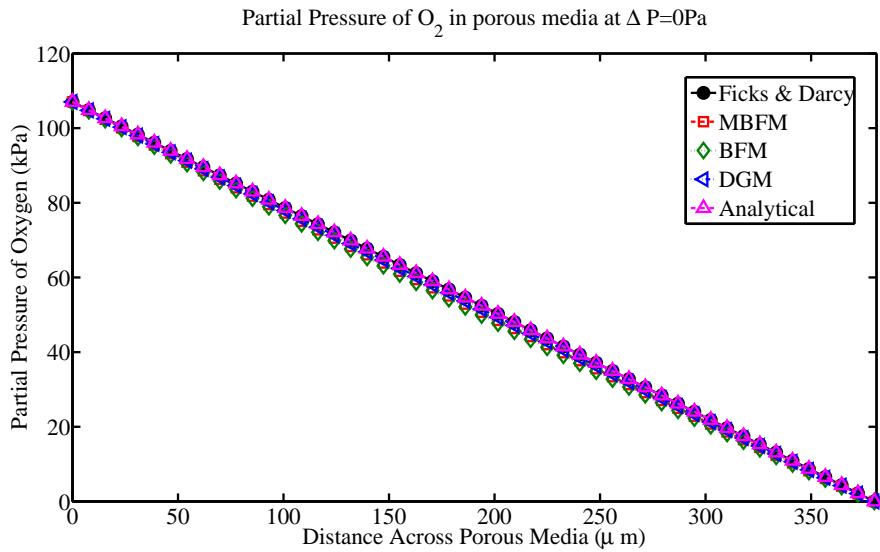


Figure 3.6 – Comparison of oxygen partial pressure across the GDL for different models. Solution at zero pressure difference across porous media

The similarity at low pressure differences can also be verified by Fig. 3.6, which shows the partial pressure profile of O_2 across the GDL for pure diffusion. As the forces acting on the species are similar for all the models, the pressure gradient will also be similar, thus making the profiles match. The partial pressure profile of oxygen for Fick's and Darcy's law is linear, as the pressure gradient for pure diffusion is constant. However, the partial pressure profile of oxygen for other models are slightly

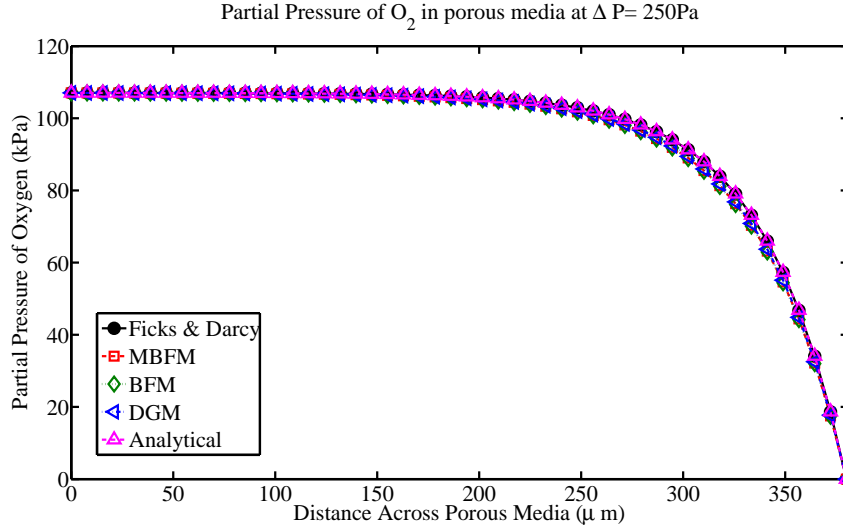


Figure 3.7 – Comparison of oxygen partial pressure across the GDL for different models. Solution at $\Delta p = 250\text{Pa}$ across porous media

non-linear as the net pressure gradient is not constant across porous media. The convection-diffusion analysis is shown in Fig. 3.7 and 3.8, which show the concentration profiles of oxygen for a pressure difference of 250 and 500 Pa across porous media. It can be seen that as the pressure difference increases, the profile becomes more and more asymptotic, due to dominance of convection over diffusion. The analysis in GDL shows that the numerical model has been implemented correctly.

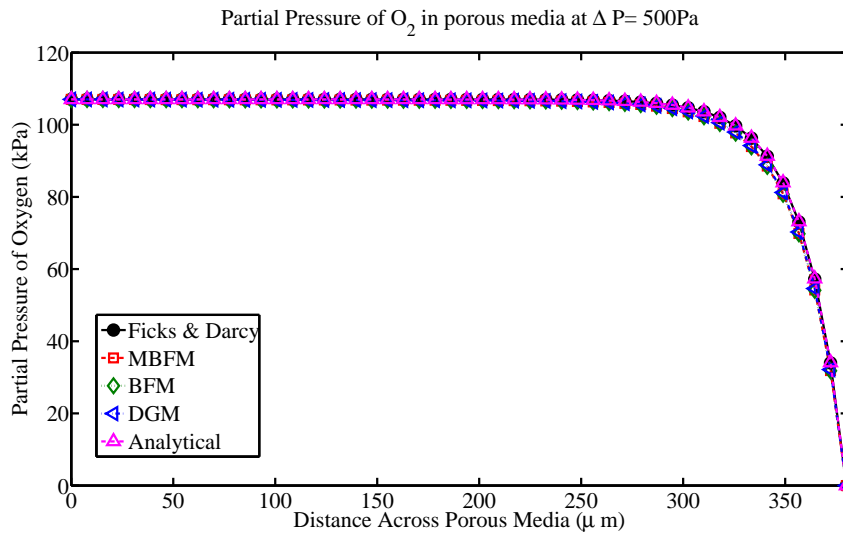


Figure 3.8 – Comparison of oxygen partial pressure across the GDL for different models. Solution at $\Delta p = 500\text{Pa}$ across porous media

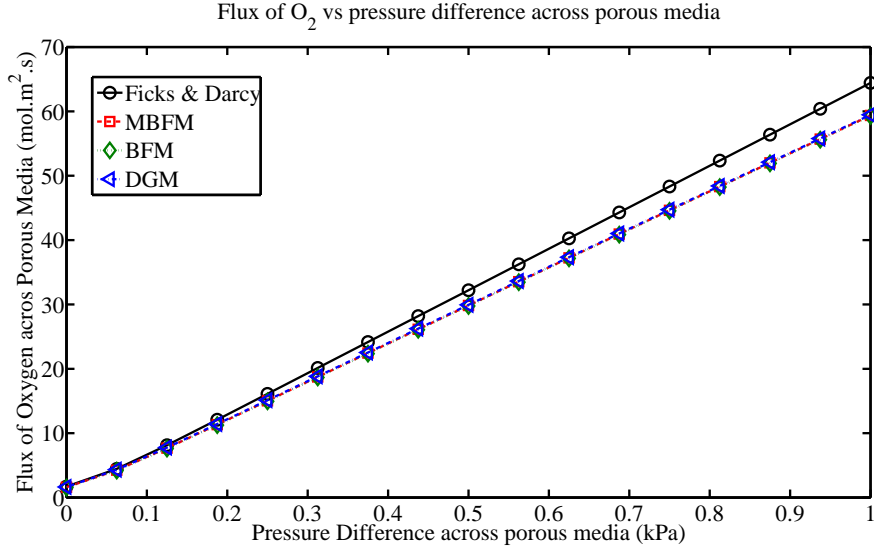


Figure 3.9 – Comparison of oxygen flux variation in GDL for different mass transport models

3.4 Results and Parametric Studies

This section presents the results obtained from numerical simulation of the various mass transport models discussed in section 3.2. To see the effect of GDL and MPL clearly on the mass transport, the simulations have been performed for three different conditions: with GDL only, with MPL only and with GDL and MPL.

3.4.1 Mass Transport in Gas Diffusion Layers

The mass transport models were solved for the same problem parameters as specified in Table 3.1. The only difference is that the pressure difference between the channels is varied from 0 to 1 kPa ($dp \in [0, 1]$ kPa). This pressure range is sufficient to observe various effects of pressure difference on mass transport in GDLs. Figure 3.9 shows the variation in flux for increase in pressure difference across porous media. As discussed in section 3.3, it is observed that all the models except Fick's and Darcy's have similar predictions. However, the Fick's and Darcy's model overpredicts the oxygen flux at higher pressure differences. The reason for the overprediction is that Fick's and Darcy's law doesn't account for interspecies friction and Knudsen friction, which results in less resistance to flux and thus results in higher flux predictions.

The partial pressure profiles of oxygen across the GDL are shown in Fig. 3.6, 3.7, 3.8 and 3.10. The partial pressure profile for pure diffusion shown in Fig. 3.6, shows

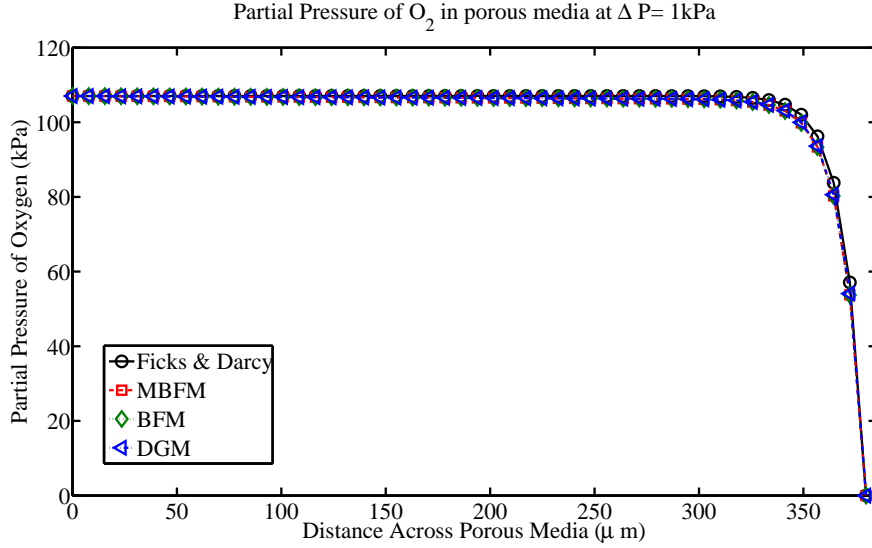


Figure 3.10 – Comparison of oxygen partial pressure across the GDL for different models. Solution at $\Delta p = 1\text{kPa}$ across porous media

negligible difference between different models. In this condition, diffusion will be the dominant mode of mass transfer, as convection is zero at $\Delta p = 0$ and also due to large pore size of GDL, Knudsen transport is negligible. The diffusive transport is governed by the partial pressure gradient, which will be very similar for all the models, thus the diffusive transport values predicted by all models are similar. At higher pressure differences, the partial pressure gradient is higher for Fick's and Darcy's law. Figure 3.10 shows the pressure profile at pressure difference of 1kPa. In the left part of the GDL ($0 < x < L$), the partial pressure profile is almost flat for Fick's and Darcy's model. This is due to dominance of convective transport, which drags O_2 molecules with it and reduces the partial pressure gradient. For other models convective transport is still dominant, however interspecies friction also plays a role. This results in the small gradient in pressure profile for other models. At the end of the GDL there is a sharp change in partial pressure to meet the boundary condition.

The variation of nitrogen flux with increase in pressure difference across the porous media is shown in Fig. 3.11. For zero pressure difference, the flux of nitrogen is equal to the oxygen flux for Fick's and Darcy's model. For other models, it is marginally different (e.g. $N_{O_2} = 1.6454\text{mol}/\text{m}^2\text{s}$, $N_{N_2} = -1.759\text{mol}/\text{m}^2\text{s}$ for DGM), resulting in a net total mixture flux. This validates the concern raised in section 3.2.2 regarding the validity of DGM. The DGM uses Darcy's law to calculate the viscous flux of mixture, which is also equal to the net mixture flux. Therefore, at zero net pressure

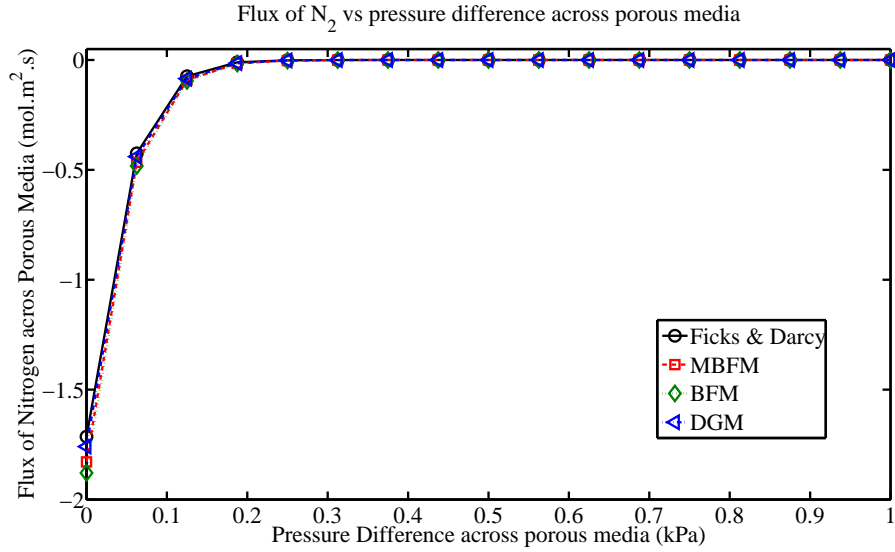


Figure 3.11 – Comparison of nitrogen flux variation in GDL for different mass transport models

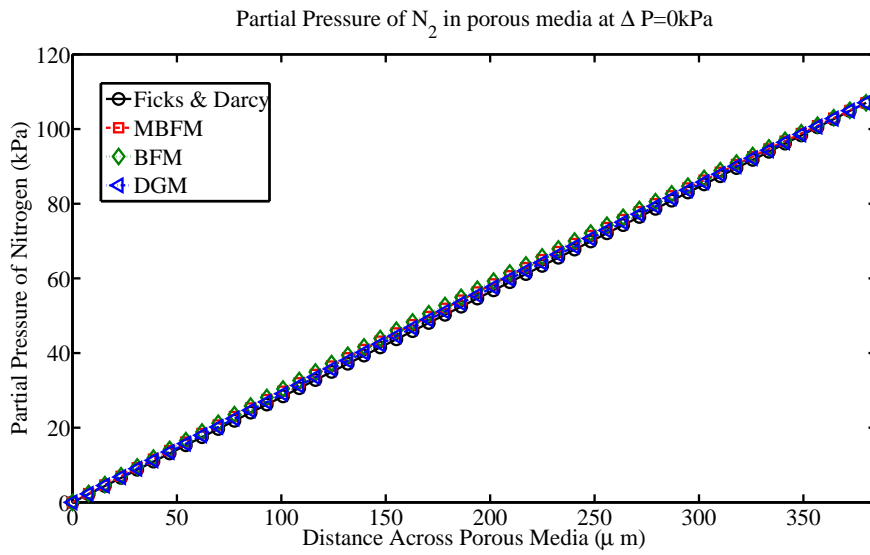


Figure 3.12 – Comparison of nitrogen partial pressure across the GDL for different models. Solution at zero pressure difference across porous media

difference, the net mixture flux should be zero. The BFM and MBFM treat each species independently, and thus will not predict a zero mixture flux.

As the pressure difference increases, the flux of nitrogen decreases in value, because the pressure difference is acting against the nitrogen pressure gradient. The convective transport overtakes the diffusive transport of nitrogen and finally after a certain pressure drop the nitrogen flux goes to zero. This is also evident from the

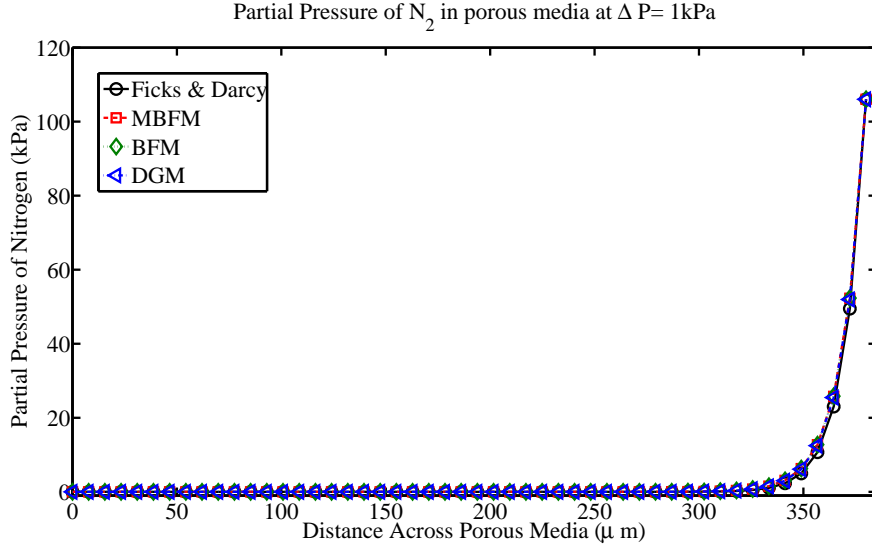


Figure 3.13 – Comparison of nitrogen partial pressure across the GDL for different models. Solution at $\Delta p = 1$ kPa across porous media

partial pressure profiles of nitrogen shown in Fig. 3.12 and 3.13. Figure 3.12 shows the partial pressure profile of nitrogen for zero pressure difference across GDL. The partial pressure profiles vary in a similar manner to oxygen profiles for pure diffusion. Figure 3.13 shows the partial pressure profiles of nitrogen for a pressure difference of 1 kPa across GDL. As the pressure difference acting against nitrogen increases, nitrogen can diffuse only near its flow channel. In rest of the porous media, nitrogen is flushed out by high convective transport.

3.4.2 Mass Transport in Micro Porous Layers

This section presents mass transport studies on a micro porous layer. The geometrical parameters of the MPL are significantly different from the GDL, and so the transport properties will also be different. Hence a noticeable difference should be observed in the mass transport. The problem solving parameters are shown in Table 3.2.

Figure 3.14 shows the oxygen flux at different pressure differences across the MPL. At low pressure differences, all models except DGM are in good agreement. The DGM underpredicts the flux of oxygen compared to other models. At high pressure differences, the DGM predictions are similar to other models. However Fick's and Darcy's model overpredicts the fluxes at higher pressure differences. In a MPL, Knudsen friction is dominant due to pores sizes in the range of 10 nm. The Fick's

Table 3.2 – Problem solving parameters for MPL simulation

Parameter	Value	Reference
Number of GDL	0	N/A
Number of MPL	2	N/A
Assembly Structure	MPL MPL	N/A
Single MPL Thickness	45 μ m	SIGRACET catalogue on 24 series GDL
MPL porosity (ϵ)	42.2%	SIGRACET catalogue on 24 series GDL
MPL permeability (B_v)	2.841 $\times 10^{-14} m^2$	From experiments on 24BC
MPL tortuosity (τ)	$\epsilon^{-0.5}$	Bruggeman correlation
MPL pore size (r_p)	10nm	Martinez et al. [67]
Operating Temperature	31°C	Experimental condition
Channel 1 Pressure	107.3 kPa	Experimental condition
Channel 2 Pressure	Varying	N/A
Pressure Difference	$dp \in [0, 20]$ kPa	N/A

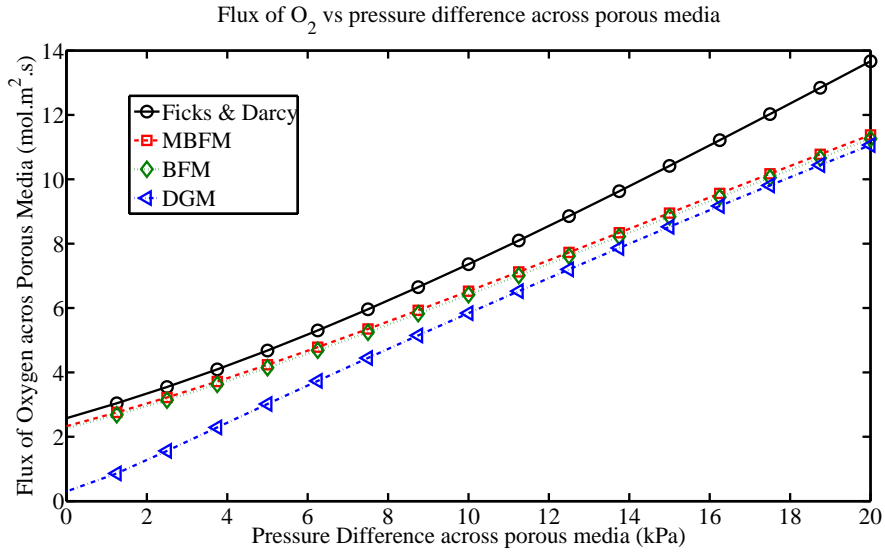


Figure 3.14 – Comparison of oxygen flux variation in MPL for different mass transport models

and Darcy's model does not account for Knudsen friction. The BFM and MBFM account for it in parallel with viscous friction, which reduces the net resistance as viscous friction is less dominant. The DGM fully accounts for the Knudsen friction and thus have the highest resistance for oxygen transport. Due to the high resistance, DGM underpredicts the flux values at low pressure differences. At high pressure differences, Fick's and Darcy's model fully accounts for the viscous flux without any additional resistances. However in BFM, MBFM and DGM Knudsen friction is still present, reducing the net oxygen flux. This explains the overprediction of Fick's and Darcy's model at higher pressure differences. The increasing dominance of viscous flux at higher pressure differences also results in the DGM, BFM and MBFM values to converge.

The predicted partial pressure profile of oxygen for zero pressure difference across the MPL, obtained the different models is shown in Fig. 3.15. As discussed earlier, the convective transport is negligible at zero pressure difference and only molecular diffusion and Knudsen diffusion are present. The interspecies friction force will be nearly constant across the porous media for pure diffusion, due to the oxygen and nitrogen pressure gradients being almost the same. The Knudsen friction depends only on the geometric properties, and thus will also remain constant across porous media. This near constant net resistance results in having almost linear pressure profile across the porous media, as shown in Fig. 3.15. Figure 3.16 and 3.17 show the partial pressure profiles for a pressure difference of 10 and 20 kPa respectively across MPL. For DGM, the convection dominated mass transport results in almost exponential partial pressure profile, similar to the one for GDL in Fig. 3.10. The molecular transport in Fick's & Darcy's model and Knudsen transport in BFM/MBFM are equally dominant compared to viscous transport. The molecular diffusion and Knudsen diffusion results in a linear partial pressure profile, while convective transport results in exponential profile. For a case where both the transport methods are dominant, the linear nature of Knudsen or Fick's combined with exponential nature of convective transport gives the pressure profile a less asymptotic nature.

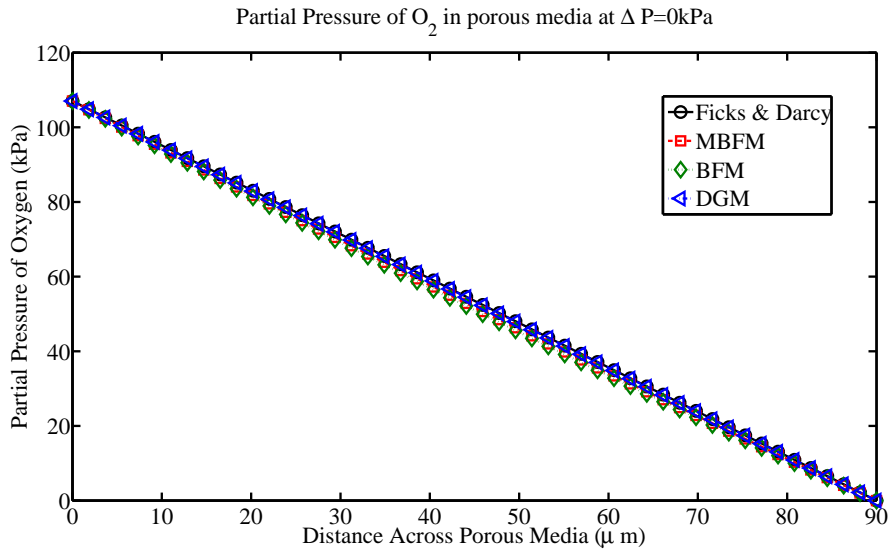


Figure 3.15 – Profile of oxygen partial pressure across MPL, predicted by different models. Solution at zero pressure difference across porous media

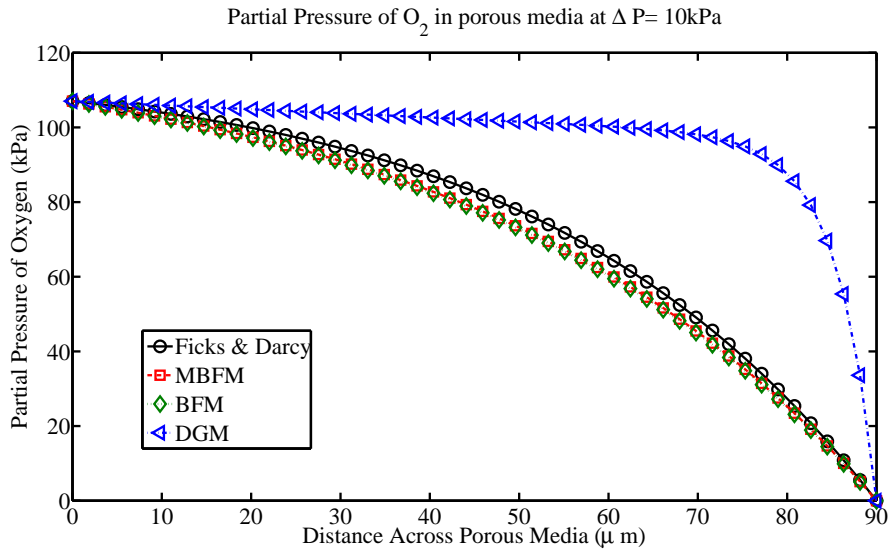


Figure 3.16 – Profile of oxygen partial pressure across MPL, predicted by different models. Solution at $\Delta p = 10\text{kPa}$ across porous media

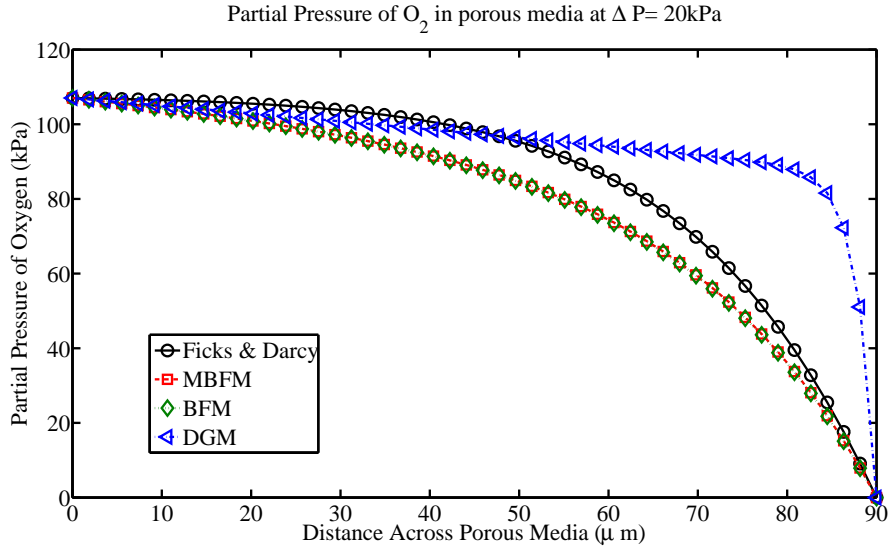


Figure 3.17 – Profile of oxygen partial pressure across MPL, predicted by different models. Solution at $\Delta p = 20\text{kPa}$ across porous media

Figure 3.18 shows the nitrogen flux with increase in pressure difference across the MPL. At zero pressure difference the DGM has the highest resistance and thus predicts the lowest value of flux. At higher pressure differences the DGM still has a higher net resistance. However as the pressure difference increases, the oxygen flux and net mixture flux increases, flushing out the nitrogen. Above a certain pressure difference, the DGM is completely convection dominated, which is acting against nitrogen flux and results in having a zero flux for nitrogen. For other models, the convective transport is not so dominant and thus the nitrogen flux is higher in value. At extremely high pressure differences the convective flux dominates in all models and the nitrogen flux becomes zero.

Figure 3.19 shows the partial pressure profile of nitrogen across MPL for zero pressure difference. For Fick's and Darcy's law, only molecular diffusion is dominant, which results in a linear partial pressure profile. In DGM, BFM and MBFM, molecular and Knudsen diffusion are dominant, which also result in an almost linear partial pressure profile. The interesting fact to note here is that, even though all the models predict almost the same pressure profile for pure diffusion, the values of predicted flux are quite different. In other words, the pressure gradient is not the only governing parameter of mass transport. Similar conclusions can also be made for the oxygen flux at pure diffusion in Fig. 3.14.

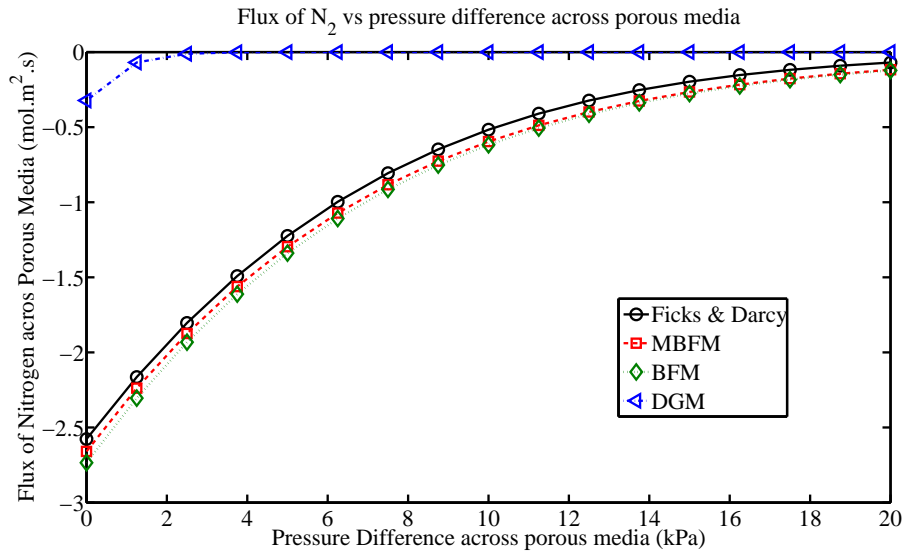


Figure 3.18 – Comparison of nitrogen flux variation with increase in pressure difference in MPL, for different mass transport models

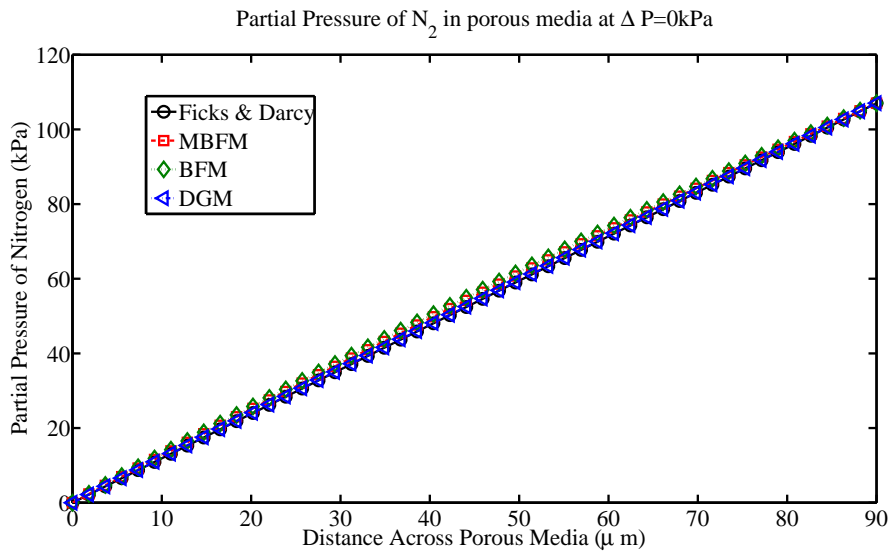


Figure 3.19 – Profile of nitrogen partial pressure across MPL, predicted by different models. Solution at zero pressure difference across porous media

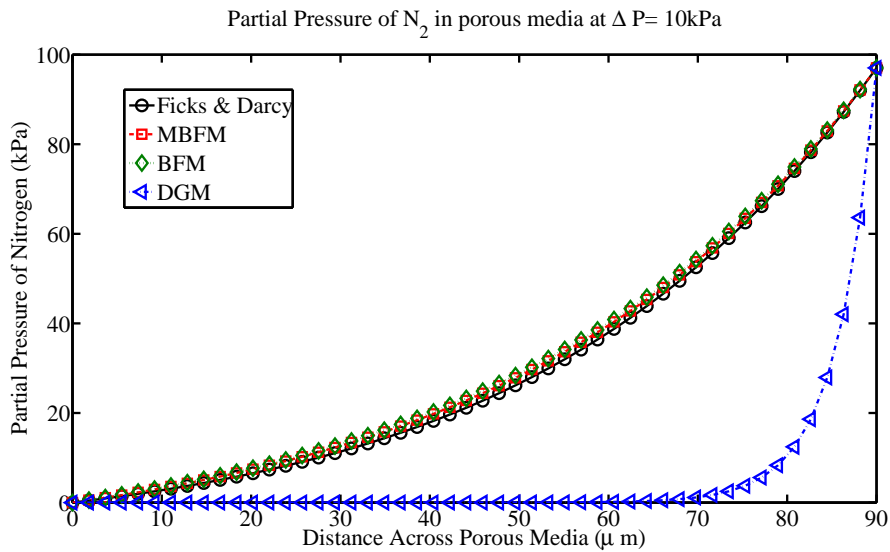


Figure 3.20 – Profile of nitrogen partial pressure across MPL, predicted by different models. Solution at $\Delta p = 10\text{kPa}$ across porous media

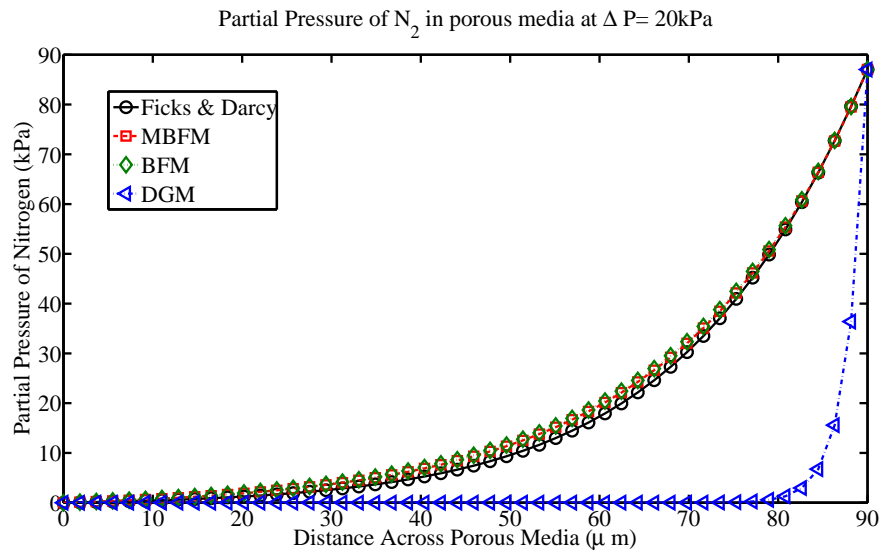


Figure 3.21 – Profile of nitrogen partial pressure across MPL, predicted by different models. Solution at $\Delta p = 20\text{kPa}$ across porous media

Figure 3.20 and 3.21 show the partial pressure profile of nitrogen for a pressure difference of 10 and 20 kPa across porous media. Due to dominance of convective transport in the DGM, the profile is almost exponential. As all the N_2 is flushed out by convective transport, the partial pressure of nitrogen is zero for most part of the MPL. At the end of MPL a sharp rise in pressure occurs to meet the boundary condition. In other mass transport models (i.e. Fick's & Darcy, BFM and MBFM), all the modes of mass transport are equally important. This results in a partial pressure profile which is less asymptotic.

3.4.3 Mass Transport in GDL MPL Assemblies

The effect of GDL and MPL on different modes of mass transport has been studied in previous sections. With this understanding, a full scale simulation of a GDL MPL assembly have been done. The problem solving parameters are shown in Table 3.3. The porous media assembly used for simulation is similar to the one used for experimentation.

Figure 3.22 shows the variation in oxygen flux with increases in pressure difference across porous media assembly. The flux profile is similar to the one observed for only an MPL. In a GDL-MPL assembly, GDL resistance to flux is almost negligible compared to the MPL resistance, thus the flux trend is similar to later. The DGM underpredicts the mass transfer at low pressure differences compared to other models. However, at high pressure differences, the flux values of DGM are similar to the one predicted by BFM and MBFM. The Fick's and Darcy's model however starts overpredicting at high pressure differences. The behaviour of DGM can also explain why the experimental studies presented by Evans III et al. [49] are validated by both DGM and BFM [26], because the studies have been carried at high pressure differences in range of 5-30 kPa.

Table 3.3 – Problem solving parameters for GDL-MPL assembly simulation

Parameter	Value
Number of GDL	2
Number of MPL	2
Assembly Structure	GDL MPL MPL GDL
GDL properties	As shown in Table 3.1
MPL properties	As shown in Table 3.2
Operating parameters	As shown in Table 3.1

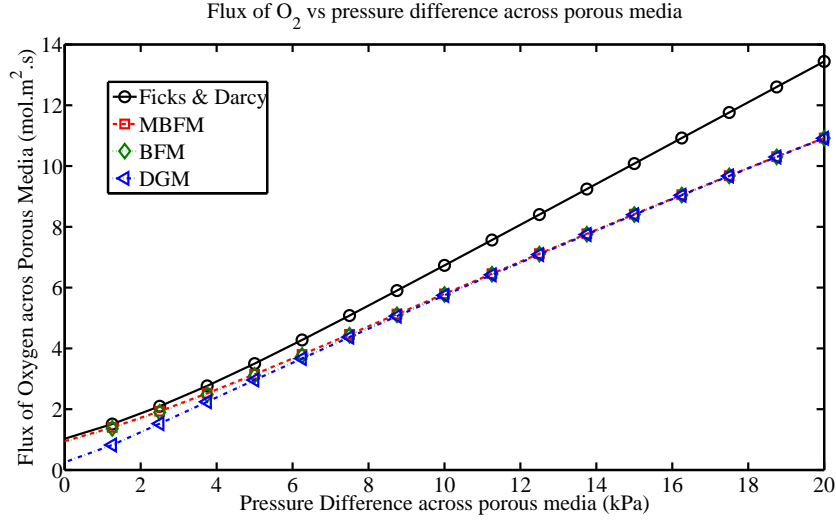


Figure 3.22 – Comparison of oxygen flux variation in GDL-MPL assembly for different mass transport models

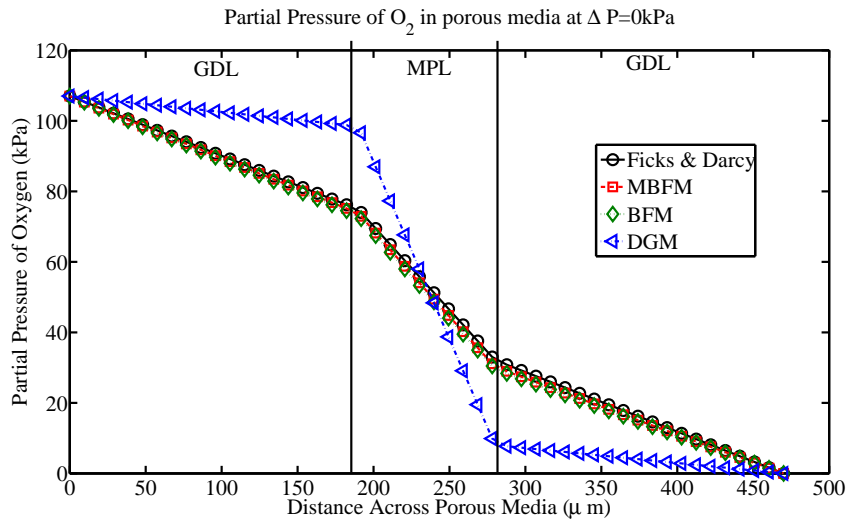


Figure 3.23 – Profile of oxygen partial pressure across GDL- MPL assembly, predicted by different models. Solution at $\Delta p = 0$ kPa across porous media

The partial pressure profile of oxygen across the porous media assembly for a zero pressure difference is shown in Fig. 3.23. The profiles for all models except DGM are similar, where the DGM have a higher pressure gradient in the MPL. The reason for higher pressure gradient in the DGM is that it overpredicts the frictional forces by accounting for Knudsen friction completely. In other models like BFM and MBFM, Knudsen friction is accounted in parallel with viscous friction, thereby reducing the net friction. The Fick's and Darcy's law does not account for Knudsen friction at all, hence the total friction is less.

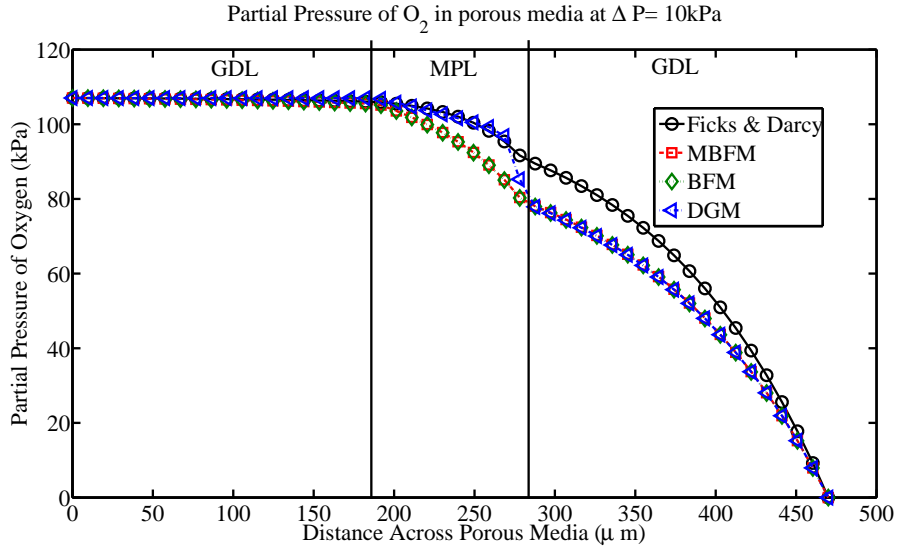


Figure 3.24 – Profile of oxygen partial pressure across GDL- MPL assembly, predicted by different models. Solution at $\Delta p = 10\text{kPa}$ across porous media

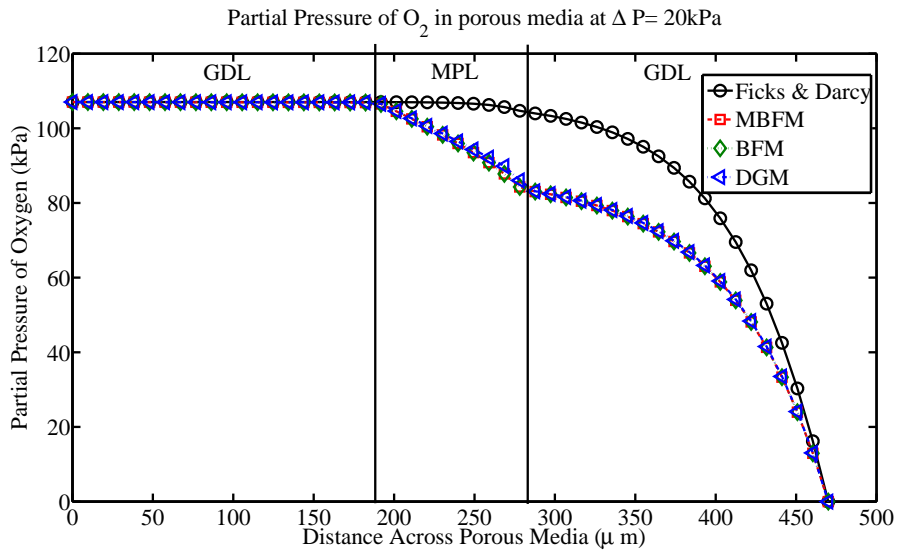


Figure 3.25 – Profile of oxygen partial pressure across GDL- MPL assembly, predicted by different models. Solution at $\Delta p = 20\text{kPa}$ across porous media

Figure 3.24 and 3.25 show the oxygen partial pressure profile for the porous media assembly, under a pressure difference of 10 and 20 kPa respectively. As the pressure difference increases, the transport in the left GDL is completely dominated by convection. Thus the partial pressure profile in left GDL is the same for all models at high pressure difference. In the MPL, the DGM profile slowly matches up with BFM and

MBFM for higher pressure differences. The Fick's and Darcy's profile is exponential in nature due to high convective transport and different from other models.

3.5 Conclusion

A detailed analysis of mass transport in porous media was presented in this chapter. Various model available in literature were described and reviewed, and a new modified binary friction model (MBFM) was presented. The various models were solved using numerical modelling in MATLAB. The code was shown to be in perfect agreement with analytical data in section 3.3. The simulation predicts the fluxes and partial pressure profiles in the porous media, for different models of mass transport in GDL-MPL assemblies. It was found that the MPL is the limiting factor in mass transport, due to high value of Knudsen and viscous friction. In the study of micro porous layers, Knudsen friction was found to be a significant factor. This raises questions on applicability of conventional models like Fick's and Darcy's equation in micro porous layers, as these do not account for wall interactions.

Chapter 4

Results on Permeability and Diffusivity Measurements and Discussion

This chapter presents the results obtained from the experimental setup presented in chapter 2. The obtained results are analyzed using various theoretical models presented in chapter 3 to estimate the transport properties of porous media. Section 4.1 presents the experimental results on permeability measurement and parameter estimation. The conventional approach of Darcy-Forchheimer equation as well as a new approach of binary friction model (BFM) for permeability estimation is presented. Section 4.2 discusses mass transport measurements in porous media and discusses diffusivity estimation using the theoretical models presented in chapter 3.

4.1 Permeability Measurements in Porous Media

The permeability measurement setup described in section 2.2 is used for permeability measurements. The gas flow rate across the porous media is varied by the means of mass flow controller and the corresponding pressure drop is recorded. A pressure drop vs flow rate profile, similar to the one presented in Fig. 2.17 is obtained. The velocity across the porous media is obtained by dividing the flow rate with mass transport aperture cross section as follows:

$$v = \frac{\dot{Q}}{\pi D^2/4} \quad (4.1)$$

where \dot{Q} is the volumetric flow rate of gas across porous media and D is diameter of the porous media aperture.

Conventionally the pressure gradient vs velocity data is fitted to Darcy's equation. However, to account for inertial effects at higher velocities, the Darcy-Forchheimer equation has been used as follows: [55]

$$\frac{dp}{dx} = -\frac{\eta}{B_v}v - \frac{\rho}{B_1}v^2 \quad (4.2)$$

where B_v and B_1 are the viscous and inertial permeabilities respectively; ρ is the density of the fluid, which is found by using ideal gas law and η is the viscosity of fluid which is estimated from Reid et al. [28, eq. (9-3.9), pp. 392] for oxygen and nitrogen. As per the assumptions of Darcy's law in 1-D, the pore average velocity across the porous media can be assumed to be constant [18]. Hence the total pressure variation will be linear. The following equation can be obtained for a single layer of porous media to replace eq. (4.2):

$$\frac{p_1 - p_2}{L} = \frac{\Delta p}{L} = \frac{\eta}{B_v}v + \frac{\rho}{B_1}v^2 \quad (4.3)$$

where p_1 and p_2 are the pressure values on each side of the porous media. For multiple layers of porous media with varying permeability, the experimental measurement can only obtain effective values of permeability. To know the permeability of each layer exclusively, the effective permeability needs to be separated into its components [55].

Figure 4.1 shows an assembly of various porous media with varying permeability values. The total pressure drop across porous media can be given as follows:

$$\frac{\Delta p}{L} = \frac{\eta}{B_v^{eff}}v + \frac{\rho}{B_1^{eff}}v^2 \Rightarrow \Delta p = \frac{\eta}{B_v^{eff}}Lv + \frac{\rho}{B_1^{eff}}Lv^2 \quad (4.4)$$

where B_v^{eff} and B_1^{eff} are the effective viscous and inertial permeability values and L is total thickness. For a single layer of porous media, the equation can be given as follows:

$$\frac{\Delta p_i}{L_i} = \frac{\eta}{B_v^i}v + \frac{\rho}{B_1^i}v^2 \Rightarrow \Delta p_i = \frac{\eta}{B_v^i}L_i v + \frac{\rho}{B_1^i}L_i v^2 \quad (4.5)$$

where Δp_i is the pressure drop in the i^{th} layer of the porous media, and B_v^i and B_1^i are the viscous and inertial permeability values of the i^{th} layer. Assuming a constant velocity across porous media, the pressure drop in all layer can be summed up as follows [55]:

$$\Delta p = \sum_{i=1}^n \Delta p_i = \eta v \sum_{i=1}^n \frac{L_i}{B_v^i} + \rho v^2 \sum_{i=1}^n \frac{L_i}{B_1^i} \quad (4.6)$$

where Δp is the total pressure drop across the entire porous media assembly. Comparing eq. (4.6) with eq. (4.4), the following expressions can be obtained for effective

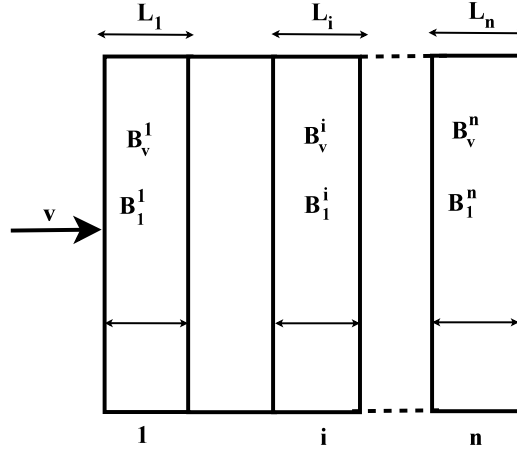


Figure 4.1 – A schematics of multiple layer assembly in permeability measurement

permeability of porous media [55]:

$$\frac{L}{B_v^{eff}} = \sum_{i=1}^n \frac{L_i}{B_v^i} \quad (4.7)$$

$$\frac{L}{B_1^{eff}} = \sum_{i=1}^n \frac{L_i}{B_1^i} \quad (4.8)$$

The effective permeability values can be measured by experimentation on GDL-MPL assemblies. To know the permeability of n^{th} layer, the permeability of other $n - 1$ layers must be known. Therefore in case of a GDL-MPL assembly, the GDL permeability have to be estimated in order to obtain MPL permeability.

4.1.1 Permeability Measurements in Gas Diffusion Layers

This section describes the permeability measurement in the gas diffusion layer (GDL) of a PEM fuel cell. A SGL SIGRACET GDL (model: 34BA) was used for experimentation. Four layers of the GDL were assembled together to make the porous media assembly as discussed in section 2.1.2. Figure 4.2 shows the schematics of the GDL assembly used in the experimentation. The reason for using four layers of GDL was to create sufficient pressure drop across the porous media assembly, so that it can be measured by the pressure transducer. At the same time, the number of GDL can not be too high as it will create problems in sealing the porous media assembly within the chip. As discussed in section 2.2.1, multiple experiments were done to ensure repeatability of data. In this case, six sets of experiments were done with oxygen on the GDL assembly.

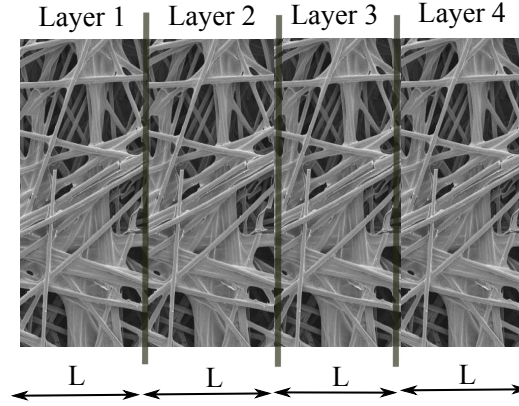


Figure 4.2 – Overview of a SGL SIGRACET 34BA GDL assembly (Individual GDL SEM images adopted from Zamel et al. [4])

The average pressure drop vs velocity profile for the 34BA assembly is shown in Fig. 4.3. The average data was fitted to Darcy-Forchheimer equation for single layer given by eq. (4.3). It can be seen that the Darcy-Forchheimer equation is in good agreement with the experimental data. The margin of error in measurements is negligible, so it is not shown in the figure. The maximum error between the datafit and the experimental data was found to be around $\pm 3\%$. To confirm the reliability of the experimental data, the experiment was repeated with a second sample of 34BA, and similar results were observed as shown in Fig. 4.4. The difference between the two profiles can be attributed to the slight difference in thickness and cross sections of the two samples. In the current experiment, the difference between two different samples was found to be around $\simeq 10\%$, even though the two samples were from the same sheet of GDL.

Table 4.1 shows the permeability values for both the samples and their comparison with the earlier results presented by Gostick et al. [54] for 34BA. Comparing with the literature values of Gostick et al. [54] it can be seen that the obtained values have similar order of magnitude but values are quite different. In earlier experiments, the permeability of two SGL SIGRACET 24BC porous media from different batches was measured. The permeability value were found to be $1.462 \times 10^{-13} m^2$ and $5.96 \times 10^{-14} m^2$. This shows that there is significant variability between different batches, which can be due to the fabrication uncertainties. The samples used by Gostick et al. [54] were from a different batch than the one used in the current experiment, hence the difference in results is observed. The variation in inertial permeability between samples is much higher. The reason for this is the second order dependence on velocity across porous media. For low velocities, the inertial term

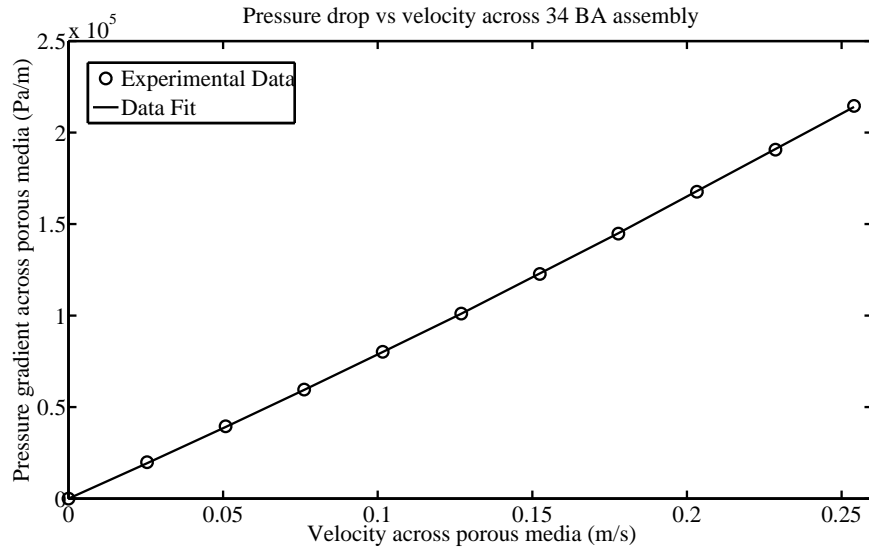


Figure 4.3 – The pressure drop vs velocity profile with oxygen for 34 BA and its comparison with datafit

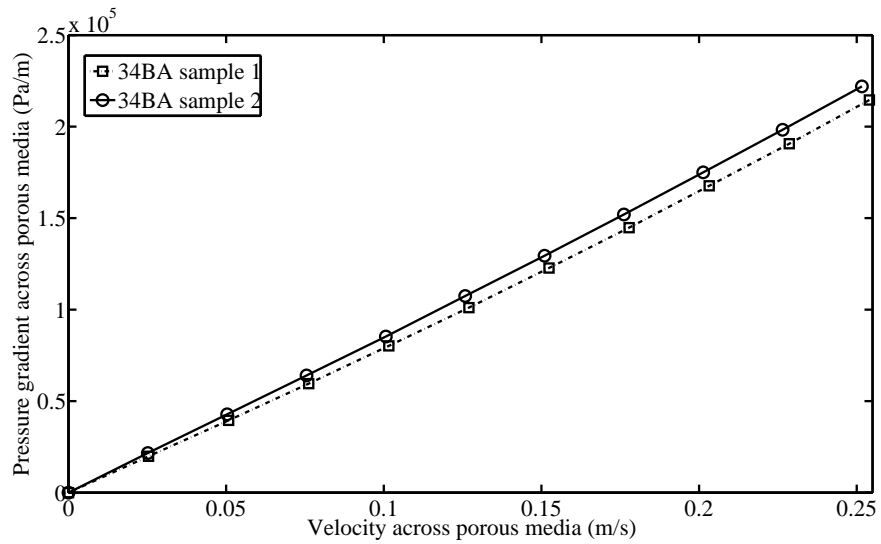


Figure 4.4 – Comparison of pressure gradient vs velocity profiles for two samples of 34BA

Table 4.1 – Permeability values for a SGL SIGRACET 34BA GDL

Parameter	Sample1	Sample2	Literature Value
Viscous permeability (m^2)	2.91×10^{-11}	2.65×10^{-11}	$1.63 \times 10^{-11} \pm 5.505\%$
Inertial permeability (m)	3.61×10^{-6}	6.22×10^{-6}	$\simeq 1.21 \times 10^{-5}$

will be almost negligible and the associated error will be much higher. The inertial permeability is not used in any model discussed in chapter 3, so it is ignored.

4.1.2 Permeability Measurements in Micro Porous Layers

This section presents the permeability measurements in micro porous layers (MPL) of a PEM fuel cell. A SGL SIGRACET porous media (model: 34BC) was used for experimentation, where the micro porous layer is coated on top of the gas diffusion layer (SIGRACET 34BA). As the permeability values of GDL and MPL are different, the multi layer approach given by eq. (4.4) is adopted for estimating MPL permeability.

The schematics of the porous media assembly used in the experiment is shown in Fig. 4.5. Two 34BC layers were combined together in a mirror image formation to provide sufficient resistance and to make similar boundary conditions on both channels. To ensure data repeatability, six sets of experiments were carried out with oxygen flow and an average pressure drop vs velocity profile was obtained.

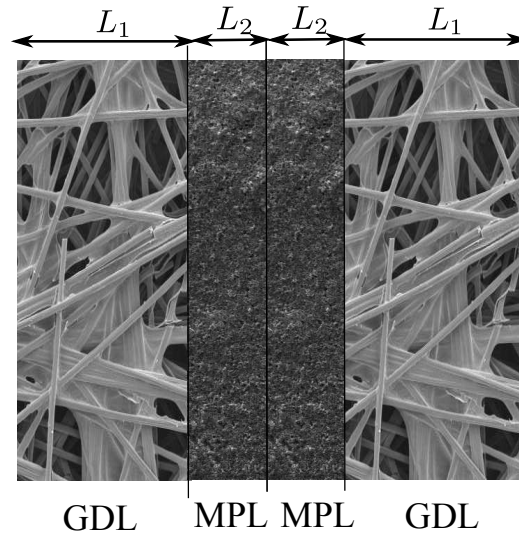


Figure 4.5 – Overview of a SGL SIGRACET 34BC GDL-MPL assembly (Individual GDL SEM images adopted from Zamel et al. [4])

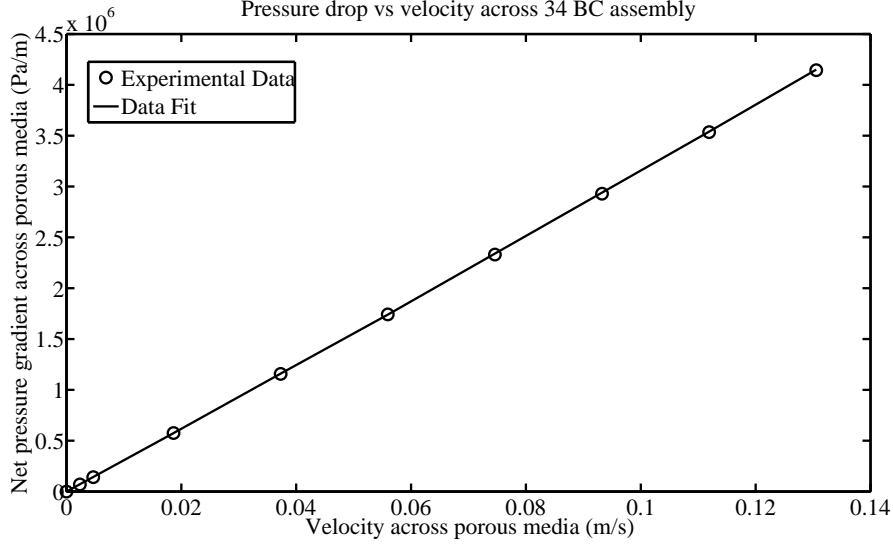


Figure 4.6 – Net pressure drop vs velocity profile for SGL SIGRACET 34BC assembly

Figure 4.6 shows the net pressure gradient vs velocity for the 34BC assembly. The experimental data was fitted to eq. (4.4) to get effective permeability values. The maximum error between the Darcy-Forchheimer data fit and experimental values was found to be around $\pm 2.8\%$. To confirm the reliability of the data, experimentation was done on another assembly of SGL SIGRACET 34BC and similar results were obtained. Table 4.2 shows the permeability values for both samples and their comparison with results presented by Gurau et al. [55]. The viscous and inertial permeability values for both samples are close to each other, confirming the reliability of the experiment. Gurau et al. [55] have presented permeability measurements on GDL-MPL assemblies. However the experiments have been performed on a different porous media which had 30% PTFE coating compared to 5% PTFE coating in SIGRACET 34BC. The experiments by Gurau et al. [55] were performed on different types of porous media and the permeability variation range has been shown in Table 4.2. The values have been only used as a reference and to confirm that the permeability values obtained in current experiment are similar.

Table 4.2 – Permeability values for a SGL SIGRACET 34BC GDL-MPL assembly

Parameter	Sample1	Sample2	Literature Value
Viscous permeability (m^2)	7.14×10^{-13}	7.01×10^{-13}	$4.4 \times 10^{-13} - 7.9 \times 10^{-13}$
Inertial permeability (m)	1.57×10^{-7}	1.59×10^{-7}	$0.63 \times 10^{-7} - 3.4 \times 10^{-7}$

Table 4.3 – Geometric parameters and permeability calculations for a SGL SIGRACET 34BC GDL-MPL assembly

Parameter	Sample 1	Sample 2
GDL (34BA) thickness (μm)	254	251
MPL thickness (μm)	62	64
Total (34BC) thickness (μm)	316	315
GDL (34BA) permeability (m^2)	2.91×10^{-11}	2.65×10^{-11}
MPL permeability (m^2)	1.429×10^{-13}	1.454×10^{-13}
Overall (34BC) permeability, (m^2)	7.14×10^{-13}	7.01×10^{-13}

The parameter of interest in this case is the viscous permeability of the micro porous layer. To find the values of MPL permeability, eqs. (4.7) and (4.8) are used with values of the GDL permeability and the overall permeability from Table 4.2. The MPL permeability can be given by the following equation:

$$B_v^{MPL} = L_{MPL} \left(\frac{L}{B_v^{eff}} - \frac{L_{GDL}}{B_v^{GDL}} \right)^{-1} \quad (4.9)$$

Table 4.3 shows the geometrical parameters of each layer and their permeability values. The thickness of the SIGRACET 34BA GDL and SIGRACET 34BC GDL-MPL assembly was measured by a micrometer. The MPL thickness was obtained by subtracting GDL thickness from the total thickness of 34BC assembly. The MPL permeability values calculated by eq. (4.9) are also shown in the table. It can be seen that the MPL permeability values are two orders of magnitude less than the GDL permeability. Due to such low permeability, the MPL becomes the convective transport limiting layer in the this assembly. The layer specific permeability values can be used for better modelling of convective transport in GDL-MPL assemblies.

4.1.3 Limitations of Darcy’s Law and a New Approach to Calculate Permeability

Darcy’s law has been extensively used to study flow in porous media. Darcy’s law is an approximation of Navier-Stokes equation for very low flow velocities where the flow can be assumed as a Stokes flow [18, 68, 69]. The corrections for non-Stokes flows include addition of the inertial forces, also known as the Forchheimer term and other corrections [69]. In fuel cell porous media, the convection velocities are low, hence the Stokes flow assumption can be applied.

The basic Navier-Stokes equation is based on a continuum assumption in the flow, which is only applicable if volume averaging can be done on the system length scale.

For rarefied gases or for very small length scales, the number of molecules within the system length scale are not sufficient for volume averaging and continuum assumption breaks down. To know the validity of the continuum approach in micro-nano pores of a PEM fuel cell, Knudsen numbers can be used. The Knudsen number is defined as follows:

$$Kn = \frac{\lambda}{L} \quad (4.10)$$

where L is the characteristic length and λ is mean free path of the gas molecules given as follows [70]:

$$\lambda = \frac{m}{\pi\rho\sigma^2\sqrt{2}} \quad (4.11)$$

where m is the molecular mass of the gas, ρ is the density and σ is the collision diameter. The pore sizes in a GDL and MPL range within $10 - 150\mu m$ [66, 67] and $2 - 120nm$ [67, 71] respectively. For calculation purpose, the average pore size of the GDL is taken as $60\mu m$ and for the MPL is taken as $60nm$. For the current experiment the mean free path for several gases were calculated at $26^\circ C$ and atmospheric pressure. Table 4.4 shows the Knudsen number calculations for several gases in GDL and MPL. The various flow regimes are based on the Knudsen number, which are given in Table 4.5. It can be observed from Table 4.4 that only in case of oxygen and nitrogen flow in GDL, the Knudsen number is around 0.001, thereby enabling the use of Darcy's law. For most of the cases the flow in PEMFC electrodes will be in the transition region, hence the use of Darcy's law will give erroneous results.

To verify the deviation from Darcy's law at high Knudsen numbers, further permeability experiments on the SGL SIGRACET34 BA GDL were done with helium. The permeability values obtained earlier with oxygen, as shown in Table 4.1 were used for comparisons. The viscosity values for helium was taken as $1.9912 \times 10^{-5} Pa \cdot s$ [73]. The difference between permeability values in both experiments was found to be around $\pm 8\%$. As shown in Table 4.4, the helium flow in the GDL is in transition region and the molecular weight of helium is different from oxygen. Since in the transition region, the effects of Knudsen transport will be present. Hence, there is a difference between the experimental and predicted pressure drop values.

Table 4.4 – Knudsen number calculations for different gases in GDL and MPL

Parameter	H_2	He	O_2	N_2
Mean free path, λ (nm)	121.1	190.1	69.3	64.4
Kn in GDL	0.002	0.003	0.001	0.001
Kn in MPL	2.018	3.168	1.155	1.073

Table 4.5 – Applicability of different flow models in different flow regimes based on Knudsen number [72]

Knudsen number	Flow model
$Kn < 0.001$	Continuum region; Navier -Stokes valid with no-slip boundary condition
$0.001 < Kn < 0.1$	Continuum-transition region; Navier-Stokes valid only with slip boundary condition
$0.1 < Kn < 10$	Transition region; Navier-Stokes not valid, moment equations or Burnett equation with slip boundary condition
$Kn > 10$	Free molecule flow; No continuum model valid

The error will be even more in MPL as the molecule wall collision will become more dominant and viscous effects will start diminishing. Figure 4.7 shows the difference between observed and predicted pressure drop values across a 34BC assembly for helium flow. The difference between slopes of the curves is higher for 34BC compared to 34BA, which indicates a higher difference between actual and predicted permeability values. Helium has a higher Knudsen diffusivity than oxygen, hence the wall friction will be less. The predicted values in the plot are the one obtained by oxygen experiments. The oxygen has a lower Knudsen diffusivity, thus higher wall friction. Therefore, the pressure drop in helium experiment is less than the values predicted by oxygen experiments.

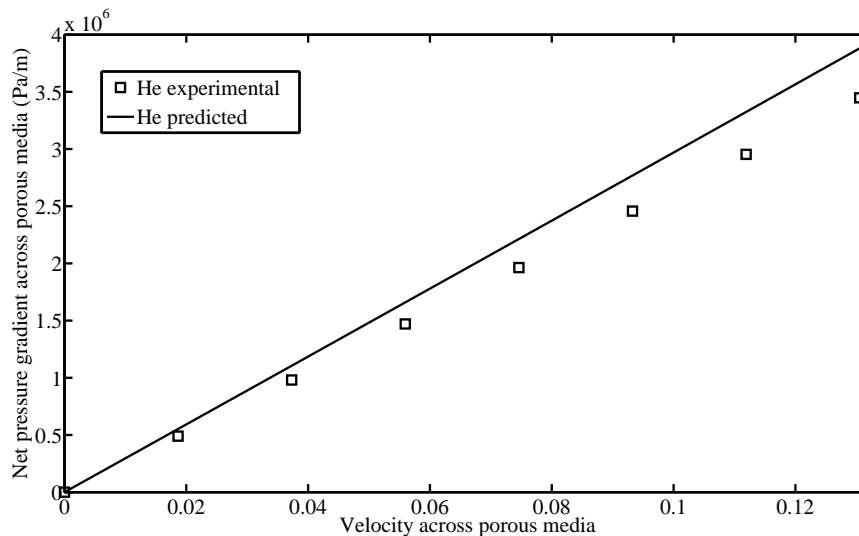


Figure 4.7 – Comparison of experimentally observed pressure drop across a SGL SIGRACET 34BC GDL-MPL assembly with Darcy-Forchheimer prediction

To reduce the error in permeability calculations, the molecule-wall interactions must also be taken into account. The modified binary friction model (MBFM), which takes into account both viscous and wall interactions can be used. The one dimensional MBFM for a single component fluid can be given as:

$$\frac{dp}{dx} = -RT \left(D_K^{eff} + \frac{B_v}{\eta/p} \right)^{-1} N \quad (4.12)$$

This equation is based on the assumption that Knudsen and viscous transports are independent and can be added in parallel. This approach has not been extensively validated. However, it provides a way to account for the wall-molecule interactions. Assuming a constant velocity across porous media and using ideal gas law ($N = cv = \frac{p}{RT}v$), the equation can be rewritten as follows:

$$\left(\frac{D_K^{eff}}{p} + \frac{B_v}{\eta} \right) dp = -v dx \quad (4.13)$$

similar equation has also been presented by [21] for combined permeability and Knudsen diffusivity estimation in porous media.

New Permeability Measurements in GDL

In case of GDL, eq. (4.13) is integrated over the length of porous media and the following expression is obtained:

$$v = \frac{D_K^{eff}}{L} \ln \left(\frac{p_1}{p_2} \right) + \frac{B_v}{\eta L} (p_1 - p_2) \quad (4.14)$$

where p_1, p_2 are the pressure values at the entrance and exit side of the porous media respectively, and L is the total thickness of GDL assembly. For the current permeability measurement setup, the gas is always exhausted to ambient pressure ($p_2 = 1 atm$). Hence the velocity is only dependent on p_1 . This equation can be fitted to experimental data for obtaining D_K^{eff} and B_v . The pressure drop is very low in GDL, therefore the Knudsen term will be almost negligible. Due to this, the associated fitting error will be very high, similar to the error in inertial permeability measurement. As Knudsen diffusion coefficient is inversely proportional to the molecular mass, D_K will be much higher for He. Also as seen in Table 4.4, the oxygen transport is in the continuum region. Hence for oxygen profile fit, Knudsen diffusivity is neglected and the Darcy's equation is recovered as follows:

$$v = \frac{B_v}{\eta L} (p_1 - p_2) \quad (4.15)$$

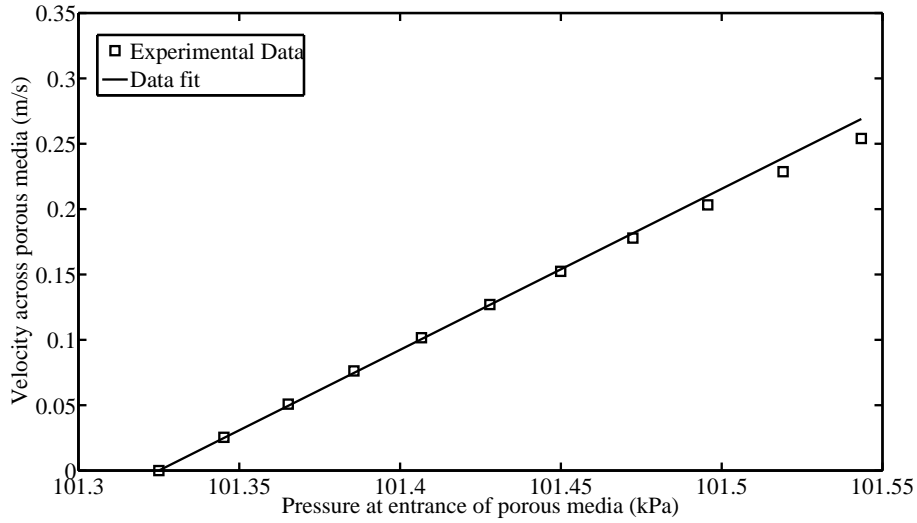


Figure 4.8 – Experimental results vs Darcy’s datafit for O_2 in a SGL SIGRACET 34BA GDL

Figure 4.8 shows the comparison of experimental observations with Darcy’s model predictions. The pressure p_1 is the fitting variable in this case, therefore it is used as the x-axis parameter. The viscous permeability of SIGRACET 34BA GDL was found be $2.586 \times 10^{-11} m^2$, with maximum error in data fit being around $\pm 5.8\%$. As the Darcy’s law is unable to incorporate the nonlinearity of the transport, the errors are slightly high compared to the earlier fit with the Darcy-Forchheimer equation.

The viscous permeability of GDL is used in the next stage of data processing. Using this value of permeability, eq. (4.14) is fitted to data obtained with helium experimentation. Figure 4.9 shows the comparison of experimental results with MBFM datafit. Again p_1 is used as the fitting variable. The Knudsen diffusivity for helium in the GDL was found to be $4.164 \times 10^{-3} m^2/s$, with maximum error in datafit being around $\pm 0.7\%$. The experimental results show excellent agreement with the trend of theoretical model. For verification, the effective pore radius can be obtained from the effective Knudsen diffusivity by eq. (3.45) as follows:

$$D_K^{eff} = \frac{\epsilon}{\tau} 0.89 \times \frac{2}{3} r_p \left(\frac{8RT}{\pi M} \right)^{1/2} \quad (4.16)$$

where the tortuosity is approximated as $\tau = 4\epsilon^{-0.5}$ [4]. The factor of four in tortuosity calculation is used to account for the overprediction by Bruggeman correlation [4]. The effective pore radius for SIGRACET 34BA ($\epsilon = 0.83$) with helium is obtained to be around $29.53 \mu m$. This values is within the range of pore size distribution

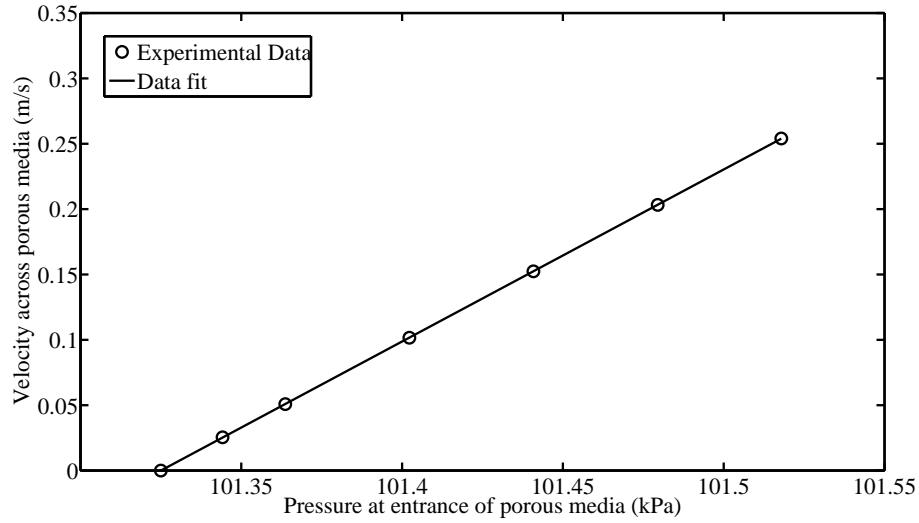


Figure 4.9 – Experimental results vs MBFM datafit for He in a SGL SIGRACET 34BA GDL

($10 - 150\mu m$) for gas diffusion layers [66, 67]. This provides a partial validation to the idea. Further validation can be done by using other gases of different molecular weights.

New Permeability Measurements in MPL

To measure permeability and Knudsen diffusivity in the MPL, again eq. (4.13) can be used. However, fitting data is not as straightforward in MPL, as the experimentation is done for a GDL-MPL assembly. Due to non-linearity of the pressure expression in eq. (4.13), separating MPL pressure drop is challenging. To start with, the GDL effects were neglected and all the pressure drop was considered to be due to the MPL. The pressure across MPL can be then fitted to eq. (4.13). Helium and oxygen flow are both in transition region for MPL, hence both Knudsen diffusivity and permeability have to be taken into account. The following results were obtained from oxygen and helium experiments datafit:

- $D_K^{He} = 1.237 \times 10^{-12} m^2/s$ $B_v = 3.092 \times 10^{-13} m^2$
- $D_K^{O_2} = 1.189 \times 10^{-12} m^2/s$ $B_v = 2.973 \times 10^{-13} m^2$

The Knudsen diffusivity is directly proportional to pore radius. However, the Knudsen diffusivity in the MPL is almost nine orders of magnitude less than in GDL. Therefore there is problem with the assumption of neglecting GDL effects.

To correct for this error, the GDL effects must also be taken into account. A linear equation for pressure drop is helpful in separating effects of individual layers, similar to the Darcy-Forchheimer equation. For a single layer porous media, eq. (4.13) can be rewritten as follows:

$$\frac{D_{K,i}^{eff}}{L_i} \ln \left(\frac{p_i}{p_{i+1}} \right) + \frac{B_{v,i}}{\eta} \left(\frac{p_i - p_{i+1}}{L_i} \right) = v = \frac{D_{K,i}^{eff}}{L_i} \ln \left(1 + \frac{\Delta p_i}{p_{i+1}} \right) + \frac{B_{v,i}}{\eta} \frac{\Delta p_i}{L_i} \quad (4.17)$$

where p_i and p_{i+1} are pressures at the entrance and exit of the i^{th} porous layer respectively, and Δp_i is the pressure drop in i^{th} layer. For current permeability experiments in porous media, the maximum pressure drop is around 2500 Pa ($\Delta p_i|_{max} \simeq 2500 Pa$) and the exit pressure can be assumed to be equal to atmospheric pressure ($p_{i+1} \simeq 1 \times 10^5 Pa$). In this case $\frac{\Delta p_i}{p_{i+1}} \ll 1$, so the logarithmic term can be expanded as a Taylor series:

$$\frac{D_{K,i}^{eff}}{L_i} \left[\left(\frac{\Delta p_i}{p_{i+1}} \right) + O \left(\frac{\Delta p_i}{p_{i+1}} \right)^2 \right] + \frac{B_{v,i}}{\eta} \frac{\Delta p_i}{L_i} = v \quad (4.18)$$

The higher order terms can be neglected as $\frac{\Delta p_i}{p_{i+1}} \simeq O(10^{-2}) \ll 1$. The exhaust pressure p_{i+1} can be assumed to be equal to atmospheric pressure everywhere as the variation is negligible compared to its absolute value. For a single layer, the simplified equation can be given as follows

$$K_i \frac{\Delta p_i}{L_i} = v \quad (4.19)$$

where K_i is the friction coefficient for a single layer, which is given as:

$$K_i = \left(\frac{D_{K,i}^{eff}}{p_{atm}} + \frac{B_{v,i}}{\eta} \right) \quad (4.20)$$

For an entire GDL-MPL assembly, an effective friction coefficient can be obtained as follows:

$$K_{eff} = v \frac{L}{\Delta p} \quad (4.21)$$

where L is the total thickness of the GDL-MPL assembly and Δp is net pressure drop across the assembly. Following a similar approach as given in section 4.1, the individual constant K_i values for GDL and MPL can be related to the effective parameter K_{eff} as follows:

$$K^{MPL} = L_{MPL} \left(\frac{L}{K_{eff}} - \frac{L_{GDL}}{K_{GDL}} \right)^{-1} \quad (4.22)$$

The experimental data on SIGRACET 34BC GDL-MPL assembly was fitted to eq. (4.19) for the effective parameter. Figure 4.10 shows the experimental data and

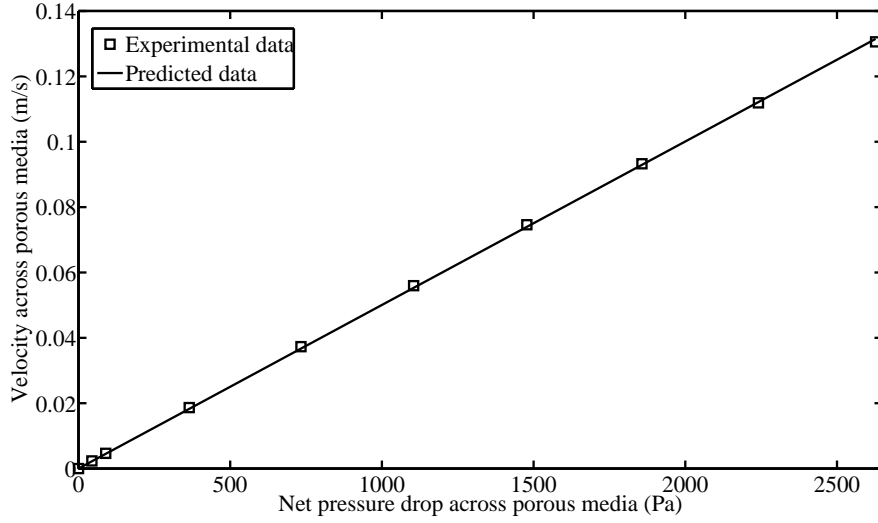


Figure 4.10 – Comparison of experimental data to a linear datafit for a SIGRACET 34BC assembly with O_2

corresponding data fit for a SGL SIGRACET 34BC assembly with oxygen. The maximum error in data fit was observed to be around $\pm 5\%$. Similar results were observed in helium experiments as well. These two experiments provided two effective friction coefficients in the GDL-MPL assembly, from which the MPL coefficient is separated using eq. (4.22). The two MPL coefficients have to be then solved to separate Knudsen diffusivity and permeability. The two equations can be written as follows:

$$\frac{D_{K,He}^{eff}}{p_{atm}} + \frac{1}{\eta_{He}} B_v = K_{He} \quad (4.23)$$

$$\frac{D_{K,O_2}^{eff}}{p_{atm}} + \frac{1}{\eta_{O_2}} B_v = K_{O_2} \quad (4.24)$$

where $D_K^{eff} = f(T, M, \epsilon, \tau, r_p)$, amongst which T, M & ϵ are known and τ & r_p are unknowns. Replacing D_K^{eff} by eq. (4.16), the following system of linear equations is obtained

$$\frac{1}{p_{atm}} 0.89 \times \frac{2}{3} \left(\frac{8RT}{\pi M_{He}} \right)^{1/2} \frac{\epsilon r_p}{\tau} + \frac{1}{\eta_{He}} B_v = K_{He} \quad (4.25)$$

$$\frac{1}{p_{atm}} 0.89 \times \frac{2}{3} \left(\frac{8RT}{\pi M_{O_2}} \right)^{1/2} \frac{\epsilon r_p}{\tau} + \frac{1}{\eta_{O_2}} B_v = K_{O_2} \quad (4.26)$$

These two linear equations can be solved to obtain $\frac{\epsilon r_p}{\tau}$ and B_v . Which can be then used to calculate D_K^{eff} and B_v . Table 4.6 shows the permeability and Knudsen diffusivity in GDL and MPL of a SIGRACET 34BC porous media obtained using the

Table 4.6 – Permeability and Knudsen diffusivity values in PEM fuel cell porous media

Parameter	in GDL	in MPL
Viscous permeability, B_v (m^2)	2.586×10^{-11}	1.187×10^{-13}
Knudsen diffusivity (He), $D_{K,He}^{eff}$ (m^2/s)	4.164×10^{-3}	1.646×10^{-4}
Knudsen diffusivity (O_2), D_{K,O_2}^{eff} (m^2/s)	1.472×10^{-3}	5.820×10^{-5}

MBFM approach. The permeability values are slightly smaller than the ones obtained by Darcy-Forchheimer equation (see table 4.3), due to accounting for Knudsen flow. The Knudsen diffusivity values in MPL are around two orders of magnitude less than in GDL, which is in the acceptable range. The use of MBFM helped in accounting for the Knudsen transport through nano pores of the porous media and in turn helped in reducing the error in transport properties estimation.

For validation of Knudsen diffusivity in MPL, the effective pore radius can be calculated using eq. (4.16). The tortuosity is again assumed as $\tau = 4\epsilon^{-0.5}$ [4]. For a SIGRACET 34BC MPL ($\epsilon = 0.422$) the effective pore radius was found to be around $3200nm$. The calculated value is not within the range of pore size distribution in MPL[67, 71]. This can be attributed to the linear assumptions in the derivation, uncertainties in the pore radius and porosity. At nano length scales, other phenomena like surface transport can also come into picture which also contributes to the error. Also, there are crack formations in the MPL, which can increase the net flux and hence introduce error in computation.

4.1.4 Permeability and Knudsen Diffusivity Validation

To validate the applicability of modified binary friction model (MBFM), a new experiment was carried out. The experimentation was done on the SIGRACET 34BC GDL-MPL assembly by using nitrogen (N_2) as the working fluid. The pressure drop across the GDL-MPL assembly is estimated by using eq. (4.19), where all the permeability and Knudsen diffusivity values are already known. Figure 4.11 shows the comparison of experimental and theoretical predictions of pressure gradient across the porous assembly. The difference between the experimental and theoretical results for nitrogen was found to be around $\pm 3\%$. The pressure gradient profile for nitrogen lies in between the oxygen and helium profile as expected. It can be seen that the MBFM predicts the flow in porous media with better accuracy than Darcy-Forchheimer equation. This analysis shows that the Knudsen transport is significant in fuel cell porous media, and must be taken into account for accurate predictions.

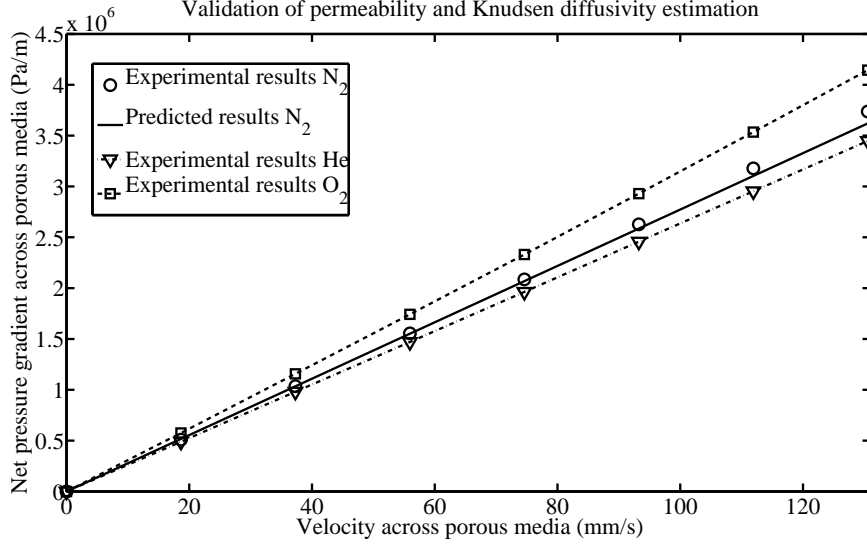


Figure 4.11 – Comparison of experimental and MBFM predictions for flow across porous media

4.1.5 Sensitivity Analysis of Permeability Results

The permeability and Knudsen diffusivity estimation depends on measurement of several variables. During post-processing, any error in the measurement of the primary variables will have a direct impact on the accuracy of parameter estimation. The permeability and Knudsen diffusivity can be given as function of the primary variables as follows:

$$B_v = f(\Delta p, \dot{Q}, L, d, \epsilon) \quad (4.27)$$

$$D_K = f(\Delta p, \dot{Q}, L, d, \epsilon) \quad (4.28)$$

where Δp is the pressure drop recorded by transducer, \dot{Q} is the flow rate measured by flow controller, L is the thickness of porous media measured by a micrometer, d is the diameter of the aperture measured by a surface profilometer and ϵ is the porosity taken from SIGRACET catalogue.

The error associated with flow rate, pressure drop and diameter is instrumental and is given by the instrument's accuracy as discussed in section 2.2.1. The error associated with thickness and porosity is not only based on the instrument but also on the measurement process. The thickness and porosity of the porous media can change significantly during the measurement due to compression. Especially in the GDL, the error can be very high due to its highly porous and compressible nature. The MPL even though not compressible; is susceptible to errors in GDL measurement, as the

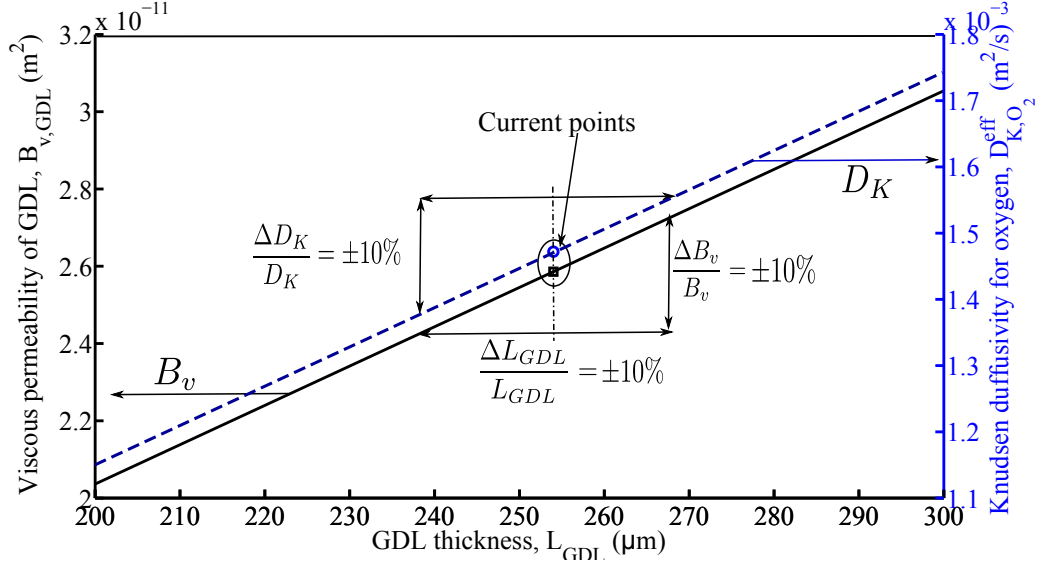


Figure 4.12 – Sensitivity of GDL permeability and Knudsen diffusivity of oxygen with respect to GDL thickness

MPL properties are obtained by separating GDL measurements from the GDL-MPL assembly.

The equation for GDL permeability estimation is given as follows:

$$v = \frac{D_K^{eff}}{L} \ln \left(\frac{p_1}{p_2} \right) + \frac{B_v}{\eta L} (p_1 - p_2) \quad (4.29)$$

where p_1, p_2, η and v are fixed for a given experimental data set. In other words, the profile shape of v vs p_1 is fixed, hence the coefficients D_K^{eff}/L and $B_v/\eta L$ have to be constant. The change in permeability and Knudsen number can be given as a function of change in GDL thickness for a given experiment as follows:

$$\Delta B_{v,GDL} = A \times \Delta L_{GDL} \quad (4.30)$$

$$\Delta D_{K,GDL}^{eff} = B \times \Delta L_{GDL} \quad (4.31)$$

where A and B are constants obtained with initial values of L_{GDL} and $B_{v,GDL}$. It can be concluded from eq. (4.30) and (4.31) that the relative error in permeability and Knudsen diffusivity measurement in GDL will be equal to the relative error in GDL thickness measurement as shown in Fig. 4.12. During datafit, the effective Knudsen diffusivity in the GDL is estimated as single parameter from eq. (4.14). Therefore the porosity measurement error does not affect the Knudsen diffusivity estimation.

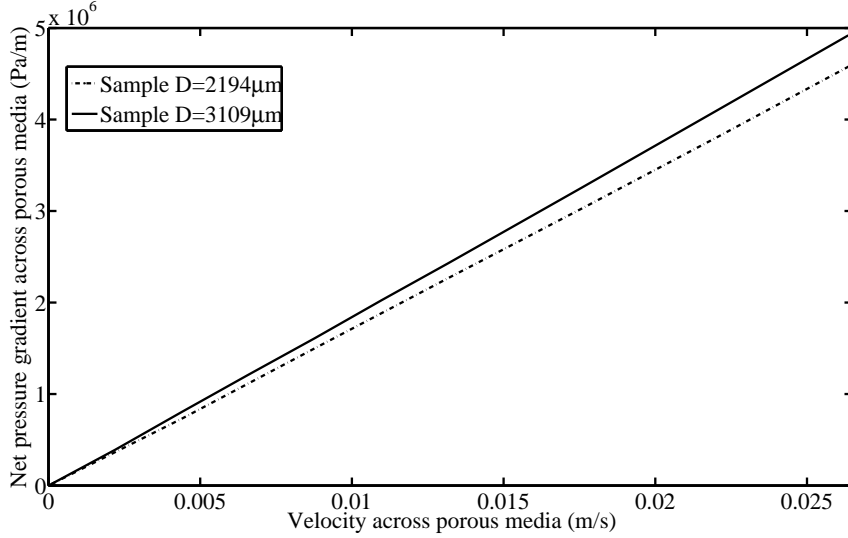


Figure 4.13 – Comparison of pressure drop vs velocity profile for two samples of SIGRACET 24BC with different cross sections

To estimate the MPL permeability and Knudsen diffusivity, the following equation is used:

$$K^{MPL} = L_{MPL} \left(\frac{L}{K_{eff}} - \frac{L_{GDL}}{K_{GDL}} \right)^{-1} \quad (4.32)$$

where $\frac{L}{K_{eff}}$ can be given as follows from eq. (4.21):

$$\frac{L}{K_{eff}} = \frac{\Delta p}{v} \quad (4.33)$$

where Δp and v will be constant for given experimental data set. Similarly $\frac{L_{GDL}}{K_{GDL}}$ is a constant for given data set as the GDL permeability is already calculated. In this case the MPL friction parameter K^{MPL} is proportional to the MPL thickness:

$$\Delta K^{MPL} = C \times \Delta L_{MPL} \quad (4.34)$$

where C is a constant. Equations (4.25) and (4.26) for permeability and Knudsen diffusivity are linearly dependent on K^{MPL} . Therefore the permeability and Knudsen diffusivity will be directly proportional to MPL thickness. The relative error in MPL permeability and diffusivity will be equal to the relative error in MPL thickness measurement.

To find the sensitivity of permeability values with respect to the aperture cross section area, two samples of SIGRACET 24BC were tested with different cross sections. Figure 4.13 shows the comparison of pressure drop vs velocity profiles for both

the samples. The difference between the permeability values for the samples was found to be around $\pm 6.93\%$, which is within the uncertainty range for different samples. In other words, the difference in permeability can be attributed to the variation in porous media properties between different samples, as discussed earlier in section 4.1.2.

4.2 Diffusivity Measurements in Porous Media

This section describes the measurement of diffusion coefficients in porous media by mass transport experiments. The experimental setup used to obtain the data is described in section 2.1.1. Oxygen flux is measured as function of net pressure gradient across porous media. The experimental data is then fitted to the mass transport models presented in chapter 3.

The mass transport models have three unknown parameters; Knudsen number, viscous permeability and effective diffusivity, which need to be known for numerical modelling. The permeability and Knudsen number have already been calculated in section 4.1.3. This section focuses on determining effective diffusivity in porous media. Figure 4.14 shows the comparison of experimental and numerical results, where the effective diffusivity is calculated by Bruggeman correlation. It can be seen that the Bruggeman correlation overpredicts mass transport by 3-4 times, hence experimental measurements of effective diffusivity are necessary.

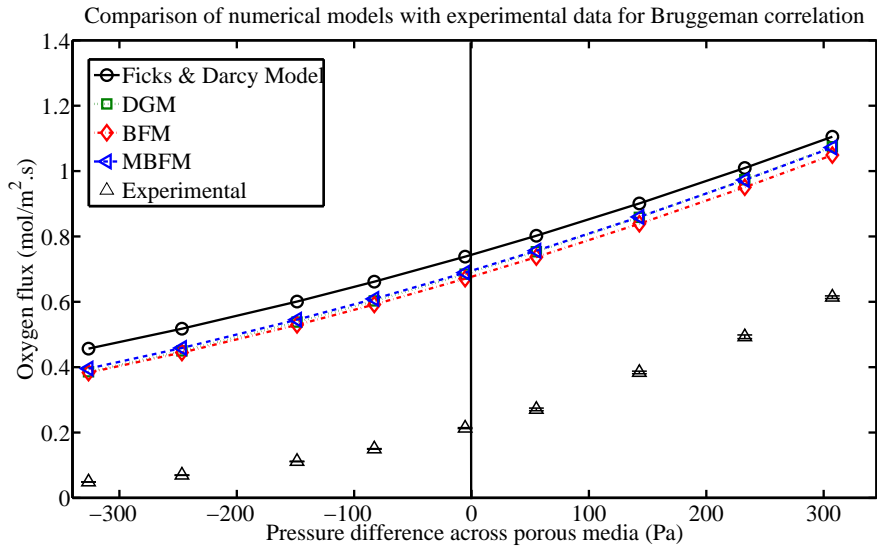


Figure 4.14 – Comparison of experimental flux measurements with numerical predictions using Bruggeman correlation

4.2.1 Diffusivity Measurements in Gas Diffusion Layers

The porous media used in PEM fuel cells is a gas diffusion layer coated with micro porous layer. SIGRACET 34 GDL-MPL assembly was used for experimentation. To understand the effects of both layers independently, effective diffusivity in both layers must be known separately.

The experimental setup was designed for low flow rates in the flow channels. As discussed in section 2.1.1, the flow rate in channels should be much higher than flow through porous media to avoid boundary layer formation. However, due to high permeability of gas diffusion layers, the flow across them is quite high and the boundary layer effects can not be ignored. Further, this high amount of incoming oxygen flux was not within micro-GC detection limits. Replacing the flow controllers and analyzing equipment was not possible within the time frame. Therefore, the effective diffusivity in gas diffusion layer was taken from literature. Several researchers have estimated effective diffusivity values in gas diffusion layers [4, 30, 35–37]. All of the researchers have reported similar results for gas diffusion layers. As per their observations, the over-prediction by Bruggeman correlation is on an average three times for porous media with porosity values around 80% (Similar to 34BA). Taking this into account the effective diffusivity in GDL has been assumed as follows:

$$D_{O_2N_2,GDL}^{eff} = \frac{1}{3}D_{O_2N_2}\epsilon^{1.5} \quad (4.35)$$

For the current case of experimentation with oxygen and nitrogen at 28°C, the effective diffusivity in GDL is around $4.8953 \times 10^{-6} m^2/s$.

4.2.2 Diffusivity Measurements in Micro Porous Layers

Once the GDL effective diffusivity is fixed, the only unknown parameter remaining is the effective diffusivity in the MPL. The MPL effective diffusivity can be used as a fitting parameter to fit the mass transport models to experimental data. The effective diffusivity directly depends on the tortuosity of the porous media, hence the tortuosity has been used as a fitting parameter. For datafit, a least square approach has been used. The following residual function is minimized by changing the tortuosity of the MPL:

$$R = \sum_{k=1}^n (N_k^{model} - N_k^{exp})^2 \quad (4.36)$$

where N_k^{model} is the flux predicted by the model at Δp_k pressure difference, and N_k^{exp} is the flux observed by experimentation at the same pressure difference. The difference

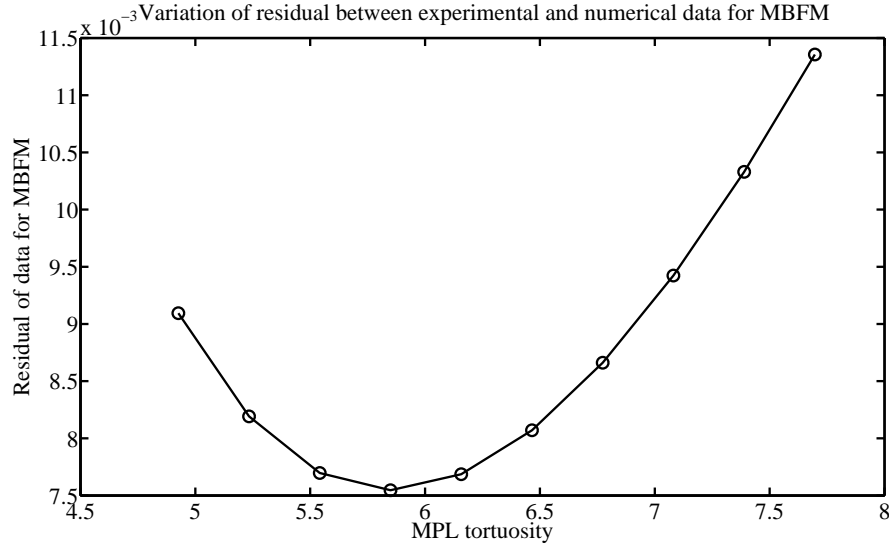


Figure 4.15 – Variation of the residual with tortuosity for the least square method

square is summed over all sample points and the net residual is minimized for best datafit. Figure 4.15 shows the variation of residual for different tortuosity values used in MBFM. The tortuosity at minimum residual point is taken for the best fit, and the experimental and numerical results are compared. Similarly the best fitting tortuosity values were found for other mass transport models. Then the following equation is used to calculate effective diffusivity, which is then used in numerical models to obtain the best fitting flux profile:

$$D_{O_2N_2}^{eff} = \frac{\epsilon}{\tau} D_{O_2N_2} \quad (4.37)$$

Figure 4.16 shows the comparison of experimental results with numerical results for the best fit value of MPL tortuosity. It can be seen that the trends predicted by mass transport models are matching very well with the experimental results. The margin of error shown on the experimental results was calculated for a 95% confidence interval. It can be seen that the margin of error is almost negligible in the experimental results, so the data is reliable. The maximum difference between experimental and numerical results was around $\pm 8\%$. Earlier in chapter 3 in Fig. 3.22, it was shown that the predictions by different mass transport models were not matching. In that case all the models were solved for same transport parameters. However in this case, each model has been individually fitted to the experimental data. Therefore, the best fitting numerical results are at different tortuosities for different models. This explains why all the models are almost exactly matching.

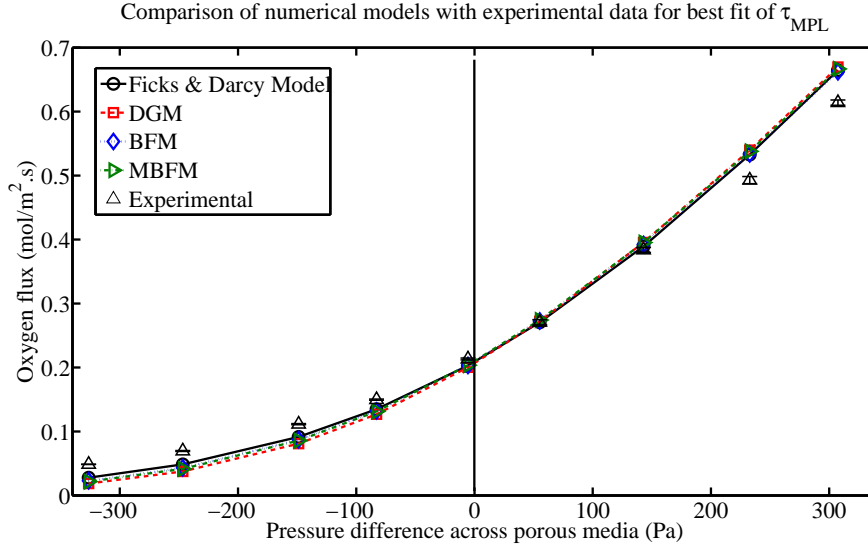


Figure 4.16 – Comparison of experimental and best fitting numerical results of mass transport, using MPL tortuosity as fitting parameter

Table 4.7 – Effective diffusivity values in MPL for the best fit of different mass transport models

Model	Effective diffusivity in MPL, D^{eff} (m^2/s)
Bruggeman correlation	5.3242×10^{-6}
Best fit of Fick's and Darcy's law	1.2101×10^{-6}
Best fit of binary friction model (BFM)	1.4389×10^{-6}
Best fit of modified binary friction model (MBFM)	1.3651×10^{-6}
Best fit of dusty gas model (DGM)	1.2676×10^{-6}

Table 4.7 shows the values of effective diffusivity used in different mass transport models for the best fit. The diffusivity value predicted by Bruggeman correlation is also shown. It can be seen that the correlation overpredicts the diffusivity by around 3.5–4.5 times. Similar observations have been made by other researchers as well [4, 30, 35–37].

4.2.3 Diffusivity Estimation Validation

To validate the findings, a new mass transport experiment was carried out. Instead of pure oxygen diffusing in pure nitrogen, a mixture of oxygen and nitrogen (10% O_2) was allowed to diffuse into a pure nitrogen stream and the mass transport was observed. Figure 4.17 shows the comparison of the new experimental results with the numerical results. The numerical model uses the diffusivity values predicted with

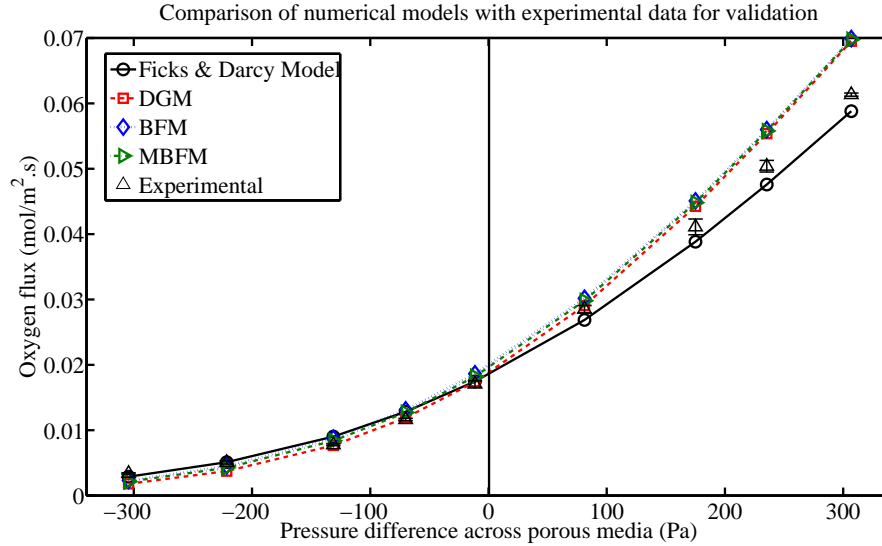


Figure 4.17 – Comparison of experimental and numerical results for validation of MPL tortuosity calculations

pure O_2 experiments for calculations, as shown in Table 4.7. The maximum difference between the experimental results and numerical results was found to be around $\pm 13\%$. The numerical results agree well with experimental values, validating the diffusivity calculations. The values of MPL diffusivity shown in Table 4.7 can be now used for further calculations and numerical modelling of mass transport in MPL.

It can be seen that all the theoretical models predict the mass transport quite accurately, as long as their corresponding best fitting tortuosity value is used. In this case the results shows excellent agreement even after changing the composition of the gases. It suggests that all the models are correctly accounting for the dominant forces in fuel cell porous media, hence the trends are matching. Similar findings have also been presented by Vural et al. [27] and Tseronis et al. [74] in their study of mass transport in solid oxide fuel cells. They concluded that in the operation range of fuel cells, all the models were able to predict the mass transport trends accurately. Extensive validations is needed to confirm the reliability and accuracy of all the models. Different types of porous media have to be tested with several gases, to separate and analyze all the forces.

Table 4.8 shows the values of all the geometric and transport parameters for a SIGRACET 34BC GDL-MPL assembly. These parameters are sufficient to model mass transport in porous media with modified binary friction model (MBFM) while

Table 4.8 – Geometric and transport parameters of GDL and MPL estimated from the experiments in a SIGRACET 34BC porous media

Parameter	GDL Value	MPL Value
Thickness, L (μm)	254	32.5
Porosity, ϵ	0.83	0.422
Permeability, B_v (m^2)	2.586×10^{-11}	1.487×10^{-13}
Knudsen diffusivity of O_2 , D_{K,O_2}^{eff} (m^2/s)	1.472×10^{-3}	5.82×10^{-5}
Molecular diffusivity, $D_{O_2N_2}^{eff}$ (m^2/s)	4.8953×10^{-6}	1.3651×10^{-6}

accounting for all the physical processes of convection, molecular diffusion and wall interactions.

4.2.4 Sensitivity Analysis of Diffusivity Results

The diffusivity values in GDL and MPL are found by fitting the flux vs pressure drop profile. The profile depends upon the measurement of several primary variables. Therefore the MPL diffusivity can be presented as:

$$D_{ij,MPL}^{eff} = f(A, \Delta p, \epsilon_{MPL}, D_{ij,GDL}^{eff}, L_{MPL}) \quad (4.38)$$

where A is the area count measured by micro-GC, Δp is the pressure drop across porous media measured by the pressure transducer, ϵ_{MPL} is the MPL porosity obtained from SIGRACET catalogue, $D_{ij,GDL}^{eff}$ is the GDL diffusivity predicted in section 4.2.1 and L_{MPL} is the MPL thickness. The diffusivity also depends upon the porosity and thickness of GDL as well, however these variables are already accounted for in estimation of $D_{ij,GDL}^{eff}$. Any error in measurement of these variables will directly affect the accuracy of MPL diffusivity estimation.

The measurement error in A and Δp is only instrumental, which can be quantified by the accuracy of the equipment as discussed in section 2.1.8. The error in MPL thickness and porosity measurement is dependent upon the measurement process. The compression of the porous media can significantly change the thickness and porosity values. The GDL diffusivity has been approximated in section 4.2.1, the approximated values will have a direct impact on estimation of MPL diffusivity.

Figure 4.18 shows the variation in MPL diffusivity with respect to the GDL diffusivity. The variation is not linear and tends to saturate for increasing values of GDL diffusivity. Due to the non-linear variations, the measurement error will change depending on the location of its evaluation. In a MBFM data fitting near current

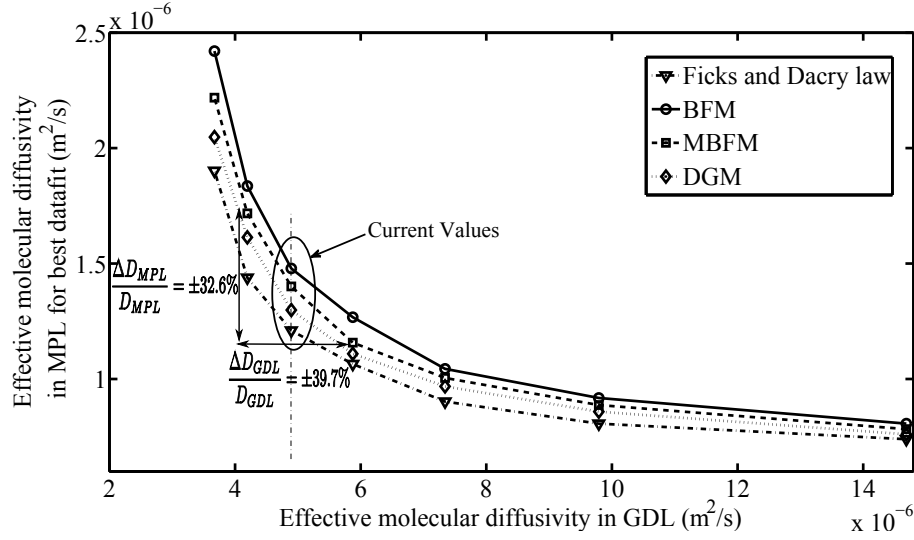


Figure 4.18 – Sensitivity of MPL diffusivity with respect to GDL diffusivity

values, an error of $\pm 39.7\%$ in GDL diffusivity estimation results in an error of $\pm 32.6\%$ in MPL diffusivity. The errors in the MPL diffusivity is almost equal to the error in GDL diffusivity, therefore the GDL diffusivity has to be measured with high accuracy.

To understand the effect of MPL porosity, one must look at the governing equations presented in section 3.2.5. The porosity is only used in effective diffusivity calculations. For a given experimental data set, the flux vs pressure drop profile is a constant. As the MPL diffusivity is a profile controlling parameter, it must also remain constant. Therefore, the porosity measurement error has no effect on effective diffusivity estimations. However, the MPL tortuosity will change while changing the MPL porosity. To keep effective diffusivity constant, the ratio $\frac{\epsilon}{\tau}$ must remain constant in MPL, therefore the error in tortuosity estimation will be equal to the error in porosity estimation.

To find the sensitivity of the MPL diffusivity with respect to MPL thickness, the MPL thickness was changed to $50\mu m$ from the original value of $62.5\mu m$. The corresponding value of MPL diffusivity for best fit of data changed from $1.3651 \times 10^{-6} m^2/s$ to $8.7283 \times 10^{-7} m^2/s$. In other words; for a 20% change in MPL thickness, the corresponding change in MPL diffusivity was found to be around 36%. Figure 4.19 shows the best fit of numerical models with experimental data for a MPL thickness of $50\mu m$. Not only the MPL diffusivity is most sensitive to MPL thickness, but also the trends of the flux profile do not match properly, decreasing the reliability of the datafit. Therefore the measurement of MPL thickness should be done with highest

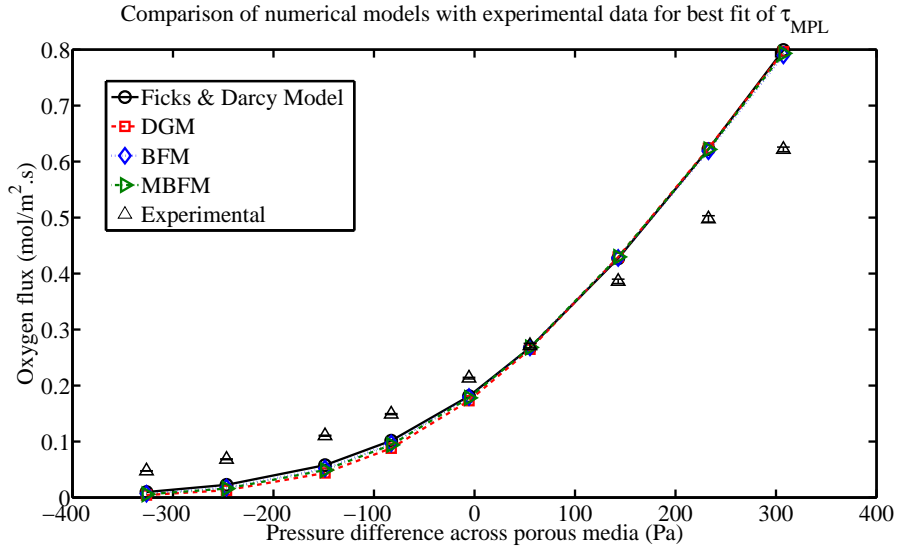


Figure 4.19 – The comparison of best fitting numerical results with experimental results of mass transport, for an MPL thickness of $50\mu m$

accuracy and reliability. It is suggested that the MPL thickness should be measured by measuring the cross section of GDL-MPL assembly on a scanning electron microscope (SEM).

Chapter 5

Conclusion and Future Work

5.1 Conclusion

The aim of this research was to develop an experimental setup to predict convective-diffusive mass transport in fuel cell porous media. In order to achieve this goal, a diffusion bridge setup has been build and tested for reliability. The experimental setup has been used to obtain species fluxes as a function of pressure difference across porous media. In order to analyze the experimental data, several mass transport theories have been studied. Based on the shortcoming of the previous models, a new theoretical model, namely the modified binary friction model (MBFM) based on irreversible thermodynamic approach of Lightfoot equation was proposed. The model is based on balancing of all the driving forces and frictional forces acting in porous media. The final model is a modification of binary friction model proposed by Kerkhof [26] in the pretext of eliminating all assumptions of BFM. The theoretical model takes into account viscous friction, wall collisions and interspecies interactions. The only assumption in the model is that the Knudsen transport and viscous transport are independent of each other and can be added in parallel. The new model was compared with the conventional models like Fick's and Darcy's model and dusty gas model (DGM). It has been shown that the Ficks and Darcy's model is inaccurate for highly convective flows and also for flow in micro-nano pores due to absence of wall collision terms. The dusty gas model was also found to be incorrect for pure diffusion and moderate convection-diffusion situations.

The experimental setup used for mass transport studies was designed as a diffusion bridge to facilitate both; pure diffusion and convection diffusion studies. The experimental study of mass transport in GDL and MPL has two main parts: a) Permeability analysis on porous media; b) Diffusivity analysis on porous media. The permeability

of the porous media was initially obtained by conventional Darcy-Forchheimer equation. The permeability values for the SIGRACET 34BA GDL and SIGRACET 34BC MPL were found to be $2.91 \times 10^{-11} m^2$ and $7.14 \times 10^{-13} m^2$ respectively using oxygen as the working fluid. The permeability values were found to be within the range of reported data in the literature. By performing further experiments with helium, it was shown that the Darcy's approach is not valid for small pore sizes in the MPL due to migration from the continuum regime. A new technique based on MBFM was proposed to predict not only permeability of the porous media, but also the effective Knudsen diffusivity. Based on the new approach, the permeability values in GDL and MPL were found to be $2.586 \times 10^{-11} m^2$ and $1.487 \times 10^{-13} m^2$ respectively. The effective Knudsen diffusivity values for oxygen were found to be $1.472 \times 10^{-3} m^2/s$ and $5.82 \times 10^{-5} m^2/s$ for GDL and MPL respectively.

The MPL diffusivity was measured by fitting the experimental data with theoretical models using a least square fit. The effective diffusivity of oxygen-nitrogen in MPL with a best fit to MBFM was found to be around $1.3654 \times 10^{-6} m^2/s$. The experimental results suggest that conventional correlations like Bruggeman equation overpredict the diffusivity in MPLs by as much as four times. Similar finding have been reported in literature for GDLs by Zamel et al. [4], Lamanna and Kandlikar [30], Fluckiger et al. [35], Baker et al. [36], Kramer et al. [37]. The diffusivity measurements on GDLs could not be performed successfully due to very high permeability. Due to the high permeability of GDL, the transport across porous media was high enough to create a thick boundary layer in the flow channels, which was a challenge for modelling. The only way of avoiding the boundary layer is to install higher capacity flow controllers in the flow channels and a new oxygen detector. This was not possible within the time frame of this research, therefore the GDL diffusivity values were taken from literature.

To validate the estimated transport properties, a new experimental study was carried out. The experimental results were found to be within $\pm 13\%$ of the values predicted by numerical models using the earlier found effective diffusivity. For the operating parameter range used in current experiment, all the models were found to be accurately predicting the mass transport. Earlier Vural et al. [27] and Tseronis et al. [74] have also confirmed the validity of these models in solid oxide fuel cell porous media.

In summary, this thesis presents:

- Development of a new experimental setup based on diffusion bridge to measure pure diffusion, pure convection and convection-diffusion.
- Development of a methodology to extract data from the experimental setup.
- Development of a new mass transport model, which includes all the interactions
- A new technique to estimate permeability and Knudsen diffusivity in porous media, using the newly derived mass transport model.
- Mass transport measurements in porous media and effective diffusivity estimation using the mass transport models.
- Conclusive evidence of underprediction of mass transport limitations in porous media by Bruggeman correlation.
- Preliminary evidence of accuracy of all mass transport models.

5.2 Future Work

This thesis has only focused on diffusivity measurements in MPLs due to technical difficulties in the current setup. It was found that the MPL diffusivity estimation is sensitive to the GDL diffusivity assumptions. Therefore, the priority of the research will be to modify the current experimental setup to perform mass transport studies on GDLs. To avoid the boundary layer formation in the flow channels, new flow controllers with flow range of 0-5 L/min will be installed. The high flow rate in flow channels will reduce the boundary layer thickness to a negligible value. A new gas detection equipment will be used for detecting the high flow rates of oxygen through GDL.

In the current research, all the mass transport models were found to be accurate predicting the mass transport with corresponding best fit tortuosity values. However, the tortuosity is a physical parameter, which has to be constant for a porous media. In that case, only one of the models will be able to predict the mass transport better than others. To test the validity of the models, further experimentation will be done using different porous media and different gases. By changing the porous media, thickness and gases, different forces will be less or more dominant. This will

be helpful in finding the model which predicts the mass transport most accurately.

The current research has focused on binary transport in porous media. To simulate the exact conditions of a PEMFC electrode, a ternary transport has to be studied with oxygen, nitrogen and water vapours. In future experiments, a humidifier will be installed with the setup which will mix the water vapours in the flow channels and a relative humidity sensor will detect the water vapour composition at the outlet stream. The multicomponent studies will also be performed with different composition of gases to understand the behaviour of each component in the mixture.

An extensive data reliability analysis will also be performed to see the effect of aperture diameter, number of porous layers in the assembly and sample variation. The experimental study will be performed for different GDLs and MPLs with varying thickness, porosity, microstructure and PTFE content to understand the effect of each parameter on mass transport. The current experimental results will also be validated by performing experimentation with different gases like argon and neon.

In this work, the mass transport studies were performed on a SGL SIGRACET porous media which are made from carbon fibers. In a PEM fuel cell several other kind of porous media can be used such as: carbon-cloth and carbon-filled porous media. All of these porous media have a different microstructure. Therefore, an extensive study will be done by using different types of porous media to understand the effect of material and microstructure on mass transport.

References

- [1] Wishart J, Dong Z, and Secanell M. Optimization of a PEM fuel cell system for low-speed hybrid electric vehicles. In *ASME 2006 International Design Engineering Technical Conferences & Computers and Information in Engineering Conference*, Philadelphia, Pennsylvania, USA, September 10-13, 2006.
- [2] BBC News . Fuel cells in laptops edge closer, 2006. URL <http://news.bbc.co.uk/2/hi/technology/5016984.stm>. Taken on April 20, 2011, 5.10 PM.
- [3] Wagner F, Lakshmanan B, and Mathias M. Electrochemistry and the future of the automobile. *Journal of Physical Chemistry Letters*, 1(14):2204–2219, 2010.
- [4] Zamel N, Astrath N, Li X, Shen J, Zhou J, Astrath F, Wang H, and Liu Z.-S. Experimental measurements of effective diffusion coefficient of oxygen-nitrogen mixture in PEM fuel cell diffusion media. *Chemical Engineering Science*, 65(2): 931–937, 2010.
- [5] Li X and Sabir I. Review of bipolar plates in PEM fuel cells: Flow-field designs. *International Journal of Hydrogen Energy*, 30(4):359–371, 2005.
- [6] Chen-Yang Y, Hung T, Huang J, and Yang F. Novel single-layer gas diffusion layer based on PTFE/carbon black composite for proton exchange membrane fuel cell. *Journal of Power Sources*, 173(1):183–188, 2007.
- [7] Giorgi L, Antolini E, Pozio A, and Passalacqua E. Influence of the PTFE content in the diffusion layer of low-Pt loading electrodes for polymer electrolyte fuel cells. *Electrochimica Acta*, 43(24):3675–3680, 1998.
- [8] Wilson M and Gottesfeld S. Thin-film catalyst layers for polymer electrolyte fuel cell electrodes. *Journal of Applied Electrochemistry*, 22(1):1–7, 1992.

- [9] Siegel N, Ellis M, Nelson D, and Von Spakovsky M. Single domain PEMFC model based on agglomerate catalyst geometry. *Journal of Power Sources*, 115 (1):81–89, 2003.
- [10] Larminie J and Dicks A. *Fuel Cell Systems Explained*. Wiley, West Sussex, England, 2 edition, 2003.
- [11] Kandlikar S and Lu Z. Fundamental research needs in combined water and thermal management within a proton exchange membrane fuel cell stack under normal and cold-start conditions. *Journal of Fuel Cell Science and Technology*, 6 (4):0440011–04400113, 2009.
- [12] Hayre R. O, Cha S. W, Colella W, and Prinz F. B. *Fuel Cell Fundamentals*. Wiley, New York, USA, 2 edition, 2008.
- [13] Bernardi D. M and Verbrugge M. W. Mathematical model of a gas diffusion electrode bonded to a polymer electrolyte. *AIChE Journal*, 37(8):1151–1163, 1991.
- [14] Bernardi D. M and Verbrugge M. W. Mathematical model of the solid-polymer-electrolyte fuel cell. *Journal of the Electrochemical Society*, 139(9):2477–2491, 1992.
- [15] Taylor R and Krishna R. *Multicomponent Mass Transfer*. Wiley, 1993.
- [16] Krishna R and Wesselingh J. A. The Maxwell-Stefan approach to mass transfer. *Chemical Engineering Science*, 52(6):861–911, 1997. ISSN 0009-2509.
- [17] Mason E. A and Malinauskas A. P. *Gas Transport in Porous Media: The Dusty Gas Model*. Elsevier, Amsterdam, 1983.
- [18] Whitaker S. Flow in porous media I: A theoretical derivation of Darcy’s law. *Transport in Porous Media*, 1(1):3–25, 1986.
- [19] Bird R. B, Stewart W. E, and Lightfoot E. N. *Transport Phenomena*. Wiley, New York, 2 edition, 2002.
- [20] Fick A. Ueber diffusion. *Annalen der Physik*, 170(1):59–86, 1855. ISSN 1521-3889.
- [21] Kast W and Hohenthanner C.-R. Mass transfer within the gas-phase of porous media. *International Journal of Heat and Mass Transfer*, 43(5):807–823, 2000.

- [22] Kerkhof P and Geboers M. Toward a unified theory of isotropic molecular transport phenomena. *AIChE Journal*, 51(1):79–121, 2005.
- [23] Salcedo-Diaz R, Ruiz-Femenia R, Kerkhof P, and Peters E. Velocity profiles and circulation in Stefan-diffusion. *Chemical Engineering Science*, 63(19):4685–4693, 2008.
- [24] Bearman R and Kirkwood J. Statistical mechanics of transport processes. XI. equations of transport in multicomponent systems. *The Journal of Chemical Physics*, 28(1):136–145, 1958.
- [25] Lightfoot E. N. *Transport phenomena and living systems: Biomedical applications of momentum and mass transfer*. Wiley, New York, USA, 1974.
- [26] Kerkhof P. A modified Maxwell-Stefan model for transport through inert membranes: The binary friction model. *Chemical Engineering Journal and the Biochemical Engineering Journal*, 64(3):319–343, 1996.
- [27] Vural Y, Ma L, Ingham D, and Pourkashanian M. Comparison of the multicomponent mass transfer models for the prediction of the concentration overpotential for solid oxide fuel cell anodes. *Journal of Power Sources*, 195(15):4893–4904, 2010.
- [28] Reid R. C, Prausnitz J. M, and Poling B. E. *The Properties of Gases and Liquids*. McGraw-Hill, 1987.
- [29] Bruggeman D. A. G. Berechnung verschiedener physikalischer konstanten von heterogenen substanzen. I. dielektrizitätskonstanten und leitfähigkeiten der mischkörper aus isotropen substanzen. *Annalen der Physik*, 24:636–679, 1935.
- [30] Lamanna J and Kandlikar S. Determination of effective water vapor diffusion coefficient in PEMFC gas diffusion layers. *International Journal of Hydrogen Energy*, 36(8):5021–5029, 2011.
- [31] De La Rue R. E and Tobias C. W. On the conductivity of dispersions. *Journal of the Electrochemical Society*, 106(9):827–833, 1959.
- [32] Tomadakis M. M and Sotirchos S. V. Effective knudsen diffusivities in structures of randomly overlapping fibers. *AIChE Journal*, 37(1):74–86, 1991.
- [33] Tomadakis M. M and Sotirchos S. V. Ordinary and transition regime diffusion in random fiber structures. *AIChE Journal*, 39(3):397–412, 1993.

- [34] Zamel N, Li X, and Shen J. Correlation for the effective gas diffusion coefficient in carbon paper diffusion media. *Energy Fuels*, 23:6070–6078, 2009.
- [35] Fluckiger R, Freunberger S, Kramer D, Wokaun A, Scherer G, and Buchi F. Anisotropic, effective diffusivity of porous gas diffusion layer materials for PEFC. *Electrochimica Acta*, 54(2):551–559, 2008.
- [36] Baker D, Wieser C, Neyerlin K, and Murphy M. The use of limiting current to determine transport resistance in PEM fuel cells. volume 3, pages 989–999, 2006.
- [37] Kramer D, Freunberger S, Fluckiger R, Schneider I, Wokaun A, Buchi F, and Scherer G. Electrochemical diffusimetry of fuel cell gas diffusion layers. *Journal of Electroanalytical Chemistry*, 612(1):63–77, 2008.
- [38] Stumper J, Haas H, and Granados A. In situ determination of MEA resistance and electrode diffusivity of a fuel cell. *Journal of the Electrochemical Society*, 152(4):A837–A844, 2005.
- [39] Ye X and Wang C.-Y. Measurement of water transport properties through membrane electrode assemblies: Part ii. cathode diffusion media. *Journal of the Electrochemical Society*, 154(7):B683–B686, 2007.
- [40] Friedman S, Zhang L, and Seaton N. Gas and solute diffusion coefficients in pore networks and its description by a simple capillary model. *Transport in Porous Media*, 19(3):281–301, 1995.
- [41] Marrero T and Mason E. Gaseous diffusion coefficients. *Journal of Physical and Chemical Reference Data*, 1(1):3–118, 1972.
- [42] Winkelmann J. Measurement methods: Diffusion of gases in gases, liquids and their mixtures. Landolt Bornstein Database, 2007.
- [43] Rohling J, Shen J, Wang C, Zhou J, and Gu C. Determination of binary diffusion coefficients of gases using photothermal deflection technique. *Applied Physics B: Lasers and Optics*, 87(2):355–362, 2007.
- [44] Astrath N, Shen J, Song D, Rohling J, Astrath F, Zhou J, Navessin T, Liu Z, Gu C, and Zhao X. The effect of relative humidity on binary gas diffusion. *Journal of Physical Chemistry B*, 113(24):8369–8374, 2009.
- [45] Bendt P. Measurements of He³-He⁴ and H₂-D₂ gas diffusion coefficients. *Physical Review*, 110(1):85–89, 1958.

- [46] Remick R and Geankoplis C. Binary diffusion of gases in capillaries in the transition region between Knudsen and molecular diffusion. *Industrial and Engineering Chemistry*, 12(2):214–220, 1973.
- [47] Remick R and Geankoplis C. Ternary diffusion of gases in capillaries in the transition region between Knudsen and molecular diffusion. *Chemical Engineering Science*, 29(6):1447–1455, 1974.
- [48] Evans III R. B, Watson G, and Truitt J. Interdiffusion of gases in a low permeability graphite at uniform pressure. *Journal of Applied Physics*, 33(9):2682–2688, 1962.
- [49] Evans III R. B, Watson G, and Truitt J. Interdiffusion of gases in a low-permeability graphite. II. influence of pressure gradients. *Journal of Applied Physics*, 34(7):2020–2026, 1963.
- [50] Henry Jr. J. P, Cunningham R, and Geankoplis C. Diffusion of gases in porous solids over a thousand-fold pressure range. *Chemical Engineering Science*, 22(1):11–20, 1967.
- [51] Reist P. Steady-state measurement of krypton-85-air diffusion coefficients in porous media. *Environmental Science and Technology*, 1(7):566–569, 1967.
- [52] Whitaker S. Role of the species momentum equation in the analysis of the Stefan diffusion tube. *Industrial and Engineering Chemistry Research*, 30(5):978–983, 1991.
- [53] Van Doormaal M. A and Pharoah J. G. Determination of permeability in fibrous porous media using the lattice Boltzmann method with application to PEM fuel cells. *International Journal for Numerical Methods in Fluids*, 59(1):75–89, 2009.
- [54] Gostick J, Fowler M, Pritzker M, Ioannidis M, and Behra L. In-plane and through-plane gas permeability of carbon fiber electrode backing layers. *Journal of Power Sources*, 162(1):228–238, 2006.
- [55] Gurau V, Bluemle M, Castro E. D, Tsou Y.-M, Jr. T. Z, and Jr. J. M. Characterization of transport properties in gas diffusion layers for proton exchange membrane fuel cells. 2. absolute permeability. *Journal of Power Sources*, 165(2):793–802, 2007.

- [56] Kerkhof P. J and Geboers M. A. Analysis and extension of the theory of multicomponent fluid diffusion. *Chemical Engineering Science*, 60(12):3129–3167, 2005.
- [57] Weber A, Darling R, and Newman J. Modeling two-phase behavior in PEFCs. *Journal of the Electrochemical Society*, 151(10):A1715–A1727, 2004.
- [58] Pant L. M, Secanell M, and Mitra S. K. Design of an experimental setup to study mass transport in micro-nano capillaries and porous media. In *ASME 2010 3rd Joint US-European Fluids Engineering Summer Meeting and 8th International Conference on Nanochannels, Microchannels, and Minichannels*, number FEDSM-ICNMM2010-30305, Montreal, Canada, August 1-5, 2010.
- [59] Pant L. M, Mitra S. K, and Secanell M. Mass transport measurements in porous transport layers of a PEM fuel cell. In *ASME 2011 9th International Conference on Nanochannels, Microchannels, and Minichannels*, number ICNMM2011-58181, Edmonton, Alberta, Canada, June 19-22, 2011.
- [60] Eiceman G. A. *Encyclopedia of Analytical Chemistry*, volume 12, chapter : Gas Chromatography : Introduction, pages 10629–10632. Wiley, 2000.
- [61] James A and Martin A. Gas-liquid partition chromatography. a technique for the analysis of volatile materials. *The Analyst*, 77(921):915–931, 1952.
- [62] *User Manual, Micro-GC Portable Model CP-2003P*. Varian Inc., California, USA, 2000.
- [63] Heinzelmann F. J, Wasan D. T, and Wilke C. Concentration profiles in Stefan diffusion tube. *Industrial and Engineering Chemistry Fundamentals*, 4(1):55–61, 1965. doi: 10.1021/i160013a009.
- [64] Benkhalifa M, Arnaud G, and Fohr J.-P. The viscous air flow pattern in the Stefan diffusion tube - application to the mutual diffusion in a porous media. *Transport in Porous Media*, 19(1):15–36, 1995. 996) 1.
- [65] Champine L, Reichelt M. W, and Kierzenka J. Solving boundary value problems for ordinary differential equations in MATLAB with `bvp4c`, 2003. URL <http://www.mathworks.com/matlabcentral/fileexchange/3819>. Taken on June 06, 2011, 1.30 PM.

- [66] Williams M, Begg E, Bonville L, Kunz H, and Fenton J. Characterization of gas diffusion layers for PEMFC. *Journal of the Electrochemical Society*, 151(8): A1173–A1180, 2004.
- [67] Martinez M, Shimpalee S, Zee J. V, and Sakars A. Assessing methods and data for pore-size distribution of PEMFC gas-diffusion media. *Journal of the Electrochemical Society*, 156(5):B558–B564, 2009.
- [68] Gray W. G and O’Neill K. On the general equations for flow in porous media and their reduction to Darcy’s law. *Water Resources Research*, 12(2):148–154, 1976.
- [69] Teng H and Zhao T. An extension of Darcy’s law to non-stokes flow in porous media. *Chemical Engineering Science*, 55(14):2727–2735, 2000.
- [70] Hirschfelder J, Curtiss C, and Bird R. *Molecular Theory of Gases and Liquids*. Wiley, 1954.
- [71] Thiele S, Zengerle R, and Ziegler C. Nano-morphology of a polymer electrolyte fuel cell catalyst layer-imaging, reconstruction and analysis. *Nano Research*, pages 1–12, 2011.
- [72] Agarwal R, Yun K.-Y, and Balakrishnan R. Beyond Navier-Stokes: Burnett equations for flows in the continuum-transition regime. *Physics of Fluids*, 13(10):3061–3085, 2001.
- [73] Petersen H. *The Properties of Helium: Density, Specific Heats, Viscosity, and Thermal Conductivity at Pressures from 1 to 100 bar and from Room Temperature to about 1800 K*. Danish Atomic Energy Commision, September 1970. Riso report no: 224.
- [74] Tseronis K, Kookos I, and Theodoropoulos C. Modelling mass transport in solid oxide fuel cell anodes: a case for a multidimensional dusty gas-based model. *Chemical Engineering Science*, 63(23):5626–5638, 2008.